

On the Small-Scale Variability of Electrical Soil Properties and its Influence on Geophysical Measurements

DISSERTATION

zur Erlangung des Doktorgrades
der Naturwissenschaften

vorgelegt beim Fachbereich Geowissenschaften
der Johann Wolfgang Goethe – Universität
in Frankfurt am Main

von
Jan Igel
aus Wangen im Allgäu

Frankfurt (2007)
(D 30)

vom Fachbereich Geowissenschaften der Johann Wolfgang Goethe –
Universität als Dissertation angenommen.

Dekan: Prof. Dr. G. Brey

Gutachter: Prof. Dr. A. Junge, Frankfurt
Prof. Dr. H. Wilhelm, Karlsruhe

Datum der Disputation: 12.07.2007

Abstract

Physical soil properties feature high spatial variabilities which are known to affect geophysical measurements. However, these variations are not considered in most cases. The challenging questions are firstly to what extent soil heterogeneities influence geophysical data and secondly what the uncertainties in the deduced results are. This topic is analysed for DC resistivity and GPR measurements which are frequently used for near-surface explorations e.g. for hydrological problems. To determine the pattern of electric soil properties in situ with the required high spatial resolution, geophysical measuring techniques are methodically enhanced.

High-resolution dipole-dipole resistivity measurements with electrode separations of 0.1 m are suitable to determine electric conductivity distribution of the topsoil. Due to the small electrode separations, the actual electrode geometry has to be considered. An analytic expression is derived for the geometric factor of arrays with elongated electrodes and is experimentally verified. Assuming point electrodes instead can result in deviations of apparent conductivity of up to 50%.

Two methods are used to determine soil permittivity with GPR: Firstly, the coefficient of reflection at the interface air–soil is measured with a 1 GHz air-launched horn antenna and soil permittivity is deduced with an accuracy of 10% and a spatial resolution of 0.25 m \times 0.3 m. Secondly, the velocity of the groundwave is measured with a new setup using two receiving antennas enhancing the lateral resolution from typically 0.5 m and even more for standard techniques to approximately 0.1 m with the new technique. With the latter, permittivity is mapped with an accuracy of 3–8%.

The optimised measuring techniques are used to determine the electric properties of sandy soils in the field. The field data are statistically analysed and a density function model as well as a variogram model are adapted to the spatial conductivity and permittivity distribution. Conductivity possesses high spatial variability and a correlation length of approximately 0.4 m. Both GPR techniques yield high variability of permittivity with correlation lengths between 0.25 m and 1.8 m. Geostatistical simulations are used to generate random

media featuring the same statistical properties as in the field. These media are used to generate realistic synthetic data by means of FD calculations.

Both, 2D and 3D dipole-dipole measurements can be used to determine statistical parameters of conductivity distribution in the field. The variance is somewhat underestimated by the DC measurement but the spatial correlation is well reproduced in a wide range of correlation lengths as proved by simulations. Soil heterogeneities which cannot be resolved with Schlumberger setups itself can nevertheless cause variations of the sounding curves. Conductivity variations as deduced in the field generate significant variations of simulated sounding curves. The uncertainties in the inverted models are comparable to 6% data noise when deducing equivalent models.

Even in pedologically homogeneous sandy soil, moisture pattern and the resulting permittivity variations cause strong GPR diffractions as demonstrated by FD simulations. This influences the detectability of objects, e.g. landmine detection with GPR. If the soil is relatively dry and the permittivity contrast between soil and mine is small, landmine detection will be difficult due to soil diffractions masking the mine signal. Furthermore, typical soil heterogeneities cause undulating groundwaves, thus complicating the velocity destination with moveout measurements, which are commonly used for classical groundwave analysis. Conductivity variations as typical for soils showed to have a minor effect on GPR measurements than variations of permittivity.

In summary, geostatistical analysis and simulation provide a powerful tool to simulate geophysical measurements under field conditions including soil heterogeneity which can be used to quantify the uncertainty of field measurements by geologic noise. Such realistic simulations are helpful to e.g. optimise the survey design prior to a field campaign or to appraise field data and their interpretation.

Zusammenfassung

Der Boden bildet die oberste Schicht der Erde und stellt die Verbindung zwischen Lithosphäre und Atmosphäre dar. Ein wesentliches Merkmal von Böden ist die hohe räumliche und zeitliche Variabilität ihrer physikalischen Eigenschaften. Geophysikalische Messungen werden bekanntlich stark von der räumlichen Heterogenität der physikalischen Bodenparameter beeinflusst, da sich die Sensoren in der Regel direkt im oder auf dem Boden befinden. Gleichwohl werden diese Effekte bei Messungen vielfach nicht berücksichtigt. Es drängt sich die Frage auf, in welchem Ausmaß geophysikalische Messungen von Heterogenitäten des Bodens bestimmt werden und ob die resultierenden Messungenauigkeiten sowie Unsicherheiten der abgeleiteten Ergebnisse quantifizierbar sind. Dieser Frage wird speziell für den Fall von Geoelektrik- und Georadar-Messungen nachgegangen, die häufig für oberflächennahe Untersuchungen verwendet werden, z.B. um hydrologische Fragestellungen zu bearbeiten.

Die elektrische Leitfähigkeit des Bodens beeinflusst geoelektrische Messungen stark, da sich die Elektroden direkt im Boden befinden und in ihrer unmittelbaren Umgebung die Sensitivität der gemessenen scheinbaren Leitfähigkeit bezüglich der Bodenleitfähigkeit am größten ist. Das Georadar hingegen wird sowohl durch die elektrische Leitfähigkeit als auch den Dielektrizitätskoeffizienten (DK) beeinflusst. Die Variabilität dieser Bodeneigenschaften beeinträchtigen das Georadar stark, da die Antenne direkt auf dem Untergrund liegt und die elektromagnetischen Wellen an Bodenheterogenitäten gestreut werden. Dies gilt insbesondere dann, wenn die Heterogenitäten in der Größenordnung der Wellenlänge liegen. Um die für beide Messverfahren relevanten elektrischen Bodenparameter mit der benötigten hohen räumlichen Auflösung im Gelände bestimmen zu können, werden vorhandene geophysikalische Verfahren methodisch verbessert.

Die räumliche Anordnung der Messpunkte auf einer Fläche beeinflusst die abgeleiteten statistischen Parameter. Es werden verschiedene Messaufstellungen mit jeweils gleicher Anzahl von Messpunkten auf synthetischen Flächen mit zufallsgenerierten Parameterverteilungen unterschiedlicher Korrelationslängen

angewendet. Ein Vergleich zeigt, dass Messaufstellungen mit längeren sich kreuzenden Profilen oder eine reine Zufallsverteilung der Messpunkte besser geeignet sind als Aufstellungen, bei denen die Messpunkte auf wenige, dafür jedoch dichter beprobte Bereiche, konzentriert sind. Eng abgetastete, sich kreuzende Profile zeigen die besten Ergebnisse bei der Bestimmung der Häufigkeitsverteilung und des Variogramms. Diese Aufstellung ist auch gegenüber der Lokation auf der zu untersuchenden Fläche unempfindlich, d.h. das Ergebnis hängt nur geringfügig von der Position der Messkonfiguration auf der zu untersuchenden Fläche ab.

Die elektrische Leitfähigkeit des Bodens hängt von einer Vielzahl von Parametern ab, wie Textur, Salinität und Wassergehalt. Hochauflösende Dipol-Dipol Geoelektrik-Messungen mit Elektrodenabständen von 0,1 m eignen sich gut, um die Verteilung der elektrischen Leitfähigkeit im Oberboden zu bestimmen. Wegen des geringen Elektrodenabstandes muss jedoch die tatsächliche Elektrodengeometrie berücksichtigt werden. Die übliche Annahme von punktförmigen Elektroden kann bei hochauflösenden Messungen zu Fehlern in den scheinbaren Leitfähigkeiten von bis zu 50% führen. Es wird eine analytische Formel für Geometriefaktoren von Elektrik-Aufstellungen mit länglichen Elektroden abgeleitet. Diese Faktoren werden experimentell durch Messungen in einem homogenen Halbraum, einem großen Wassertank, verifiziert. Durch Verwendung der korrekten Geometriefaktoren ergeben sich scheinbare elektrische Leitfähigkeiten, die sehr gut mit der tatsächlichen Leitfähigkeit des Wassers übereinstimmen.

Der DK des Bodens hängt stark vom Wassergehalt ab. Die sich ergebenden Zusammenhänge werden erläutert und einige wichtige Modelle vorgestellt, welche die Abhängigkeit des DK vom Wassergehalt beschreiben. Es werden die Grundprinzipien der elektromagnetischen Wellenausbreitung, ausgehend von den vier Maxwellgleichungen beschrieben und wichtige Gesetzmäßigkeiten abgeleitet. Im Gegensatz zu den ansonsten üblichen Näherungen werden alle drei elektromagnetischen Parameter berücksichtigt. Das erlaubt eine Abschätzung der zu erwartenden Fehler, wenn bei Feldmessungen vereinfachte Formeln verwendet werden, z.B. wenn, wie üblich, die magnetische Permeabilität des Bodens $\mu_r^{Boden} = 1$ gesetzt wird.

Mit dem Georadar werden zwei unterschiedliche Verfahren verwendet, um den DK des Oberbodens zu bestimmen: Bei dem ersten Verfahren wird der Reflexionskoeffizient an der Grenzfläche Luft–Boden mit einer 1 GHz Hornantenne gemessen und daraus der DK des Bodens mit einer Genauigkeit von 10% und einer räumlichen Auflösung von 0,25 m \times 0,3 m abgeleitet. Die Er-

fassungstiefe dieser Anordnung beträgt dabei nur wenige Zentimeter. Bei dem zweiten Verfahren wird die Ausbreitungsgeschwindigkeit der Bodenwelle bestimmt. Daraus wird der DK in dem annähernd obersten Dezimeter des Bodens bestimmt. Im Gegensatz zur klassischen Methode, die eine Sende- und eine Empfangsantenne verwendet und eine laterale Auflösung von üblicherweise 0,5 m und größer hat, wurde eine neue Methode entwickelt, die zwei Empfangsantennen verwendet. Es müssen nun nur Laufzeitdifferenzen zwischen den beiden Empfängern bestimmt werden, was zum einen die Messung und Auswertung vereinfacht und zum anderen eine erheblich bessere Auflösung von etwa 0,1 m ermöglicht. Die Messgenauigkeit liegt dabei je nach DK des Untergrunds bei etwa 3–8%.

Die optimierten Messverfahren werden verwendet, um die elektrischen Eigenschaften von Sandböden, die als Grünland genutzt werden, im Feld zu bestimmen. Die Felddaten werden statistisch analysiert und es wird eine Modellfunktion an die Verteilungsdichte und das Variogramm der räumlichen Verteilung der Leitfähigkeit und des DK angepasst. Die elektrische Leitfähigkeit zeigt dabei eine hohe räumliche Variabilität mit Korrelationslängen von nur ca. 0,4 m. Die beiden Georadar-Verfahren liefern ähnliche Ergebnisse und eine hohe Variabilität des Dielektrizitätskoeffizienten mit Korrelationslängen zwischen 0,25 und 1,8 m. An einer Lokation zeigt die Verteilung eine Anisotropie, die vermutlich durch die ehemalige landwirtschaftliche Nutzung hervorgerufen wird. Bis vor zwei Jahren wurde die Fläche als Acker genutzt und dann in eine Grünfläche umgewandelt. Der DK zeigt senkrecht zur ehemaligen Pflugrichtung eine Korrelationslänge von 0,25 m und parallel zur Pflugrichtung eine etwa 5 mal größere Korrelationslänge.

Die an die Felddaten angepassten statistischen Modelle dienen dazu, mit Hilfe geostatistischer Simulationsverfahren zufallsverteilte Medien zu generieren, welche die gleiche Leitfähigkeits- und DK-Verteilung wie im Feld aufweisen. Diese Medien werden im Weiteren verwendet, um mit Hilfe von FD-Simulationen realistische synthetische Daten zu erzeugen.

Mittels Simulationen wird gezeigt, dass sowohl 2D- als auch 3D-Dipol-Dipol Messungen verwendet werden können, um statistische Parameter der Leitfähigkeitsverteilung im Gelände zu bestimmen. Bei der Inversion der 3D-Messungen können bessere Datenanpassungen erzielt werden als bei den 2D-Messungen. Die Varianz der Leitfähigkeitsverteilung im Untergrund wird durch geoelektrische Messungen etwas unterschätzt. Je kleiner die Korrelationslänge der Leitfähigkeitsverteilung, desto stärker die Abweichungen in der Verteilungsdichte. Dieser Effekt ist für 2D-Inversionen etwas stärker als bei

3D-Inversionen. Der Mittelwert und die Form der statistischen Verteilung wird hingegen korrekt wiedergegeben. Ebenso wird die räumliche Korrelation für Korrelationslängen größer 0,2 m durch 2D- und 3D-Messungen korrekt erfasst. 3D-Messungen sind jedoch um ein vielfaches zeitaufwändiger als 2D-Messungen, und für eine statistische Parameterbestimmung ist auch eine große Datenbasis von hoher Wichtigkeit.

Bei Schlumberger-Messungen können Bodenheterogenitäten, die mit der Aufstellung nicht auflösbar sind, Variationen der Sondierungskurven verursachen. Leitfähigkeitsvariationen, wie sie in situ bestimmt wurden, rufen beträchtliche Variationen in modellierten Sondierungskurven hervor. Bei einem heterogenen Oberboden (0–0,3 m) ist die Unsicherheit in den invertierten Modellen vergleichbar mit einem Datenfehler von 6% bei der Bestimmung von Äquivalenzmodellen. Bei einem homogenen Oberboden und heterogenem Unterboden (0,3–1 m) entsprechen die Unsicherheiten einem Datenfehler von nur 2%, was ein Effekt der abnehmenden Sensitivität der geoelektrischen Aufstellung mit zunehmender Tiefe ist. Es ist also häufig die Bodenheterogenität und nicht die Messungenauigkeit der Apparatur von üblicherweise etwa 1%, welche die Genauigkeit von geoelektrischen Tiefensondierungen beschränkt.

FD-Simulationen zeigen, dass die neue Bodenwellen-Messtechnik mit zwei Empfängern die statistischen Eigenschaften einer heterogenen DK-Verteilung mit einer Korrelationslänge von 0,3 m korrekt abbildet.

Die Bodenfeuchteverteilung und die daraus resultierende DK-Verteilung kann selbst in einem nach bodenkundlichen Maßstäben homogenen Sandboden starke Diffraktionen im Radargramm hervorrufen, wie anhand von Simulationsrechnungen belegt wird. Unter vielen Anwendungsbeispielen beeinflusst dies beispielsweise auch die Landminensuche mit dem Georadar. Es werden hochfrequente Constant-Offset-Messungen simuliert, wie sie üblicherweise bei der Minensuche Anwendung finden. Bei relativ trockenem Boden und folglich geringem DK-Kontrast zwischen Mine und Boden ist die Detektion von Minen schwierig, da ihr Signal von Bodendiffraktionen überlagert wird. Bei feuchten Böden können Minen besser detektiert werden, selbst wenn die Feuchteverteilung heterogen ausgeprägt ist. Hingegen haben Leitfähigkeitsvariationen, wie sie typisch für sandige Böden sind, keinen Einfluss auf die Minensuche mit dem Georadar. Erst Leitfähigkeiten größer als 0,05 S/m führen zu nennenswerten Beeinträchtigungen.

Des Weiteren verursachen typische Bodenheterogenitäten eine Krümmung der Bodenwelle, die eine Geschwindigkeitsbestimmung aus Moveout-Messungen,

wie sie für gewöhnlich bei der klassischen Bodenwellenauswertung verwendet werden, erschweren. Es zeigt sich, dass Leitfähigkeitskontraste, wie sie typisch für Oberböden sind, einen geringeren Einfluss auf Georadar-Messungen haben als Variationen des DK.

Wie schon erwähnt, zeigen die elektrischen Bodeneigenschaften einen engen Zusammenhang mit dem Wassergehalt. Deshalb sind Geoelektrik- und insbesondere Georadar-Messungen geeignet, die Wasserverteilung auf verschiedenen Skalen zu bestimmen. Der Wassergehalt ist für viele Umweltwissenschaften ein wichtiger Parameter, z.B., um in der Landwirtschaft Bewässerungen zu steuern, im Bauwesen zur Optimierung der Verdichtung oder zur Abschätzung von Hangstabilitäten und in der Hydrologie zur Bestimmung der Evapotranspiration. Die Heterogenität der Feuchteverteilung beeinflusst z.B. die Infiltration und damit den Schadstoffeintrag.

Die Feldmessungen zeigen, dass die elektrische Leitfähigkeit und der DK und folglich auch der Wassergehalt des Oberbodens eine hohe Variabilität aufweisen. Solche Heterogenitäten spielen bei der Beschreibung und Berechnung von nicht-linearen Prozessen eine große Rolle. So hängen z.B. die Evapotranspiration, die Wärme- und hydraulische Leitfähigkeit nicht-linear vom Wassergehalt ab. Dies alles sind Größen, die z.B. in Wasserhaushalts- sowie Wetter- und Klimamodellierungen eingehen und über deren kleinräumige Variabilität und deren Änderung mit der Zeit wenig bekannt ist.

Bis heute gehören geostatistische Verfahren nicht zur Standardtechnik, wenn Modelle für Computersimulationen erstellt werden. Sie erweisen sich als leistungsfähiges Hilfsmittel, um die in der Natur vorkommenden Zufallsprozesse und -zustände zu implementieren. Geostatistische Simulationstechniken sind sehr gut geeignet, um geophysikalische Messungen unter realen Feldbedingungen, d.h. unter Berücksichtigung der Bodenheterogenitäten, zu simulieren. Es können damit realistische Fehler abgeschätzt werden, mit denen Feldmessungen durch den „geologischen Noise“ behaftet sind. Die Kenntnis solcher Fehler ist z.B. wichtig für die Inversion von Daten. Realistische Simulationen dienen aber auch der Optimierung von Messaufstellungen bei der Planung einer Messkampagne oder der Bewertung von Interpretationsergebnissen. Die beschriebene Vorgehensweise kann die Geophysik einen entscheidenden Schritt weiterbringen, zum Verständnis der Wechselwirkung zwischen Lithosphäre und Atmosphäre beizutragen.

Contents

Abstract	I
Zusammenfassung	III
Contents	XI
1 Introduction	1
1.1 Aims and Objectives	1
1.2 Guideline of the Thesis	4
2 Geostatistical Methods	7
2.1 Introduction	7
2.2 Basic Assumptions	8
2.3 Frequency Distribution of Data – Normal Score Transform	9
2.4 Spatial Correlation of Data	10
2.5 Geostatistical Simulation	14
2.6 Determining an Optimal Sampling Configuration	15
2.6.1 Generation of a Synthetic Spatial Variable Distribution	17
2.6.2 Sampling Configurations	19
2.6.3 Reproducibility of the Distribution Function	19
2.6.4 Reproducibility of the Spatial Correlation	23
2.6.5 Repeatability	26
2.6.6 Summary: The Optimal Sampling Layout	29
3 Electric Conductivity σ	31
3.1 Electric Conductivity of Soils	31
3.2 Theory of Electric Current Flow	32
3.2.1 Influence of Electrode Geometry	35
3.3 Determining the Electric Conductivity of Soils	39
3.3.1 Experimental Setup	39
3.3.2 Spatial Field Measurements and Geostatistical analysis	39
4 Dielectric Permittivity ε	47
4.1 Dielectric Properties of Soils	47

4.1.1	Mechanisms of Polarisation	47
4.1.2	Dielectric Properties of Water	48
4.1.3	Dielectric Properties of Soil Matrix	51
4.1.4	Mixing Models	51
4.1.5	Determining the Dielectric Permittivity of Porous Media	53
4.2	Theory of Electromagnetic Wave Propagation	55
4.2.1	Fundamental Equations of Electrodynamics	55
4.2.2	Dispersion Relation	57
4.2.3	Reflection of Electromagnetic Waves	60
4.2.4	Horizontal Resolution – 1st Fresnel Zone	64
4.2.5	Homogeneous and Inhomogeneous Waves – the Groundwave of GPR	66
4.3	Determining Permittivity by the Coefficient of Reflection	69
4.3.1	Coefficient of Reflection at the Interface Air – Soil	69
4.3.2	Experimental Setup	73
4.3.3	Spatial Field Measurements and Statistical Analysis	79
4.4	Determining Permittivity by Using the Groundwave	84
4.4.1	Velocity of Radar Waves in Soil	84
4.4.2	Groundwave Measurements – State of the Art	86
4.4.3	Experimental Setup Using 2 Receivers	89
4.4.4	Spatial Field Measurements and Statistical Analysis	98
5	Influence of Soil Variability on Geophysical measurements	105
5.1	Influence of Conductivity Variations on DC Measurements	106
5.1.1	Accuracy of Dipole-Dipole Measurements to Determine Statistical Properties	106
5.1.2	Influence on Resistivity Soundings	111
5.2	Influence of Conductivity and Permittivity Variations on GPR Measurements	117
5.2.1	Accuracy of Groundwave Measurements to Determine Statistical Properties	117
5.2.2	Influence on Constant Offset Measurements; Landmine Detection	120
5.2.3	Influence on Moveout Measurements	124
6	Summary and Conclusions	129
A	Results of Different Sampling Layouts on Simulated Data	135
B	Pedological Description of the Measuring Locations	141

B.1 Location 1	141
B.2 Location 2	143
B.3 Location 3	145
Used Symbols	147
List of Figures	153
List of Tables	155
Used Software	157
Bibliography	168
Acknowledgements	169
Curriculum Vitae	171
Declaration	173

1 Introduction

1.1 Aims and Objectives

Soil as the top layer of the earth is situated at the interface between the lithosphere and the atmosphere and therefore plays an important role for hydrological and biological processes. Soil properties show high variability in space and time. When carrying out geophysical measurements, the physical sensors are in most cases placed on or inside the soil and thus soil heterogeneity has a great influence on geophysical measurements. The aim of the thesis is to determine the effect of small-scale variabilities of electrical soil properties on geophysical measurements.

Soil **conductivity** influences geoelectric measurements as the electrodes are placed in the soil and the measured apparent conductivity is highly sensitive to the conductivity in vicinity of the electrodes. Especially the small-scale variability in the range of decimetres and a few metres have a negative influence on the measurements (Wtorek et al., 2003). They have the typical dimension of electrode separation and cannot be resolved by classical geoelectric measurement layouts. For instance, when carrying out Schlumberger resistivity soundings, small-scale soil heterogeneities cannot be resolved but cause significant variations of the sounding curves. This is a source of error which is generally known but not adequately studied up to now wherefore there is a lack of literature on this topic.

Ground-penetrating radar (GPR) is influenced by electric conductivity and **permittivity**. Electric soil properties highly affect GPR waves as soil is the medium in the direct vicinity of the antennas (Holliger et al., 2004; Lampe and Holliger, 2003). Electromagnetic waves are reflected and scattered at soil heterogeneities. This is particularly the case if heterogeneities occur in the scale of the wavelength of the radar signals which are typically between 1 decimetre and a few metres depending on the used antenna frequencies. If small objects have to be detected with GPR, e.g. non-metallic landmines (Bruschini et al., 1998; Dam et al., 2003; Hendrickx et al., 2001; Miller et al., 2002) which are

usually buried in the first 20 centimetres, topsoil heterogeneity causes geologic noise in the data which can mask the mine signal. Soil variability also has a negative influence on the detection of deeper objects which is a common application for GPR (Becht et al., 2006; Fisher et al., 1992; Davis and Annan, 1989). For instance, an irregular permittivity distribution as typical for the vadose zone causes a plane groundwater table to occur as an uneven reflector.

So far, concerning standard applications for geophysical measurements, soil comprising its heterogeneity has been looked at as a disturbing layer between the sensor and the target producing a lot of **geologic noise** to the data which is difficult to quantify and to take into consideration. However, in the last years the vadose zone in general and particularly soil have become an object of research studied with geophysical methods due to its importance for environmental issues. Investigating small-scale structures in the soil is a challenge for geophysical techniques as they are usually applied on larger scales. Therefore, methodological enhancements have to be made to adapt the methods to the specific purposes, e.g. a high spatial resolution in the range of decimetres (Müller et al., 2003).

The aim of the thesis is first to develop and adapt geoelectric and GPR measuring techniques which are suited to determine the small-scale variability of electric conductivity and permittivity. These techniques will be applied in the field to determine the spatial pattern of the electric soil properties. In a second step the influence of the determined variability on geoelectric and GPR measurements is analysed by means of finite difference (FD) calculations. Different scenarios are simulated under realistic conditions. The final result is an **assessment of uncertainty** which may be expected when carrying out geoelectric and GPR measurements on actual locations.

The electric soil properties are linked to **soil water content**. Therefore, geoelectrical measurements and particularly GPR are useful tools to determine soil water distribution on different scales (Turesson, 2006; Daily et al., 1992; Greaves et al., 1996; Huisman et al., 2003a; Hubbard et al., 2002; Hanafy and el Hagrey, 2006; Schmalholz et al., 2004; Garambois et al., 2002). Soil water content is an important parameter in several domains, e.g. in agriculture to control irrigation, in geotechnics to optimise soil consolidation and to assess the potential of landslides or in hydrology to determine evapotranspiration. Local variabilities dominate water flow even in homogeneous sand (Schmalz et al., 2002). Soil moisture heterogeneity influences infiltration velocity and characterises preferential flow paths (Täumer et al., 2006) and therefore is an important parameter to assess vulnerability of groundwater to pollution. It is



Figure 1.1: Picture of sandy soil demonstrating soil heterogeneity on an area of $1\text{ m} \times 1\text{ m}$. The turf has been removed and the pattern corresponds to the soil moisture (dark parts = moist soil, light parts = dry soil), pers. comm. Schmalholz, TU Berlin (<http://www.interurban.de>).

also an important parameter for meteorological processes. It determines the evapotranspiration, effective heat capacity and thermal conductivity.

The water content of topsoil features high **spatial variability**. Fig. 1.1 shows a picture of a sandy soil featuring a heterogeneous moisture distribution. Spatial variability in soil water content is caused by heterogeneity of physical soil properties as texture, water repellency, micro-topography, soil cultivation and vegetation (Ritsema and Dekker, 1994; Wendroth et al., 1999; Dekker et al., 1999). Consequently, as they are linked to the water content, electric soil properties feature comparable variability. Determining these properties by geophysical measurements provides information about the spatial pattern of soil water content.

There is a strong demand on determining small-scale variability of soil moisture (Lehmann, 1995). Soil moisture has a great influence on hydrological model calculations and its variability is the greatest uncertainty (Montenegro Ferrigno, 1995; Herbst et al., 2006). The effects of small-scale heterogeneity in land surface characteristics on the large-scale fluxes of water and energy has become a central focus of many climatology research projects (Wood, 1997;

Vanderborght et al., 2006). When calculating evapotranspiration there is a significant difference whether the soil moisture is assumed to be heterogeneous or spatially averaged, e.g. those determined by remote sensing techniques (Ulaby et al., 1996). This is an effect of **non-linear relation** between moisture and evapotranspiration (Feddes et al., 1999). The same holds true for e.g. thermal or hydrological conductivity of the soil and leads to the problem of scaling.

Usually, it is not possible to measure the parameters directly at the scale we need for describing processes, e.g. the permeability for describing fluid flow or the electromagnetic parameters for describing electromagnetic wave propagation (Moysey and Knight, 2004). When the parameters are determined in the laboratory scale or in situ in the scale of a few metres, one will have to shift them to a larger scale. This **up-scaling** is not trivial and linear averaging usually will fail as non-linear effects are often involved. For example, concerning fluid transport, the hydraulic permeability is not additive (Chilès and Delfinier, 1999). The process of up-scaling is to find a fictive homogeneous medium which behaves like the analysed heterogeneous medium. Thus, the heterogeneity has to be known when carrying out up-scaling.

1.2 Guideline of the Thesis

In the following, a brief preview of the general approach is given. A flowchart representing the guideline of the thesis is depicted in Fig. 1.2.

In **chapter 2**, the fundamentals of geostatistical data analysis and simulation are described. The basic parameters to characterise a regionalised variable are the density function which specifies the frequency a data value can take and the variogram which describes the spatial correlation of data. Both are needed as input parameters for geostatistical simulation techniques which are used to generate random distributed media. When determining the statistical properties in situ, one of the main issues is to use an optimal sampling or measuring layout. The aim is to approximate the density function and the variogram by the experimental data as close as possible with as few measurements as possible. It has to be analysed to which extent the determined statistical parameters depend on the allocation of the measuring points. An optimal sampling configuration has to be found featuring only minor deviations on different sites which possess a wide range of correlation lengths. A further important aspect is the sensitivity of the deduced statistics in respect to a displacement

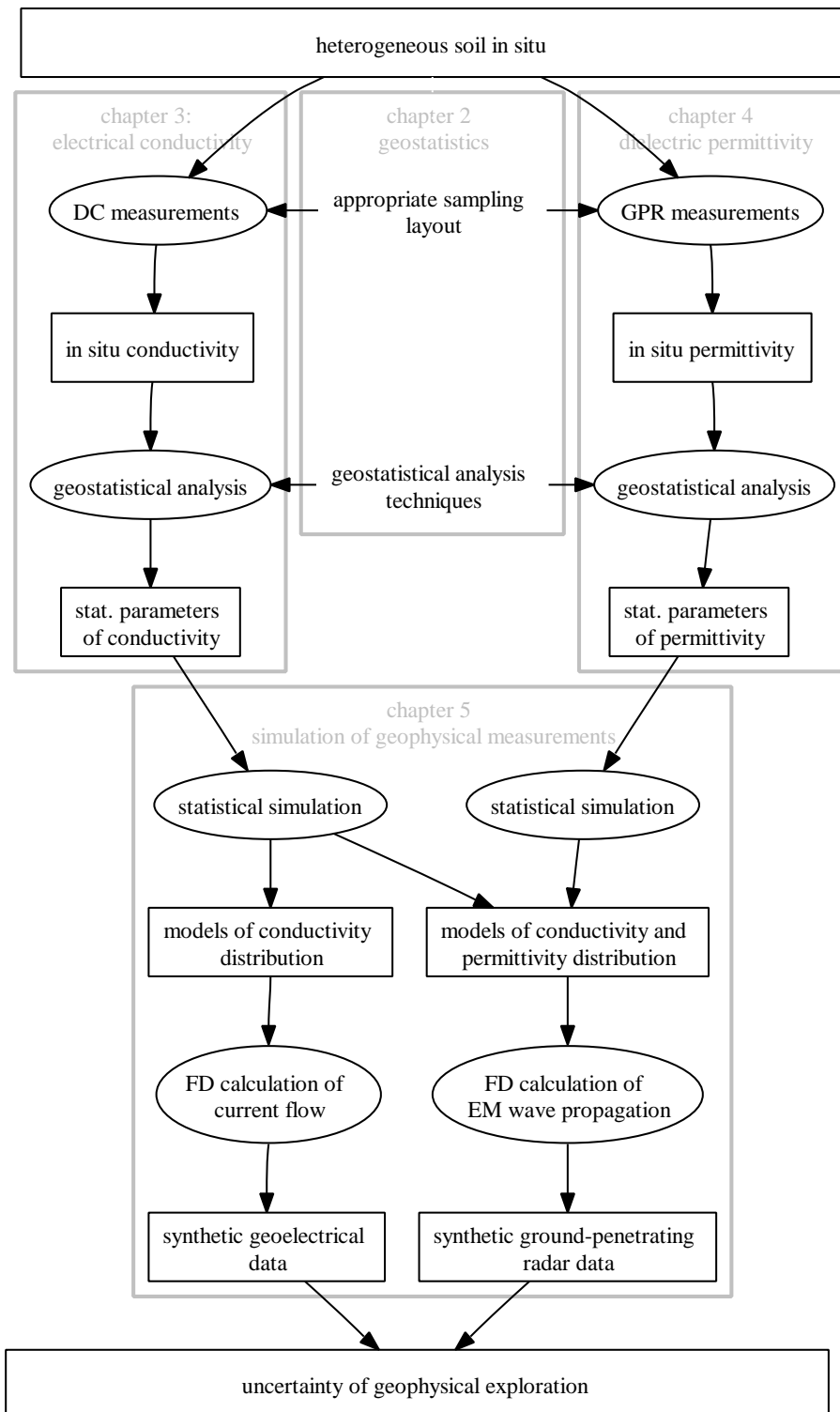


Figure 1.2: Flowchart representing the guideline of the thesis: elliptical nodes are the processes and box-shaped nodes are the results.

of the layout inside the area which is explored.

In **chapter 3**, the electric conductivity of soils is analysed with DC geoelectrical measurements. A brief overview is given of the principle physical processes which effect the conductivity of soils. The setup used for the field measurements has to be adopted to the required high spatial resolution. It has to be analysed whether setups, electrodes and interpretation techniques used for standard DC applications are suited for small-scale measurements. The methodically enhanced measurement techniques are applied in field and typical statistical parameters of topsoil conductivity distribution will be derived.

In **chapter 4**, the permittivity distribution in the topsoil is determined with ground-penetrating radar (GPR). The principal physical processes determining the permittivity of soils are specified and the theoretical fundamentals of electromagnetic wave propagation are deduced. Different methods are adopted and enhanced to determine soil permittivity with GPR. These methods have to be critically evaluated concerning their absolute accuracy and the spatial resolution they provide. Field measurements are carried out using the developed GPR measuring techniques and typical statistical parameters of topsoil permittivity distribution are derived.

In **chapter 5**, the influence of heterogeneities of the upper soil on resistivity and GPR measurements is determined by FD calculations. Heterogeneous FD models are generated representing fluctuations which are typical for natural soils and which were determined in chapters 3 and 4. First, it is tested whether the developed high-resolution geophysical methods do accurately determine the statistical parameters of heterogeneous conductivity and permittivity distribution. Furthermore, it is analysed how small-scale soil variabilities affect common resistivity and GPR measurements. The objective is a realistic estimation of uncertainty in the results of the geophysical measurements caused by geologic noise.

2 Geostatistical Methods

2.1 Introduction

Geostatistical analysis represents the same for regionalised variables as time series analysis does for temporally sampled data. Where time-series analysis describes the change of a physical quantity with time, geostatistical analysis quantitatively describes how regionalised variables change with space. Geostatistical methods have first been applied in the field of resource management, e.g. to assess the reservoir of ore in mines (Krige, 1951). The mathematical fundamentals have been formulated mainly by Matheron (1965, 1971). In the last years, geostatistics has been applied to further domains in geosciences especially to agricultural and hydrology problems (Schafmeister-Spierling, 1990; Lehmann, 1995; Western et al., 1998; Western and Blöschl, 1999; Miao et al., 2000; Täumer et al., 2006) or to some domains of geophysics, most notably to hydro-geophysics (Rea and Knight, 1998; Huisman et al., 2002, 2003a; Lampe and Holliger, 2003; Knight et al., 2004; Tronicke and Holliger, 2005). But in contrast to time series analysis, geostatistical analysis has not become a standard tool for geophysical data interpretation up to now.

The most commonly used application of geostatistics is kriging, albeit, it is often applied to data in an automatic manner without regarding the mathematical background. Kriging provides the best among all linear interpolation methods, i.e. the most likely value of a variable at a location inside a sampled area. As a fundamental advantage compared to other interpolation methods, kriging can provide an estimation error. Kriging will always generate a smooth distribution of the variable and will suppress small-scale variations. Therefore, it is not the adequate method if small-scale heterogeneities are of interest and will influence the processes which are regarded. Neglecting the small-scale variability and using smoothed interpolations instead can cause significant biases when nonlinear effects are involved (Chilès and Delfinier, 1999), e.g. using a mean soil moisture instead of a small-scale variable when computing water movement in the unsaturated zone with the Richards equation (Montenegro Ferrigno, 1995). For these purposes, geostatistical simulation

techniques should be used as small-scale variations will be reproduced. As several realisations can be calculated, geostatistical simulations can also provide a measure of uncertainty of the results, e.g. when carrying out flow simulations (Schafmeister-Spierling, 1990; Deutsch and Journel, 1998).

The geostatistical analysis used in the later chapters will be carried out in 3 steps:

- statistical and spatial analysis of the data
- fitting of a statistical model
- statistical simulation.

2.2 Basic Assumptions

In the following, some assumptions have to be made concerning the distribution of the regarded variable in space. Deducing statistical parameters of a variable as the mean, the variance or the density function requires repetitive sampling. As opposed to a physical experiment which can be repeated several times, in geosciences, usually only one sample or one datum is available at a specific location. The way out is to regard the value at another location as a replication of the random variable at the position under consideration. This presumes that the random variable $Z(\vec{x})$ at every location \vec{x} originates from the same random process and corresponds to the hypothesis of strong stationarity. For most practical situations, second-order stationarity or presuming the intrinsic hypothesis will suffice.

- **Stationarity:** The random function is invariant under an arbitrary translation, i.e. the distribution is homogeneous in space.
- **Second-order stationarity:** Only the first two moments are invariant under translations. The mean is constant and the covariance only depends on the separation \vec{h} but not on the location \vec{x} . Thus, both moments are homogeneous in space:

$$E[Z(\vec{x})] = m \quad (2.1)$$

$$E[Z(\vec{x} + \vec{h}) \cdot Z(\vec{x})] - m^2 = \text{Cov}(\vec{h}). \quad (2.2)$$

Since a Gaussian distribution is completely defined by its first two moments, the mean and the covariance function suffice to determine the

spatial distribution of a Gaussian random function. Hence second-order stationarity is equivalent to full stationarity (Chilès and Delfinier, 1999).

- **Intrinsic hypothesis:** The expectation E of the random function Z is constant and corresponds to the mean and the increment $[Z(\vec{x}+\vec{h})-Z(\vec{x})]$ has a finite variance which depends on \vec{h} but not on \vec{x} :

$$E[Z(\vec{x})] = m(\vec{x}) = m \quad (2.3)$$

$$\begin{aligned} \text{Var}[Z(\vec{x}+\vec{h})-Z(\vec{x})] &= \\ E\left[\left(Z(\vec{x}+\vec{h})-Z(\vec{x})\right)^2\right] &= 2\gamma(\vec{h}), \end{aligned} \quad (2.4)$$

with γ being the semivariance.

Second-order stationarity implies the intrinsic hypothesis but the reverse is not true (Journel and Huijbregts, 1978).

2.3 Frequency Distribution of Data – Normal Score Transform

Beside the spatial correlation of data, geostatistics also describes the basic statistic properties as the mean, the variance or the complete frequency distribution. The distribution can either be described by the probability density function (PDF) or the cumulative density function (CDF). In many cases, earth-science data do not represent a normal distribution, log-normal or other distributions are prevalent, too.

When comparing several distributions, i.e. a measured distribution to a model function, one can either compare the whole distribution or restrict to some typical values which describe the characteristics of the curves. The first three moments of a statistical distribution are the mean m , the variance σ^2 and the skewness γ_3 .

- The arithmetic **mean** is defined as:

$$m = \frac{1}{N} \sum_i \xi_i, \quad (2.5)$$

where ξ_i are the data and N is the number of values.

- The **variance** is a measure of statistical dispersion describing how the values spread around the mean:

$$\sigma^2 = \frac{1}{N} \sum_i (\xi_i - m(\xi))^2 . \quad (2.6)$$

- The **skewness** γ_3 is a measure of asymmetry of the data around the sample mean. The skewness of a symmetric distribution is zero as e.g. is the case for a normal distribution. If it is negative, the data are spread out more to the left of the mean. When it is positive, the data are spread out more to the right. The skewness is defined as:

$$\gamma_3 = \frac{\sum_i (\xi_i - m(\xi))^3}{N \sigma^3} . \quad (2.7)$$

As a normal distribution forms the basis of most statistical analysis techniques, the data often have to be trimmed to a normal distribution before being analysed. In case of a log-normal original data distribution, this is trivial as just the logarithmised variable has to be considered. In case of a more complicated distribution, which can not be described by an analytic expression, the data have to be transformed by a non-linear transformation $G = \Phi(F)$ referred to as normal score transform or Gaussian anamorphosis (Olea, 1999). First, the original data are ranked and then the corresponding quantile is assigned to the corresponding quantile of a standard normal distribution (Fig. 2.1). Thus, a list is provided which transfers every datum of the original data to a datum corresponding to a standard normal distribution.

The transformation $F = \Phi^{-1}(G)$ is used to transform the data back, which have been processed as normally distributed data. The back transformation can also be used to generate a non-normal distributed variable, i.e. for trimming a normal distributed variable generated by geostatistical simulations to any other distribution.

2.4 Spatial Correlation of Data

The analysis of spatial variability provides the information what an observation at one point tells us about the value at a neighboring point. One of the basic geostatistical tools is variogram analysis. The variogram describes how the values at two points become different as the separation between these points

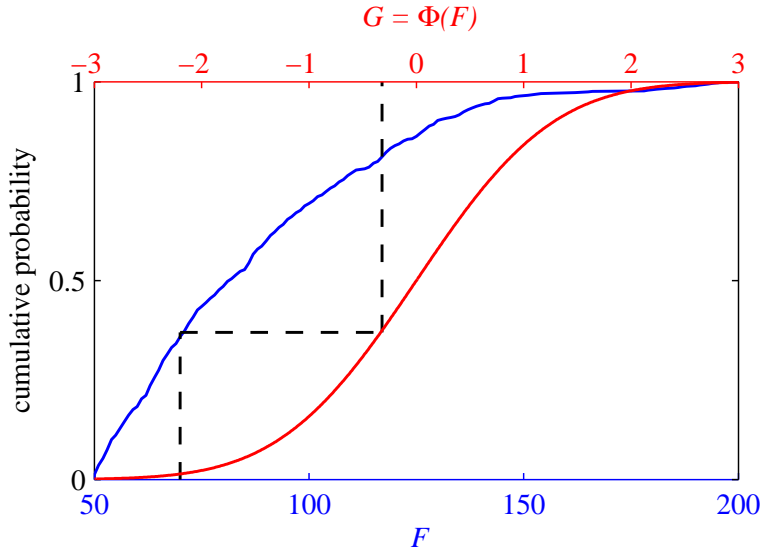


Figure 2.1: Schema of the normal score forward transformation $G = \Phi(F)$. The blue line corresponds to the original data F , the red line to a standard normal distribution G , and the dashed line displays the transformation path.

increase. Let Z be an intrinsic random function in a field then the semivariance γ is (Olea, 1999):

$$\gamma(\vec{h}) = \frac{1}{2} \text{Var}[Z(\vec{x}) - Z(\vec{x} + \vec{h})], \quad (2.8)$$

with \vec{x} being the location and \vec{h} the separation vector between variable pairs. The semivariance describes the difference of data with increasing distance as opposed to the covariance which describes the semblance of data depending on the distance. They behave contrarily and are related one to another:

$$\gamma(\vec{h}) = \text{Cov}(0) - \text{Cov}(\vec{h}). \quad (2.9)$$

In geostatistics, the use of the semivariance is preferred to the covariance because it requires a less stringent assumption for its existence and it is less sensitive to a drift or a constant added to the random function. The semivariance γ plotted against the lag distance h is the semivariogram (Fig. 2.2) which describes the spatial correlation of the variable. At small lag distances the values are correlated and the difference and thus the semivariance is small. With increasing distance, the semivariance rises as the values correlate less and reaches a plateau indicating that there is no correlation any more and the values are independent. The distance at which the plateau is reached is called

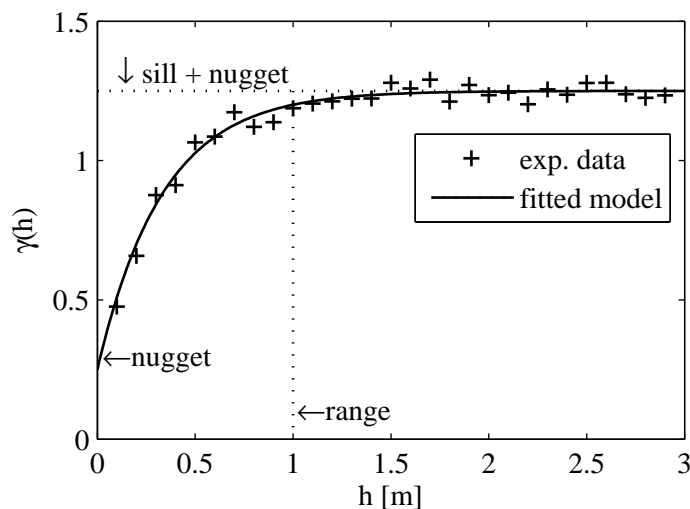


Figure 2.2: Exemplary experimental semivariogram and fitted model: the characteristic parameters sill, range and nugget are depicted.

the range a and the height of the plateau is the sill and corresponds to the ordinary or a priori variance σ^2 of the dataset with σ being the standard deviation. The range corresponds to the correlation length of a variable distribution and denotes the average distance at which the data barely correlate.

One would expect the semivariogram starting at the origin as two values at the same location ($h = 0$) are identical. If the semivariance does not vanish for $h \rightarrow 0$, one will be concerned with a nugget effect. A nugget effect can be caused by either a statistical error in measurement of the analysed variable or micro-variability which is not resolved by the measurement, e.g. if the sampling distance is larger than the typical scale of the micro-variability. If there is a nugget, the height of the semivariogram plateau corresponds to the sill plus the nugget. In practice, we do not know the semivariance but can estimate it from the spatial variable distribution $F(\vec{x})$:

$$\gamma(\vec{h}) = \frac{1}{2N(\vec{h})} \sum_{i=1}^{N(\vec{h})} (F(\vec{x}_i) - F(\vec{x}_i + \vec{h}))^2, \quad (2.10)$$

where i is the sample index and N the number of pairs which are separated by the distance vector \vec{h} . If the semivariance only depends on the absolute lag distance h but not on the direction, the semivariogram is considered to

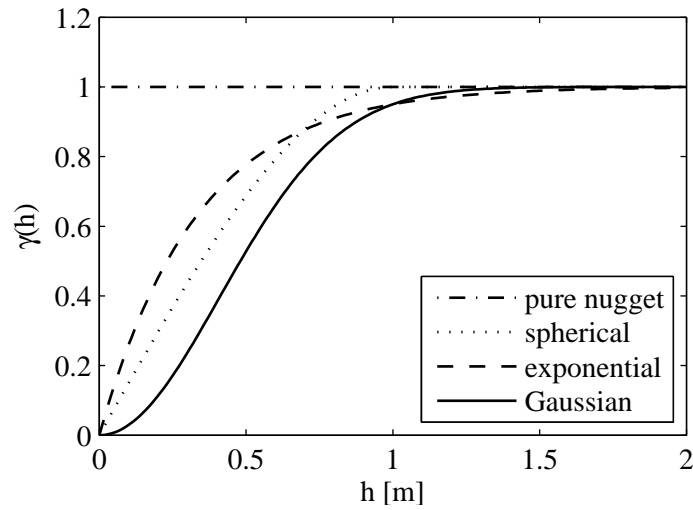


Figure 2.3: Some basic variogram models (sill $C = 1$, range $a = 1$ m): pure nugget effect, spherical, exponential and Gaussian model.

be isotropic and an omnidirectional semivariogram can be used. In case of anisotropy one has to calculate the semivariogram for different directions.

Definition 2.10 requires the random variable to be intrinsically stationary which implies that the mean is constant. In case of an external drift, i.e. a systematic variation of the mean, the semivariogram will not become stationary and no plateau will be reached. A proper semivariogram estimation requires the removal of this drift from the data (Olea, 1999).

For practical applications, when the data are not located regularly along the direction for which the variogram should be calculated or when the data are located totally irregularly, the lag-distance vectors are grouped into classes in analogy to the classes of a histogram. Thus, one has to define a distance and an angular tolerance inside which the data are grouped together.

The next step after calculating the experimental variogram is to fit a model which will be used e.g. for kriging the data or to simulate a statistical data distribution. The most common models are defined in the following and are plotted in Fig. 2.3 (Goovaerts, 1997). Complicated variogram structures can be fitted by superposing several basic models.

The **pure nugget effect** is

$$\gamma(h) = C_0 \quad (2.11)$$

and means that there is no spatial correlation of the data in the observed range. The distribution of the variable in space is purely random.

The semivariance of the **spherical model** rises linearly from the origin and reaches the sill C at the range a .

$$\gamma(h) = \begin{cases} C \left(\frac{3h}{2a} - \frac{1}{2} \left(\frac{h}{a} \right)^3 \right) & \text{if } 0 \leq h < a \\ C & \text{if } h \geq a \end{cases} \quad (2.12)$$

The semivariance of the **exponential model** rises linearly from the origin and approaches the sill C asymptotically. The practical range a is defined as the distance at which the semivariance holds 95% of the sill ¹.

$$\gamma(h) = C \left(1 - \exp \left(\frac{-3h}{a} \right) \right) \quad (2.13)$$

Within the **Gaussian model** ² the semivariance also approaches the sill asymptotically and the practical range a is defined as above. As opposed to the exponential model, the graph has a parabolic form at the origin, i.e. it rises slowly at short lag distances. This behaviour is typical for continuous variables like groundwater tables or the temperature distribution in the subsurface.

$$\gamma(h) = C \left(1 - \exp \left(\frac{-3h^2}{a^2} \right) \right) \quad (2.14)$$

2.5 Geostatistical Simulation

As opposed to kriging, geostatistical simulations do not have a smoothing effect but the characteristic small-scale variability will be reproduced. Every simulation provides an alternative but equiprobable realisation. The simulation reproduces the probability density and the spatial correlation of the variable. When carrying out a conditional simulation, the simulated values will match

¹In some software packages, a theoretical range a_{th} is used which is the distance at which a tangent line to the curve at the origin intersects the sill. The theoretical range is one third of the practical range $a_{th} = a/3$ and the semivariogram value is at approximately 63% of the sill. One has to take care which definition of the range is used. In the following, the range of an exponential or Gaussian model is the practical range.

²The Gaussian variogram model is not to be confounded with the Gaussian distribution function. The former describes the spatial correlation of a random variable whereas the latter describes the frequency a value of a random distribution is taken.

the measured values at the sampling locations, too. Thus, the input parameters for a geostatistical simulation are the distribution function, the spatial correlation of the variable in terms of the variogram, and the values at the sampling locations in case of a conditional simulation.

There are a variety of simulation algorithms, whereof the sequential Gaussian simulation `sgsim` (Deutsch and Journel, 1998) is used in the following due to its rapidness and its potential to simulate large fields. Simulated annealing techniques are more flexible and are able to reproduce the input parameters more accurately but are much slower than sequential simulation algorithms. As only a normal distribution can be simulated and most earth-science data do not present Gaussian histograms, the data often have to be transformed after simulation. An inverse normal score transform can be used to adopt the simulated data to the desired density functions.

In comparison to the model assumptions, every realisation will feature some difference in the statistical distribution and the spatial correlation of the data, referred to as ergodic fluctuations (Goovaerts, 1997). The larger the size of the simulated field is compared to the correlation length, the more exactly the model parameters are reproduced by the simulated model. Thus, when using relatively small fields expanding only some few correlation lengths, which may often be the case, several simulations should be run and compared. The realisation featuring the best fit to the input model should be used for further calculations. Figure 2.4 shows the experimental density function and the experimental semivariograms of 6 individual realisations of a geostatistical simulation of a regionalised variable $F(x, y)$ using a sequential Gaussian simulation. The size of the field is 10 m \times 10 m and a standard normal distribution was simulated assuming an exponential variogram with a correlation length of $a = 0.5$ m and 2 m, respectively. One can recognise the individual realisations fluctuating around the model assumptions. The discrepancy between the realisations and the input model are higher in case of the larger correlation length $a = 2$ m which corresponds to one fifth of the simulated field size.

2.6 Determining an Optimal Sampling Configuration

In this section, an appropriate spatial sampling configuration will be determined. If maps of a regionalised variable are to be plotted, a regular grid is

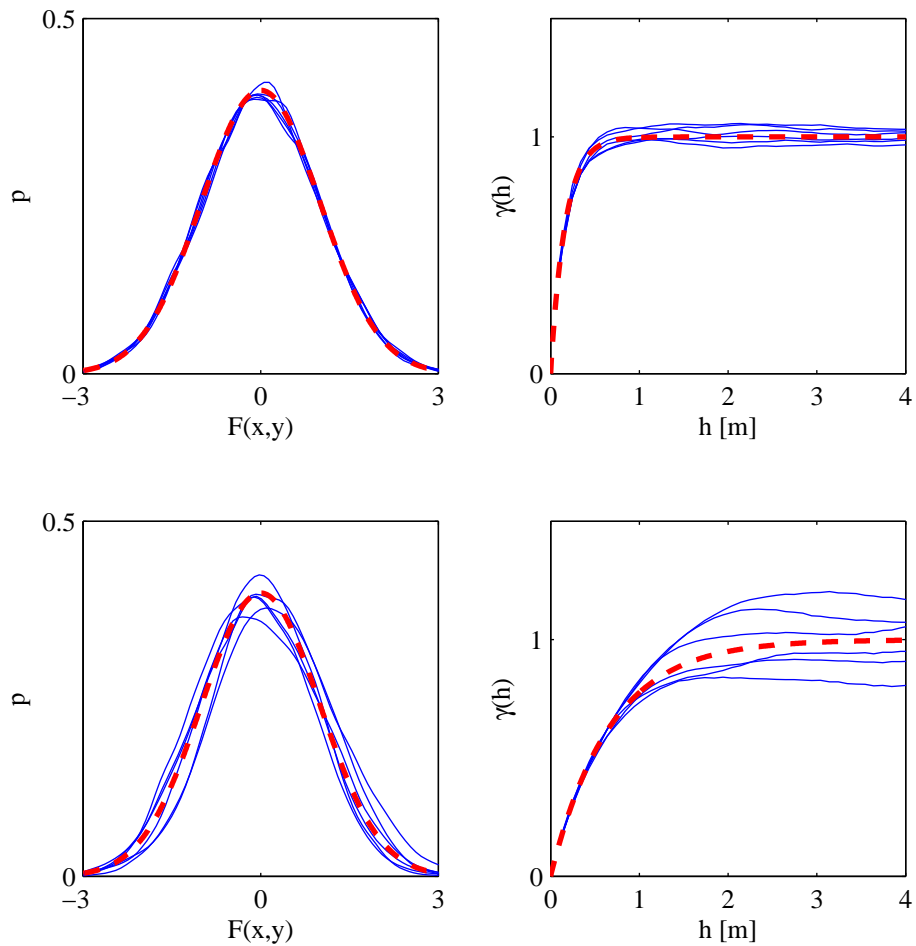


Figure 2.4: Experimental density function and variogram of six realisations of a statistical simulation on a $10 \text{ m} \times 10 \text{ m}$ area illustrating ergodic fluctuations. The model function used for the simulation was: standard normal distribution and exponential variogram model (upper graphs: range $a = 0.5 \text{ m}$, lower graphs: $a = 2.0 \text{ m}$). The dashed red line is the model function and the blue lines are the experimental values of the six realisations.

the first choice since the overall interpolation error becomes minimal. However, the aim of this work is not to produce accurate maps of a variable distribution, e.g. the electric conductivity distribution on an acre to distinguish sandy and clayey areas. The aim is to acquire the statistical properties of the spatial distribution of this variable in terms of the density function and the variogram.

A pragmatic way to determine an optimal sampling configuration is to test different setups on simulated data with statistical properties corresponding to the expected field data. Several configurations emulating geophysical measurements are applied to the synthetic parameter distribution. Then, the geostatistical properties i.e. the mean, the frequency distribution, and the semivariogram of the emulated measurements will be compared to the properties of the exhaustive geostatistical simulation. The aim is to get a good approach of the estimated statistical properties using as few measured data as possible.

In this chapter, the geophysical measurement itself will not be simulated i.e. the spatial resolution or optimal setup of the particular geophysical methods will not be considered. This will be done in the next chapters where geophysical measuring techniques are discussed. At first, the spatial distribution of sampling points and its influence on the deduced statistical parameters is analysed in a general form.

2.6.1 Generation of a Synthetic Spatial Variable Distribution

As variabilities in the range of decimetres up to a few metres are of interest in this work, different sampling setups are emulated inside an area of $10\text{ m} \times 10\text{ m}$. The regionalised variable was simulated with a grid-node distance of 0.1 m assuming a standard normal distribution with no spatial anisotropy. Three different correlation lengths (0.2, 0.5, and 2 m) were used which cover typical dimensions for small-scale variabilities of electrical properties in soils as will be shown later. Figure 2.5 shows the results of the simulations using an exponential and a spherical variogram model for comparison. The spherical model leads to a less diffuse spatial distribution than the exponential. The latter is used for further analysis due to its simplicity and its good accordance with the pattern of electrical soil properties as will be shown by the field measurements.

About 20 individual realisations with the exponential variogram model were calculated and the one featuring the best fit with the model functions is used for the following analysis. Figure 2.6 shows the experimental density function

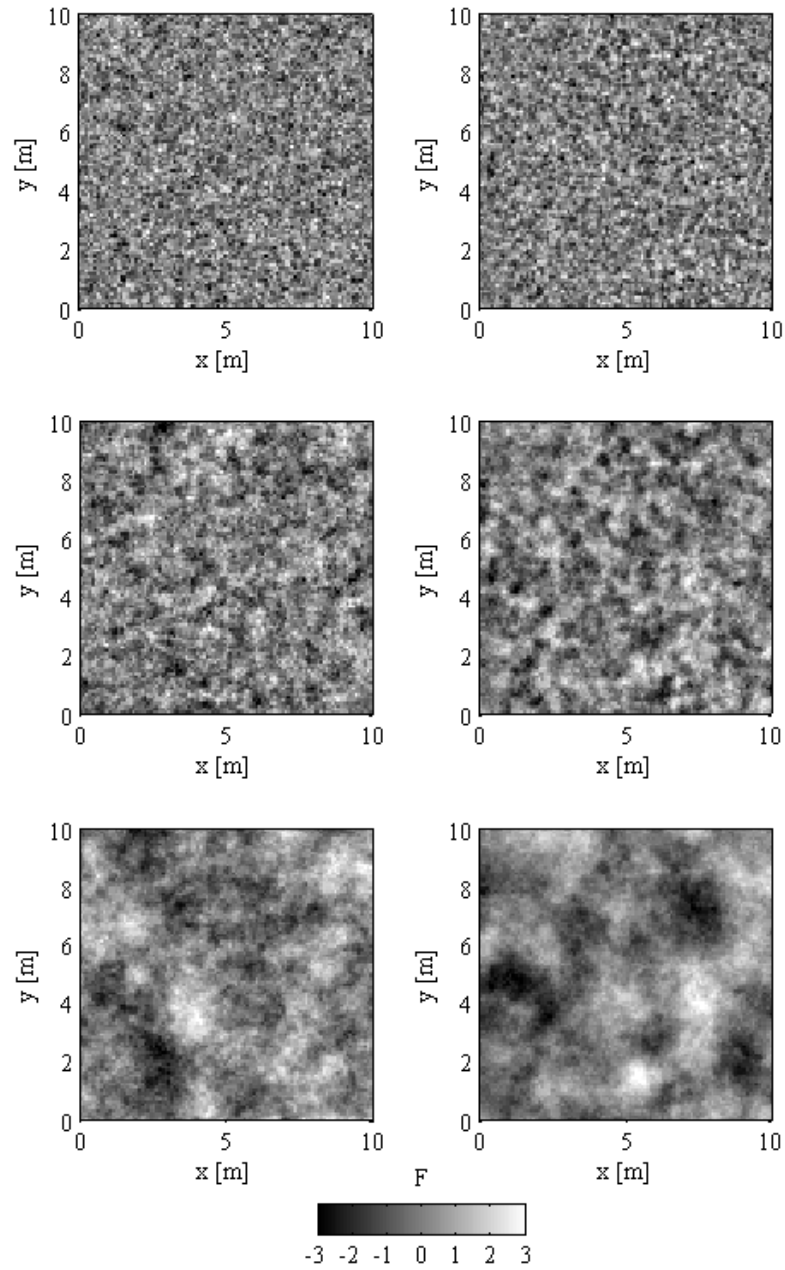


Figure 2.5: Simulated data distribution $F(x, y)$ in an area of $10\text{ m} \times 10\text{ m}$ (sequential Gaussian simulation, standard normal distribution). From top to bottom: correlation length $a = 0.2, 0.5,$ and 2.0 m ; left side: exponential variogram model; right side: spherical variogram model.

and variogram of this best-fit simulation as well as the input parameters, i.e. a standard normal probability density function and an exponential variogram with correlation length of $a = 0.2, 0.5$ and 2 m. One can note that both input functions are well reproduced by the functions which were experimentally determined from the simulated data.

2.6.2 Sampling Configurations

Some different sampling setups are depicted in Fig. 2.7. They are composed of individual profiles with minimal sampling intervals of 0.1 m as most geophysical methods are linked to measuring profiles. The sample points are placed on a 0.1 m grid so that their locations coincide exactly with the location of the simulated data points and therefore no interpolation has to be carried out. The number of sampling points is approximately 800 for all setups so that they are comparable. In addition to the regularly arranged sample points, a random distribution is used for comparison even though such field measurements will not be easy to carry out with most geophysical measuring methods.

2.6.3 Reproducibility of the Distribution Function

When sampling an area, first of all the mean and the standard deviation or, in the ideal case, the complete experimental distribution function of the variable have to be reproduced. The results of the extractions are exemplary shown for the simulated data using an exponential variogram with a correlation length of 2 m (Fig. 2.8). The experimental distribution functions resulting from the extracted data points are plotted as well as the distribution of the exhaustive simulated data with a grid-node spacing of 0.1 m. The distribution functions for the shorter correlation length (0.2 m and 0.5 m) are depicted in Fig. A.1 and A.2. Setup a and b which represent a sampling confined to a relatively small area (Fig. 2.7) yield a poorer approximation of the distribution function than the setups where the sampling points are distributed over the whole area. In order to quantify the deviations between the distribution functions of the extracted data and the exhaustive field, some values which characterise a distribution are compared. The mean, median, standard deviation and skewness are calculated for the extracted data as well as the exhaustive simulated data

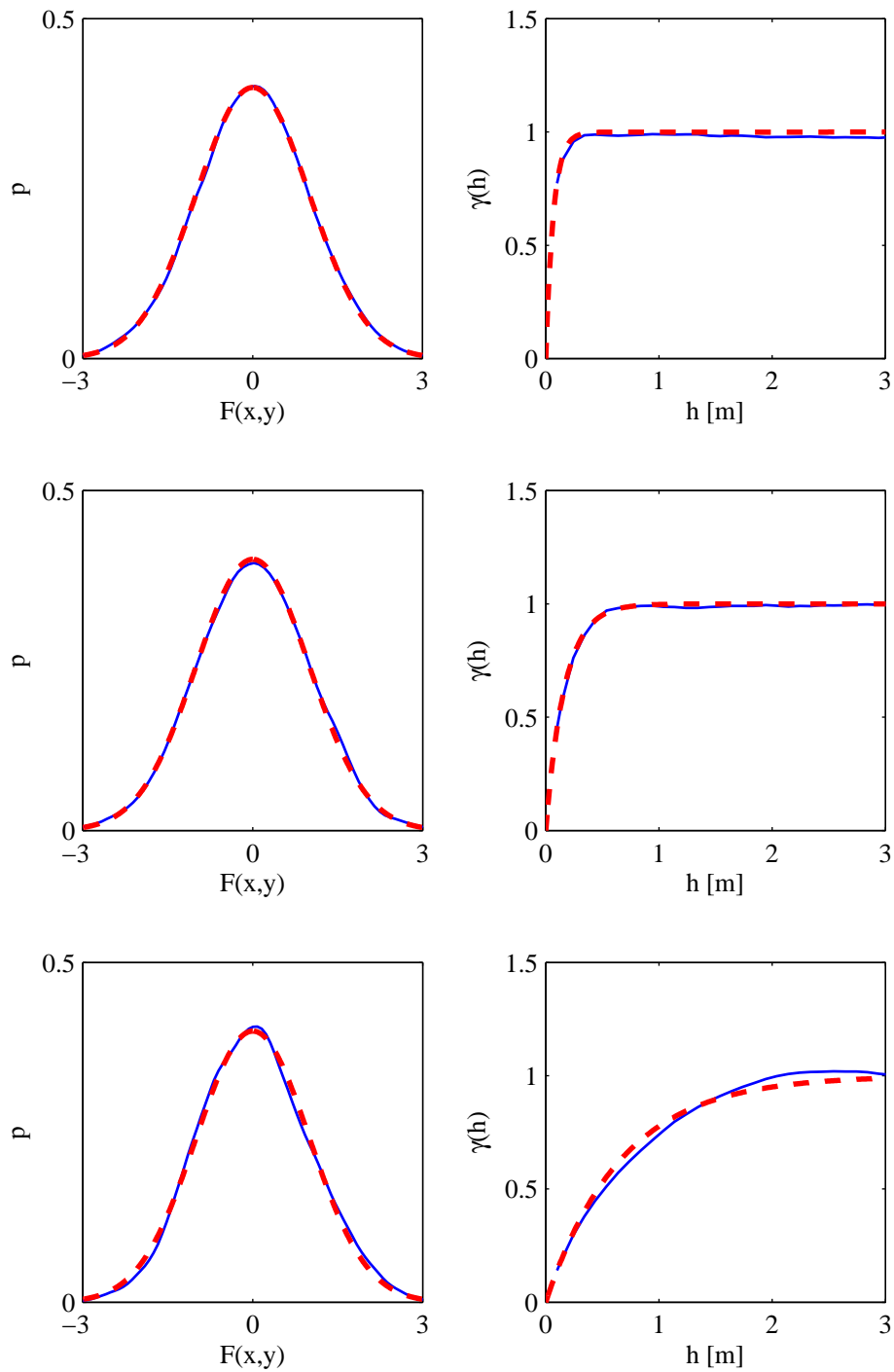


Figure 2.6: Experimental density function and variogram of the best-fit simulations with exponential variogram structure and correlation lengths of $a = 0.2, 0.5,$ and 2 m which are depicted to the left in Fig. 2.5 (blue line) and input parameters used for the simulation (red dashed line).

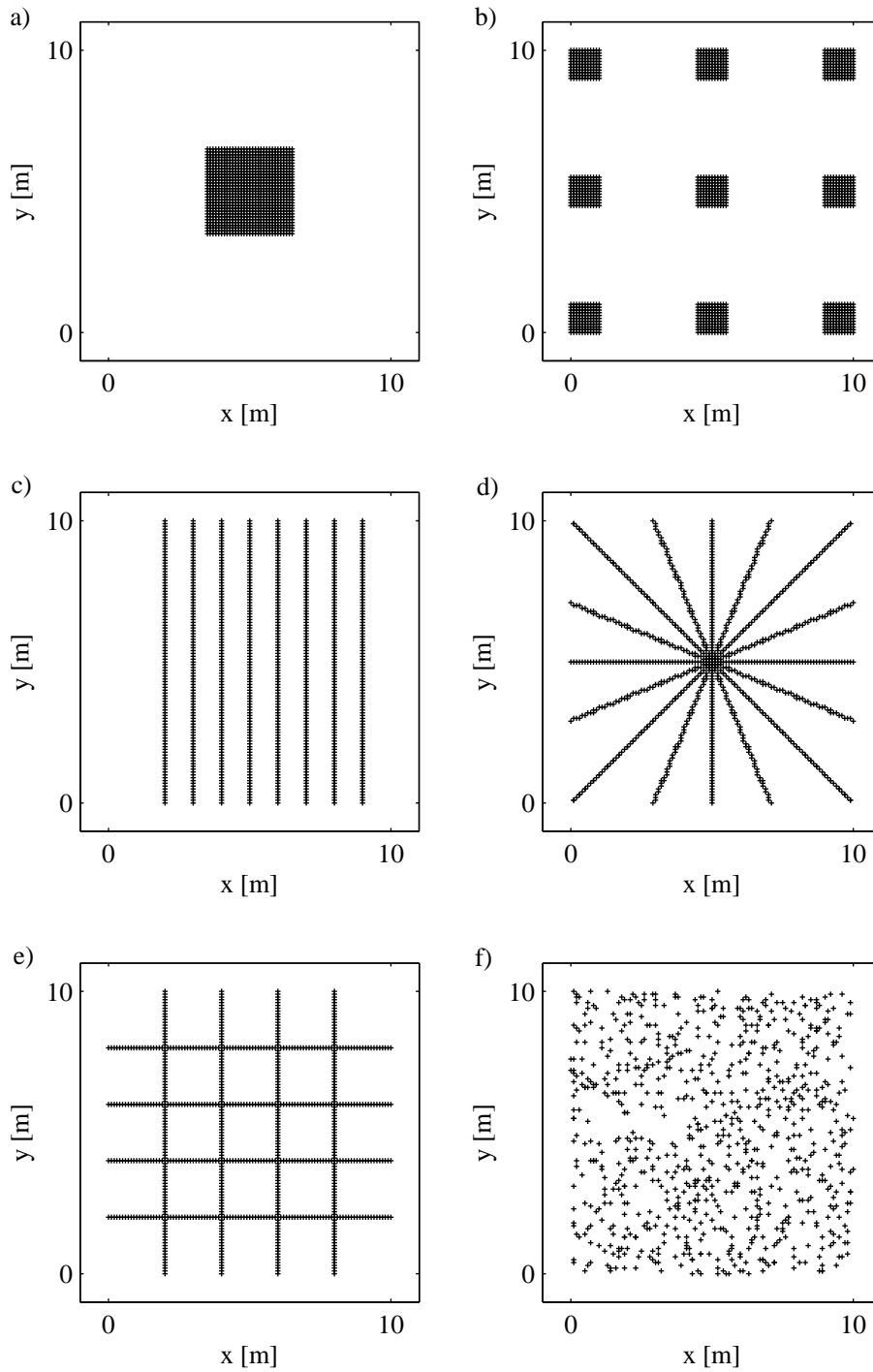


Figure 2.7: Different setups for data sampling, all consisting of approximately 800 samples: 3 m \times 3 m square (a), 9 squares of 1 m \times 1 m (b), 8 parallel lines (c), 8 crossing lines (d), grid of 4 \times 4 lines (e), and random (f). The spacing along the lines or inside the squares is 0.1 m.

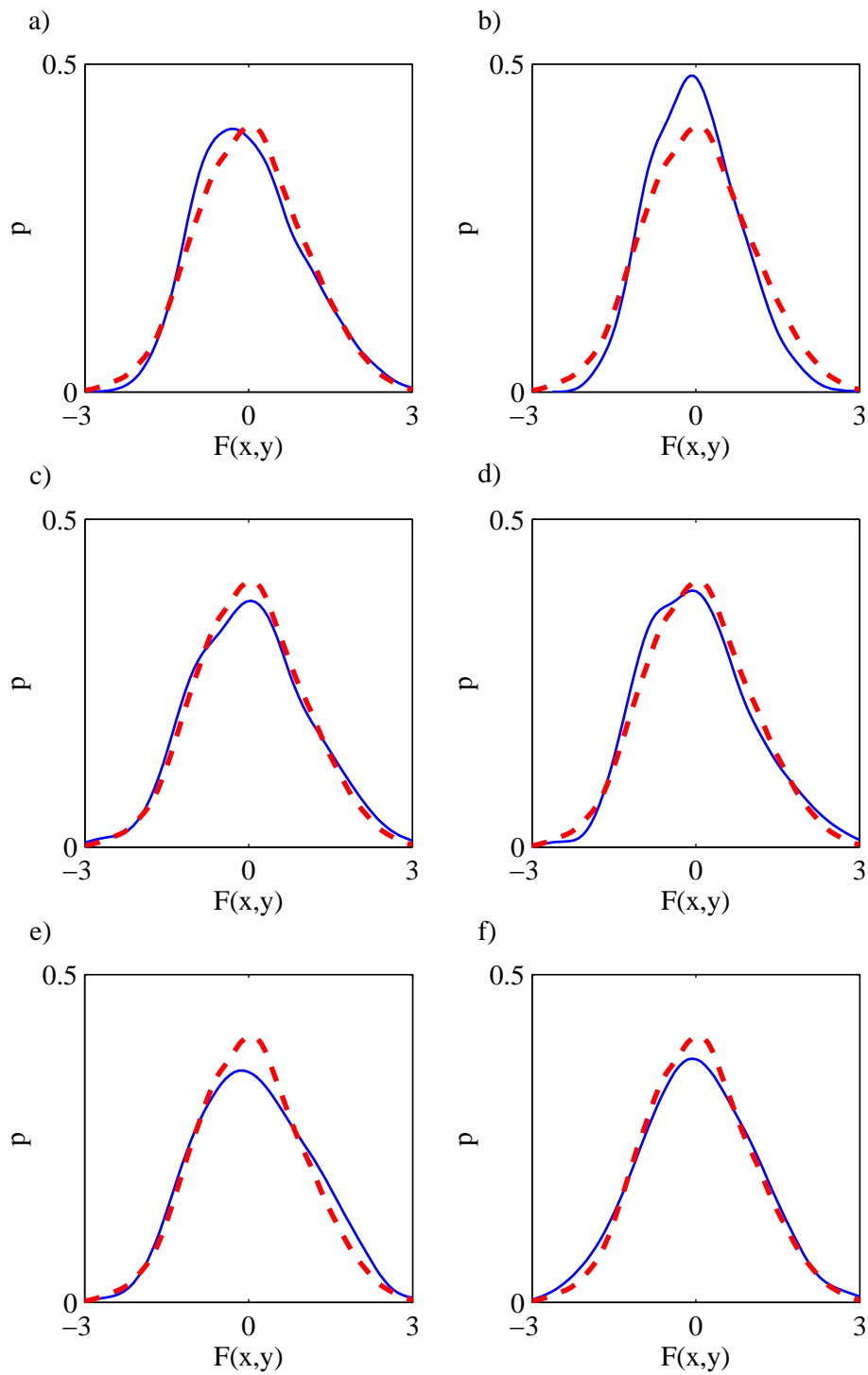


Figure 2.8: Experimental distribution functions of the extracted data (blue solid line) and distribution function of the exhaustive dataset (red dashed line). The random variable was simulated using a standard normal distribution and an exponential semivariogram with $a = 2$ m.

and the absolute deviance³ is depicted in Fig. 2.9.

At large correlation lengths setup a, b and d show the poorest fit to the desired function. Setup a and d have large skewness deviations i.e. the density function is asymmetric pretending a log-normal distribution. Setup b leads to a high deviance of the mean, median and standard deviation which manifests in a shifted and scarped distribution function.

At shorter correlation length (0.2 m and 0.5 m) the differences are not that distinct and all setups yield suitable results with setup a and f showing the lowest deviations.

2.6.4 Reproducibility of the Spatial Correlation

Besides the distribution function, the spatial correlation in terms of the variogram has to be approached as closely as possible by the sampling configuration. Figure 2.10 shows the experimental variograms of the extracted data for correlation lengths of 2 m.

The variograms of the shorter correlation length (0.2 and 0.5 m) are depicted in Fig. A.3 and A.4. A quantitative description of the deviance between the variograms of the extracted data and the exhaustive data is not as simple as is the case for the characteristic values describing the distribution function. A simple RMS deviation between the experimental data and the reference variogram will not adequately describe the fit as the rise of a variogram is much more important than the tail because it defines the deduced correlation length. Therefore, we rely on a qualitative visual valuation of the deviation of the experimental variograms.

When analysing the data with 2 m correlation length, the sampling configurations consisting of several profiles c, d and e provide much better results as larger lag distances are maintained and a larger area is sampled. At low correlation lengths, configuration a yields the best fit because a regular squared grid provides the most data pairs with short lag distances in various directions. But at larger correlation lengths, this layout as well as layout b fails and the variogram will not represent the true correlation length. The random distribution f yields suitable results at all three correlation lengths.

³The relative deviations cannot be calculated as the mean, the median and the skewness of a standard normal distribution are equal to zero.

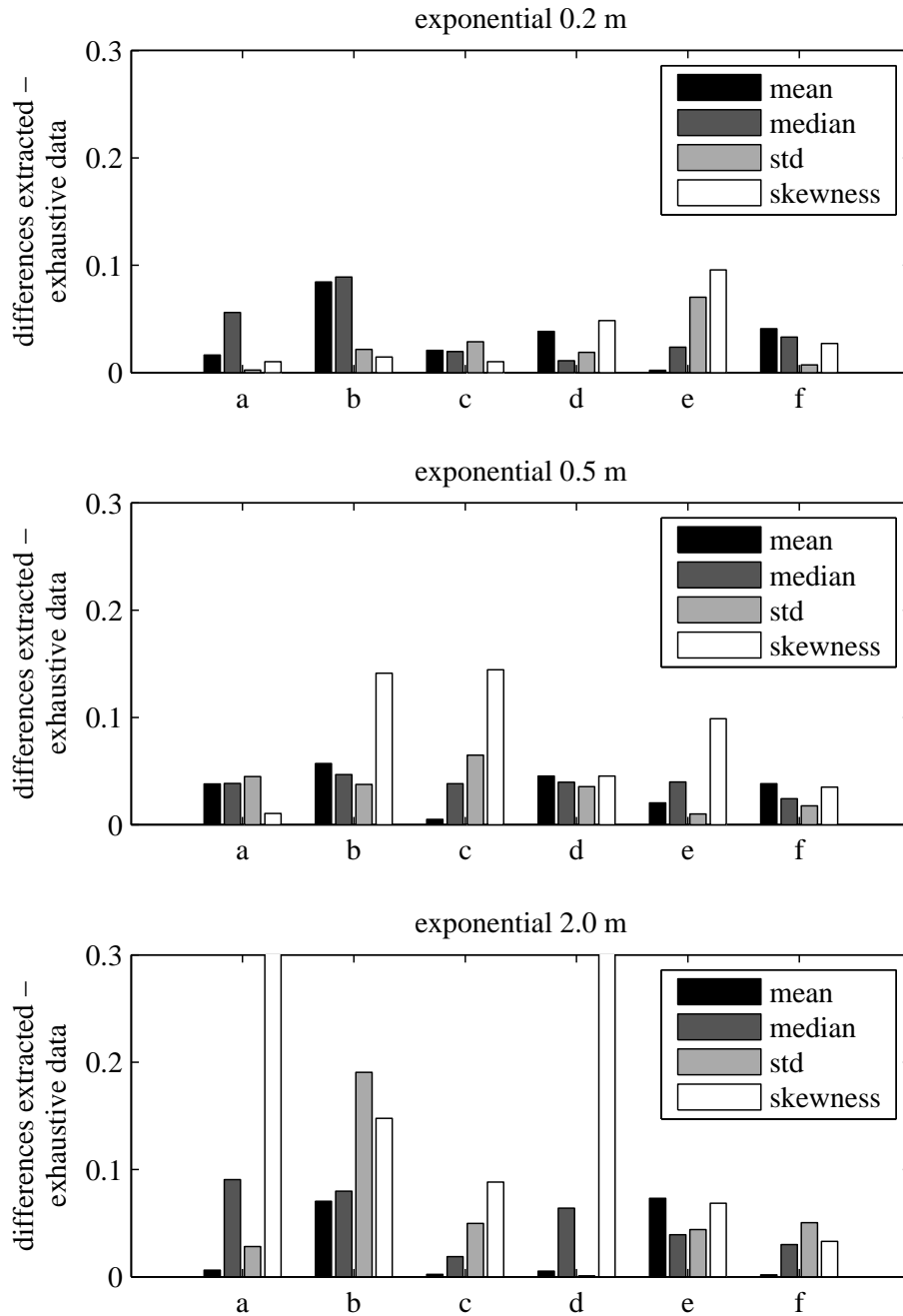


Figure 2.9: Summarisation of typical statistical parameters describing the distribution function: mean, median, root mean square deviation (std) and skewness. The absolute difference between the parameters of the extracted data (setup a–f, Fig. 2.7) and the parameters of the exhaustive data is depicted for an exponential model and three different correlation lengths (Fig. 2.5, left side).

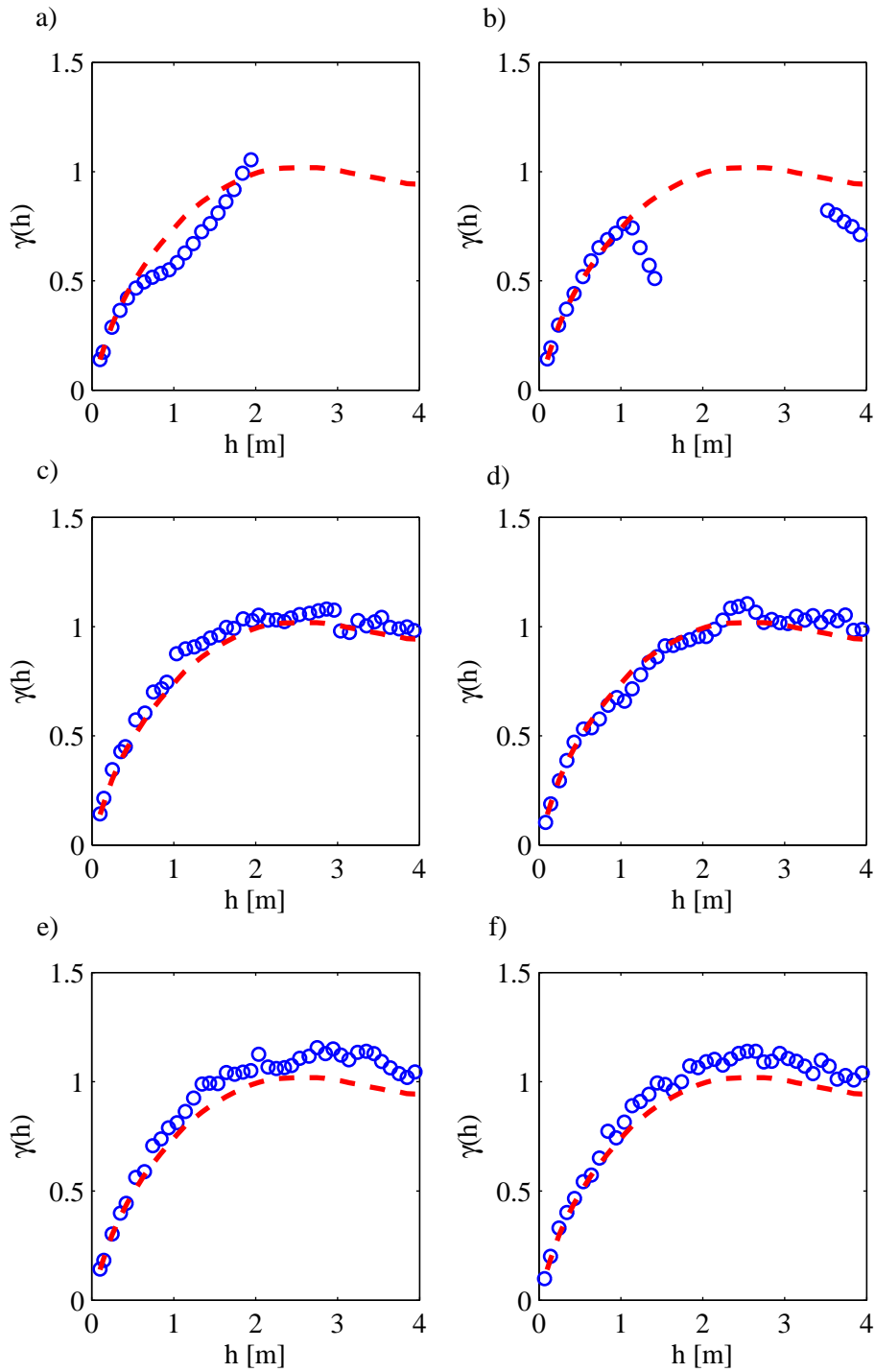


Figure 2.10: Experimental variograms of the data extracted with the setups of Fig. 2.7 (blue circles) and variograms of the exhaustive dataset sampled with a 0.1 m grid (red dashed line). The random variable was simulated using a standard normal distribution and an exponential semivariogram with $a = 2$ m.

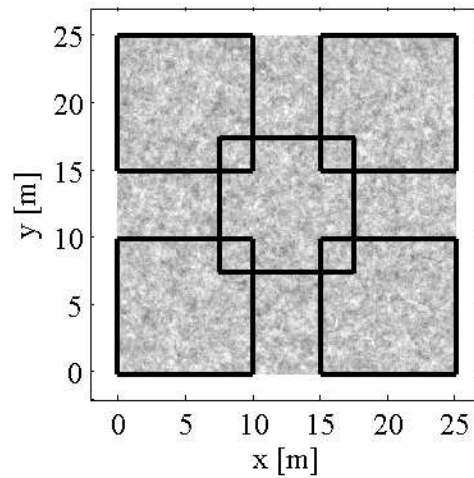


Figure 2.11: Simulated variable distribution (correlation length $a = 0.5$ m) and 5 different locations used to extract a part of the data using the layouts depicted in Fig. 2.7.

2.6.5 Repeatability

A single geostatistical simulation describes only one possible realisation of the random variable among numberless. Thus, the results of 2.6.3 and 2.6.4 are affected by some hazard. In other words, the results depend on the location of the sampling configuration inside the analysed area. A good sampling configuration will cause only little variations in the determined statistical parameters when its location in field is modified. In order to analyse these effects, the variable distribution on an area of $25 \text{ m} \times 25 \text{ m}$ was simulated with a correlation length of 0.5 m . The data were extracted while the sampling configuration was placed at 5 different locations inside the simulated field, that is to say in the centre and the edges of the field (see Fig. 2.11). Figures 2.12 and 2.13 show the results of the geostatistical analysis for the configurations of Fig. 2.7 in terms of the experimental PDFs and variograms at the five positions. The setups with less variations in the deduced density function are c, e and f. The best fit to the variogram of the exhaustive simulated data and the most stable results are obtained with setup e.

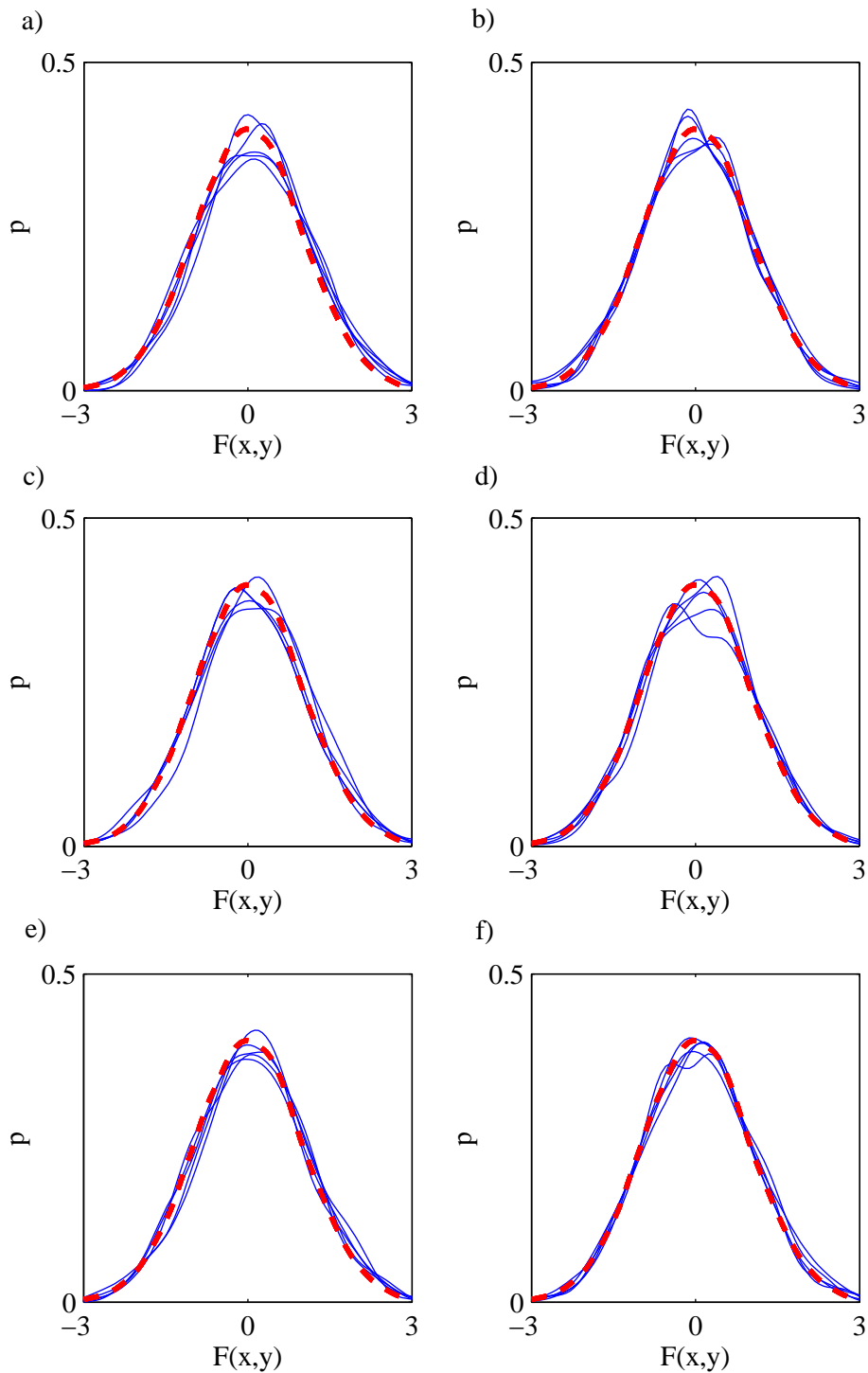


Figure 2.12: Repeatability of sampling: The experimental PDF is depicted for 5 different locations of the sampling configuration inside the simulated field (blue line). The dashed red line is the PDF of the exhaustive simulated field of $25\text{ m} \times 25\text{ m}$ (exponential model with $a = 0.5\text{ m}$).

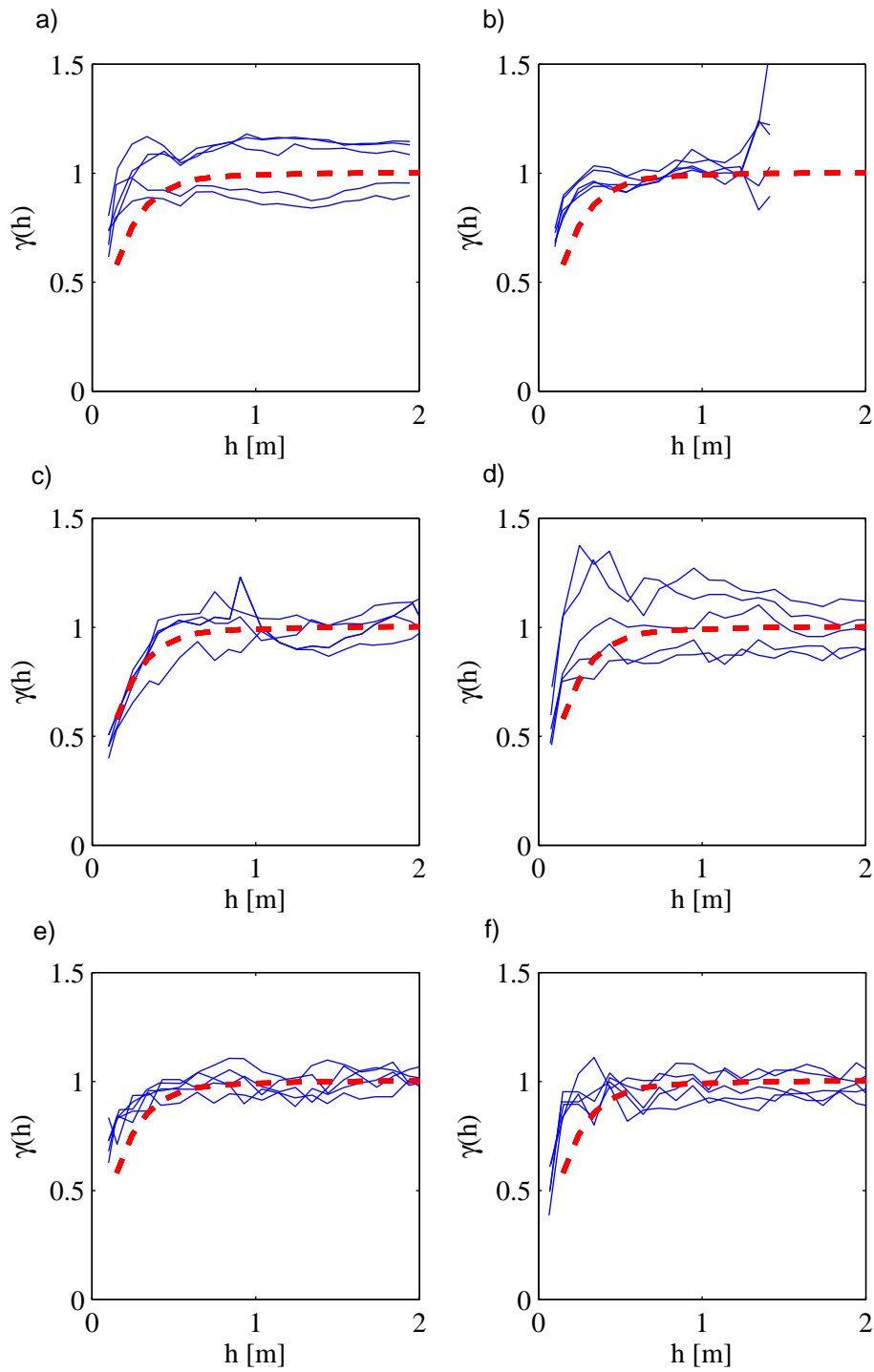


Figure 2.13: Repeatability of sampling: The experimental variogram is depicted for 5 different locations of the sampling configuration inside the simulated field (blue line). The dashed red line is the variogram of the exhaustive simulated field of $25 \text{ m} \times 25 \text{ m}$ (exponential model with $a = 0.5 \text{ m}$).

2.6.6 Summary: The Optimal Sampling Layout

The sampling layout affects the statistical properties of the extracted dataset. It acts like a filter. When only a small area is sampled very tightly, one will deduce a shorter apparent correlation length than the real one. Vice versa, when the whole field is sampled, but with large sample distances, one will not detect small-scale variabilities. This is denoted as effect of extend and spacing by Western and Blöschl (1999): "Spacing" refers to the distance between sampling points and "extend" refers to the overall coverage. The apparent correlation lengths always increase with rising spacing and extend. Thus, one has to call into question whether the deduced correlation length is an effect of the sampling layout or represents the true distribution of the sampled variable.

The optimum sampling configuration to determine geostatistical properties of regionalised variables depends on the spatial correlation of the variable itself. But unfortunately, this parameter is not known in advance in most of the cases, but has to be determined by the measurements.

If correlation length is small, a regularly spaced grid provides the best results. But when the correlation length gets longer, this layout is not suitable any more and configurations with the same number of data points which are composed of several longer profiles are appropriate (Fig. A.3 and 2.10).

Configuration e with 4×4 crossing profiles showed to be the most suitable for the range of all correlation lengths between 0.2 m and 2 m and yields the most stable results in terms of different positions of the measuring setup on the analysed area (Fig. 2.12 and 2.13). A random distribution provides good results, too, because it features short lag distances as well as large ones and is uniformly distributed inside the sampling area. But a random sampling configuration is not practicable in most cases when geophysical measurements are carried out.

The results are interpreted and explained as followed. On the one hand, we will need a lot of sampling points close one to another to get numerous data pairs with small lag distances as the shape of the rise of the variogram will mainly define the appropriate variogram model. On the other hand, we need large distances in order to acquire regional trends and large correlation length. A rule of thumb is that correlation lengths up to half of the largest distance inside a sampled field can be resolved. The number of data pairs that can be compared drastically decreases for larger lag distances. For lag distances

larger than half the extent of the field, points in the middle of the sampled area do not have an associate to form a pair and therefore are not taken into consideration. (This is in analogy to the maximal period that can be resolved in time series analysis which corresponds to the length of the time series.)

Moreover, the more equally the points are distributed, the less clustering effects will occur. Clustering is when a region with high or low values is sampled more densely than the rest of the area. Then, the deduced distribution function is not representative for the exhaustive area as is the case in Fig. 2.12 a and d. An appreciation of values has to be found between the amount of needed data and the quality of estimation of the statistical parameters, i.e., the distribution function and the variogram of the regionalised variable.

In the last section an isotropic parameter distribution has been assumed. At scales of a few metres anisotropy in horizontal direction is unlikely to occur in the upper soil if there is no artificial anisotropy, e.g. generated by ploughing or other agricultural conditioning. When anisotropy is likely, the semivariogram has to be calculated for different directions. Then, crossing sections as in Fig. 2.7 d will probably be an appropriate sampling layout as they provide numerous different lag distances in the direction of the individual sections.

Another parameter which has not been considered yet is the support of data which refers to the sampling volume or the area integrated by each measuring method in case of geophysical measurements. A change of support will change the histogram and variogram. When the support is getting larger, the apparent correlation length and the nugget effect will increase. In contrast, the apparent variance will decrease with increasing support (Western and Blöschl, 1999; Chilès and Delfinier, 1999). The effect of support will be analysed in chapter 5 where the different measurement techniques will be evaluated with regard to their ability to determine the statistical properties accurately.

3 Electric Conductivity σ

3.1 Electric Conductivity of Soils

Soil can be described as a 3-phase composite: the solid matrix, the pore fluid and the gaseous pore filling. The solid phase and the aqueous phase both contribute to the bulk conductivity whereas the gaseous phase can be regarded as an isolator. There are three mechanisms of conduction which determine the electric conductivity of geologic materials.

- The **electronic or metallic conductivity** of the matrix is caused by the free electrons in the crystal lattice of the minerals. Most of the rock forming minerals have low conductivities between 10^{-14} and 10^{-10} S/m (Knödel et al., 1997). Only ores and some form of carbon like graphite feature high conductivities. However, these materials are rare in soils so that the conductivity of the soil matrix can be neglected in most cases.
- The **electrolytic conductivity** is caused by the aqueous liquid in the pore space which features dissolved ions. In a large variety of soils it is the basic mechanism which enables conduction. The conductivity of sediments and soils can often be described by an Archie equation (Archie, 1942; Schön, 1996) which relates the bulk conductivity σ to the water saturation S :

$$\sigma = \frac{\Phi^m}{a} \sigma_w S^n, \quad (3.1)$$

where σ_w is the conductivity of the pore fluid, Φ the effective porosity and a the formation factor. The cementation factor m represents the connectivity of the pore space in the fully water-saturated case where the saturation exponent n accounts for the connectedness of the water in the partially saturated case (Knight and Endres, 2006). The parameters a and m have to be determined empirically and can vary between $1.3 < m < 2.4$ and $0.5 < a < 1$. The cementation factor m rises with increasing compaction of the sediment. The factor of saturation n varies between $1.3 < n \leq 2$ and is often set to the value of 2 (Schön, 1996).

- The **surface conductivity** is not determined by the porosity but by the inner surface of the soil. It is associated with the cation exchange capacity of the material which is typically high for clay. The mineral surface is charged negatively and the cations in the pore fluid are attracted by the electrostatic forces. Therefore, the region of the interface mineral–fluid features a concentration of charges and forms an electrical double layer which can highly enhance the electrical conductivity of a material. The double layer contributes significantly to the conductivity of soil if clay content is high. The effective conductivity is often described as a parallel connection of the electrolytic and interface conductivity. Then, the Archie equation can be expanded by the interface conductivity σ_q (Knödel et al., 1997):

$$\sigma = \frac{\Phi^m}{a} \sigma_w S^n + \sigma_q. \quad (3.2)$$

Besides the inner surface of soil, there are several factors which influence interface conductivity as texture, pore-size distribution or pore-space structure.

Electronic and electrolytic conductivity is independent of frequency in a wide range, but interface conductivity often shows a frequency dependence. When current flows through the soil, dissolved ions will accumulate at the place where the pores are narrow and will impede the current. The concentration of charges is time delayed to the applied field due to the inertia of the ions movement. This fact leads to a complex frequency dependent conductivity which is studied with spectral induced polarisation (SIP) measurements e.g. in order to determine the pore-size distribution or contaminations of soil. As the location where the measurements were carried out in this work have vanishing clay content, electrolytic conductivity is the predominant process and conductivity is considered as frequency independent in the following.

Electric conductivity also depends on temperature. With rising temperature more and more ions can be dissolved. The viscosity of water decreases what enhances the mobility of ions. Both effects result in a positive temperature coefficient of soil conductivity, i.e. conductivity rises with temperature.

3.2 Theory of Electric Current Flow

When analysing DC-geoelectric measurements, one can assume stationary fields and therefore the partial derivatives of time in Maxwell's equations van-

ish. This also holds for low frequent alternating currents which are commonly used for geoelectric measurements in order to avoid polarisation of the electrodes. Thus, the curl of the electric field \vec{E} is zero (Eq. (4.17)) and \vec{E} can be described by the gradient of a potential field Φ :

$$\vec{E} = -\nabla\Phi. \quad (3.3)$$

The basic equations describing current flow are Ohm's law:

$$\vec{j} = \sigma\vec{E} \quad (3.4)$$

and the equation of continuity

$$\nabla \cdot \vec{j} = -\frac{\partial}{\partial t} \rho_{el}. \quad (3.5)$$

Here, \vec{j} is the current density and ρ_{el} the electric charge density. All the current which flows into a volume must leave the other side unless there is a source or sink of current and the right side of Eq. (3.5) equals zero:

$$\nabla \cdot \vec{j} = 0. \quad (3.6)$$

This equation holds true for the whole area but not for current sources and sinks. From the above equations follows Laplace's equation for a homogeneous medium:

$$\Delta\Phi = 0. \quad (3.7)$$

One can describe Laplace's equation in polar coordinates (r, φ, ϑ) . If only a single source of current is considered at the surface of a homogeneous half-space, complete symmetry of current flow with respect to the ϑ and φ directions may be assumed. Therefore, the derivatives taken in these directions vanish and Laplace's equation results in (Keller and Frischknecht, 1970):

$$\frac{\partial}{\partial r} \left(r^2 \frac{\partial \Phi}{\partial r} \right) = 0. \quad (3.8)$$

This equation may be directly integrated:

$$\Phi = -\frac{c}{r} + d, \quad (3.9)$$

with the two constants of integration c and d . Defining the potential $\Phi \rightarrow 0$ for $r \rightarrow \infty$ results in $d = 0$. The second constant c is evaluated by determining the total current I of the source as the integral of the current density over a

closed surface S . If the source is placed at the boundary of a homogeneous half-space and the current flows through a half-sphere with the surface $2\pi r^2$, one can deduce:

$$I = \oint_S \vec{j} \cdot d\vec{s} = \oint_S \sigma \vec{E} \cdot d\vec{s} = \oint_S \sigma \frac{c}{r^2} \frac{\vec{r}}{r} \cdot d\vec{s} = -2\pi\sigma c. \quad (3.10)$$

Therefore, the potential function of a point source is:

$$\Phi = \frac{I}{2\pi\sigma r}. \quad (3.11)$$

As potential functions are additive, the resulting potential of several sources is the sum of the individual potential functions. Usually, a four-point setup is used to determine the conductivity of soils in field (Fig. 3.1). A current I is fed into the ground via two current electrodes, A and B, and the potential difference U is determined between two measuring electrodes, M and N. As the source and the sink are defined by opposed currents $I = I_A = -I_B$, the measured voltage is:

$$\begin{aligned} U &= \Phi_M - \Phi_N = (\Phi_{AM} + \Phi_{BM}) - (\Phi_{AN} + \Phi_{BN}) \\ &= \frac{I}{2\pi\sigma r_{AM}} - \frac{I}{2\pi\sigma r_{BM}} - \frac{I}{2\pi\sigma r_{AN}} + \frac{I}{2\pi\sigma r_{BN}}. \end{aligned} \quad (3.12)$$

$$(3.13)$$

The conductivity can thus be determined by the injected current I and the measured voltage U :

$$\begin{aligned} \sigma &= \frac{I}{2\pi U} \left(\frac{1}{r_{AM}} - \frac{1}{r_{BM}} - \frac{1}{r_{AN}} + \frac{1}{r_{BN}} \right) \\ &= \frac{1}{K_{point}} \frac{I}{U} \end{aligned} \quad (3.14)$$

$$\text{with } K_{point} = \frac{2\pi}{\frac{1}{r_{AM}} - \frac{1}{r_{BM}} - \frac{1}{r_{AN}} + \frac{1}{r_{BN}}}, \quad (3.15)$$

where K is the geometric factor which stands for the geometry of the setup. Equation (3.15) is the Neumann formula which serves to calculate the geometric factor of any 4-electrode setup when using point electrodes.

In geoelectrics, it is more common to regard the inverse of conductivity, i.e. the resistivity of the ground:

$$\rho = \frac{1}{\sigma} = K \frac{U}{I}. \quad (3.16)$$

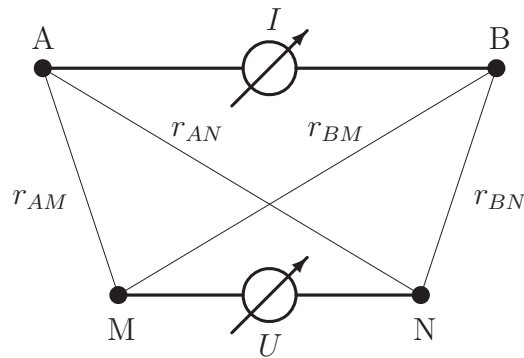


Figure 3.1: Schematic illustration (bird's eye view) of a dc measurement layout using four electrodes. A current is fed into the soil via the electrodes A, B and the voltage is measured via electrode M, N.

If soil is not homogeneous but is layered or features lateral heterogeneities, one will not determine the true conductivity σ or resistivity ρ but an apparent conductivity σ_a or resistivity ρ_a , respectively. The true parameter distribution can be determined by an inversion of the apparent parameter (Loke and Barker, 1996; Friedel, 2000; Günther, 2004).

3.2.1 Influence of Electrode Geometry

When carrying out conventional geoelectrical measurements, the electrodes are usually considered to be point electrodes. When using large electrode separations compared to the electrode length, this approximation is agreeable. But as the electrode separation is getting shorter, the real electrode design will deform the potential lines more and more and the electrodes can no longer be regarded as point electrodes. Thus, corrected geometric factors have to be deduced to convert the measured currents and voltages to apparent resistivities.

In praxis, electrodes can often be approached by elongated half-ellipsoids. The electrical field of an elliptical electrode is the same as the field of a line electrode of the length $2e$ which connects both foci (Sommerfeld, 1967). In analogy to the electrostatic problem of the electric field in the vicinity of a loaded elliptical object, the line source yields the following potential field (Miltzer and Weber,

1985):

$$\Phi = \frac{I}{4\pi\sigma e} \ln \left| \frac{z + e + \sqrt{x^2 + y^2 + (z + e)^2}}{z - e + \sqrt{x^2 + y^2 + (z - e)^2}} \right|, \quad (3.17)$$

where x and y are the horizontal coordinates, z the depth and $e = \sqrt{l^2 - \frac{d^2}{4}}$ is defined by the length l and the diameter d of the electrode. The voltage which is recorded when using a 4-electrode setup can be determined by integrating the potential along the length l of the potential electrodes. For example, the contribution of current electrode A to the potential of electrode M is:

$$\Phi_{AM} = \frac{I}{4\pi\sigma e} \int_0^l \ln \left| \frac{z + e + \sqrt{r_{AM}^2 + (z + e)^2}}{z - e + \sqrt{r_{AM}^2 + (z - e)^2}} \right| dz. \quad (3.18)$$

Thus, the geometric factor for elliptical electrodes is:

$$K_{ell} = \int_0^l \frac{4\pi e}{\ln |f(r_{AM})| - \ln |f(r_{AN})| - \ln |f(r_{BM})| + \ln |f(r_{BN})|} dz \quad (3.19)$$

with $f(r) = \frac{z + e + \sqrt{r^2 + (z + e)^2}}{z - e + \sqrt{r^2 + (z - e)^2}}$

and $e = \sqrt{l^2 - \frac{d^2}{4}}$.

The integral cannot be solved analytically and is calculated numerically. The geometric factors for elliptical electrodes and a radial dipole-dipole configuration are depicted in Fig. 3.2. Two different electrode sizes are used for the calculation. The small electrode is the same as used during the field measurements ($l = 0.03$ m, $d = 0.005$ m) and the large electrodes have the size typically used for standard geoelectric measurements ($l = 0.1$ m, $d = 0.015$ m). The geometric factors for point electrodes are displayed as well for comparison. The smaller the electrode separation, the more K_{point} differs from K_{ell} . For the smallest separation which is used in field ($a = 0.1$ m), the difference between the correct geometric factor and the factor for point electrodes is 7% for the small electrodes and 38% for the standard electrodes. This means that apparent conductivity will be overestimated by 7% or 38% in case point electrodes are assumed instead of considering the true geometry.

The influence of electrode length on the determined conductivities was also analysed in an experiment. A water tank of 2 m \times 1.3 m \times 1.2 m was filled with tap water. An electrode comb of 10 electrodes with a spacing of 0.08 m

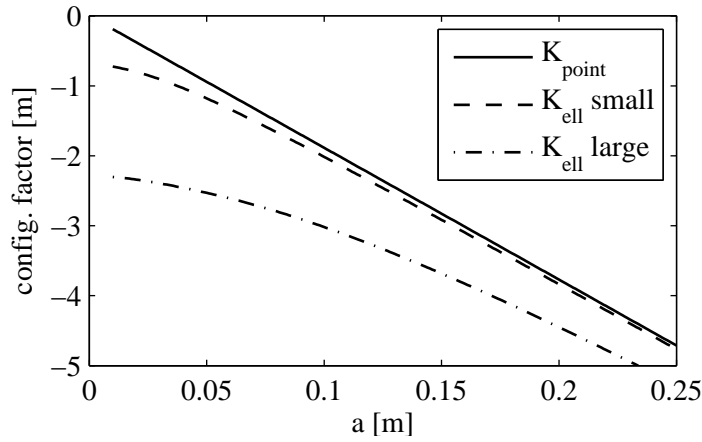


Figure 3.2: Geometric factors for a radial dipole-dipole layout when assuming point electrodes (K_{point}) and elliptical electrodes (K_{ell}). The dipole length is a and the first separation is depicted ($n = 1$). The electrodes dimensions are: $l = 0.03$ m, $d = 0.005$ m (small); $l = 0.1$ m, $d = 0.015$ m (large).

was placed on the water surface (Fig. 3.3). Boundary effects can be neglected as changing the position of the comb towards one of the side walls did not change the measured values. The electrodes had a diameter of 1 mm and the effective electrode length, i.e. the length of the electrodes in water, was step-wise varied from 0 m to 0.1 m. A DC-geoelectric measurement was carried out along the electrode comb using a Wenner and dipole-dipole configuration with an electrode spacing of 0.08 m. The individual readings were averaged in order to minimise the errors caused by small random variations in geometry. Such variations might be different immersion depth or inclinations of the electrodes. In Fig. 3.4 the derived apparent resistivities are depicted using the appropriate geometric factors when assuming point and elliptical electrodes. When using the usual point-electrode factors, one can recognise that one will get wrong conductivities especially when the effective electrode length is large. If the length is 0.1 m, the deviation is up to 50% when using a dipole-dipole configuration. In contrast, when using the geometric factors for elongated electrodes, the deduced conductivities correspond to the conductivity of the medium.

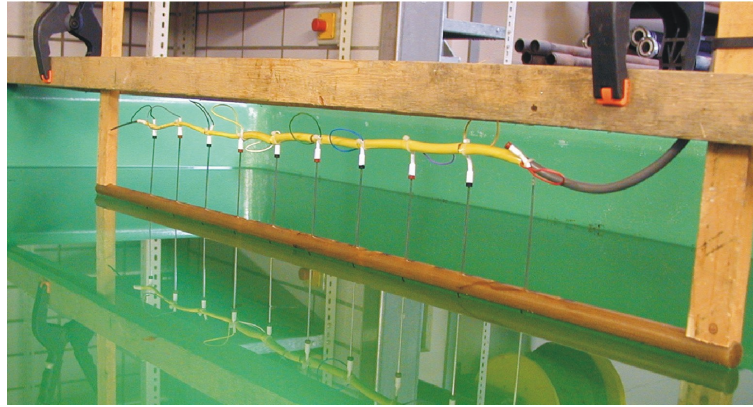


Figure 3.3: Picture of water-tank experiment to determine the influence of electrode length. The electrodes are separated by 0.08 m and can be lowered into the water yielding an effective electrode length of 0–0.1 m.

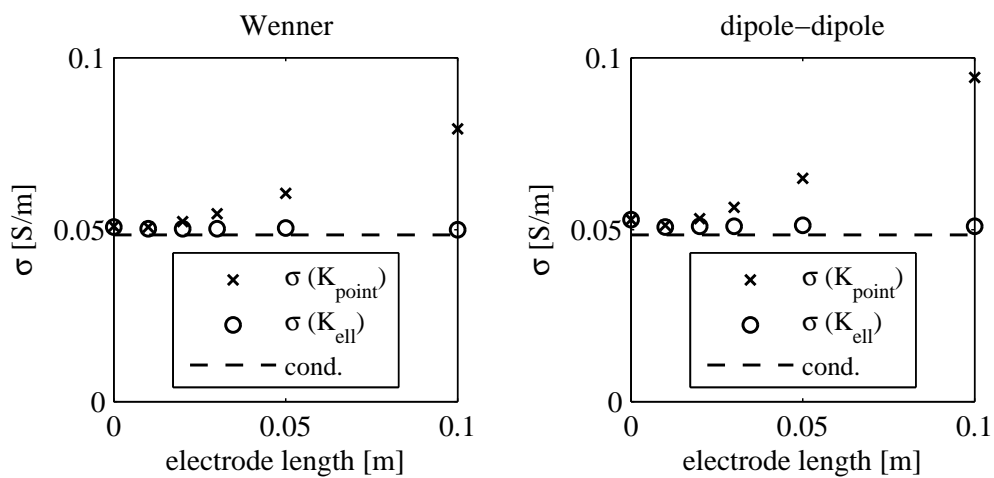


Figure 3.4: Deduced conductivities σ of the water depending on the effective length of the electrodes using geometric factors for point and elliptical electrodes. The electrode spacing was 0.08 m and a Wenner and a dipole-dipole configuration were measured. The real conductivity of the water according to a conductometer is plotted for comparison.

3.3 Determining the Electric Conductivity of Soils

3.3.1 Experimental Setup

There are several setups the electrodes can be placed when carrying out DC-geoelectric measurement all of them featuring different sensitivity to noise and different horizontal and vertical resolution. For practical reasons arrays should be used which can be applied to equidistantly placed electrodes as this enables a quick measuring progress when using modern multi-electrode acquisition systems. As the uppermost region of soil is of interest in this work, the used configurations have to feature high lateral resolution in the near-surface. The dipole-dipole configuration is used as it satisfies best the required features (Stummer et al., 2004) and provides a good measuring progress.

In order to minimise geometrical errors caused by deviating electrode positions, an electrode comb was used. The electrodes have a spacing of 0.1 m and the lengths and diameters are 0.03 m and 0.0045 m. The dipole length was $a = 0.1$ m and dipole separations up to $n = 10$ were used which caused no problems concerning too low voltages.

A resolution analysis (Günther, 2004) yields resolution radii of about 0.05 m at the top surface and rises up to 0.25 m at a depth of 0.5 m.

A 3D measurement on a grid would be the best choice, but only small areas can be measured due to limited number of electrodes and measuring time. Typical areas which can be covered with an appropriate electrode spacing are $1.5 \text{ m} \times 1.5 \text{ m}$. One has to take into consideration that the coverage and resolution is getting worse with increasing depth resulting in a smaller area which can be analysed than the electrode array on the surface. Therefore, 3D measurements will not be large enough for a geostatistical analysis and thus only 2D measurements were carried out along profiles aware of the fact that 3D effects could influence the inversion results. These influences will be analysed in section 5.1.1.

3.3.2 Spatial Field Measurements and Geostatistical analysis

The field measurements were performed on location 1 (see Appendix B) in autumn and the topsoil had a medium water content of $\Theta_V = 16 \text{ vol}\%$. A radial dipole-dipole measurement was carried out along two crossing sections of 15 m

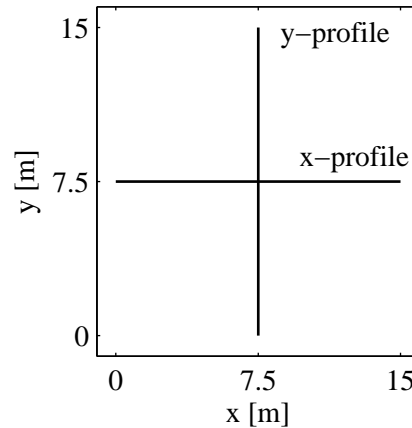


Figure 3.5: Sketch of the two dipole-dipole profiles used to determine soil conductivity.

length using the setup described in section 3.3.1 (see Fig. 3.5). After removing the data with large errors, the correct geometric factors were calculated for the used electrode shape (K_{ell}) and the measured voltages and currents were converted in apparent resistivities ρ_a .

The 2D inversion of the data was performed using a Gauss-Newton algorithm and a fixed regularisation (Günther, 2004). The model was discretised equidistantly with a cell dimension of 0.05 m which corresponds to the maximal resolution (see. section 3.3.1). An accurate error estimate is important for the inversion as the errors define the weighting of the data. Two different sources of error were regarded:

- Statistical measuring errors were determined by analysis of 8 measuring cycles of the square signals and were typically between 0.25% and 4% depending on the configuration factors.
- An error of 1.5 mm was assumed for the positioning of the electrodes as a comb was used. This geometrical error results in a data error of 4% for the smallest dipole separation ($n = 1$) and 2% for the largest separation ($n = 10$).

Table 3.1 describes the adaption of the model to the data. The relative root-

Table 3.1: Adaption of the inverted model to the data when assuming point electrodes and elliptical electrodes.

section	RRMS point elec.	RRMS ell. elec.
<i>x</i> -profile	8.72%	8.26%
<i>y</i> -profile	4.90%	4.83%

mean square deviation is defined:

$$\text{RRMS} = \sqrt{\frac{1}{N} \sum_{i=1}^N \left(\frac{d_i - f_i(M)}{d_i} \right)^2}, \quad (3.20)$$

where d_i are the data, M is the model, $f_i(M)$ the synthetic data and N the number of data. Another parameter describing the fit of the model and weighting the residual by the error ϵ_i of the measurement is χ^2 which will be used in chapter 5:

$$\chi^2 = \frac{1}{N} \sum_{i=1}^N \left(\frac{d_i - f_i(M)}{\epsilon_i} \right)^2. \quad (3.21)$$

If $\chi^2 = 1$, the data are fitted within their errors.

Note, if assuming point electrodes, the deviation between model and data is higher than if using correct configuration factors.

After the inversion, the resistivities were transformed into conductivities. Fig. 3.6 shows a cutout of the inverted *x*- and *y*-profile. A distinct layering with an interface in approximately 0.3 m depth can be noticed relying to the former plough horizon. The topsoil is enriched with humus and penetrated by roots from the grass whereas the lower soil is almost pure sand with marginal organic content. The *x*-profile shows slightly higher subsoil conductivities than the *y*-profile but nearly similar values at the crossing point $(x, y) = (7.5 \text{ m}/7.5 \text{ m})$.

The *x*-profile shows higher variability in the topsoil than the *y*-profile. This anisotropy in the conductivity distribution may be caused by the former cultivation of the area as it was used as an acre some years ago. The *x*-profile is probably perpendicular to the direction of the cultivation whereas the *y*-profile is parallel to it. The small-scale undulations of the plough horizon in the *x*-profile can either be caused by a true topography of the layer caused by

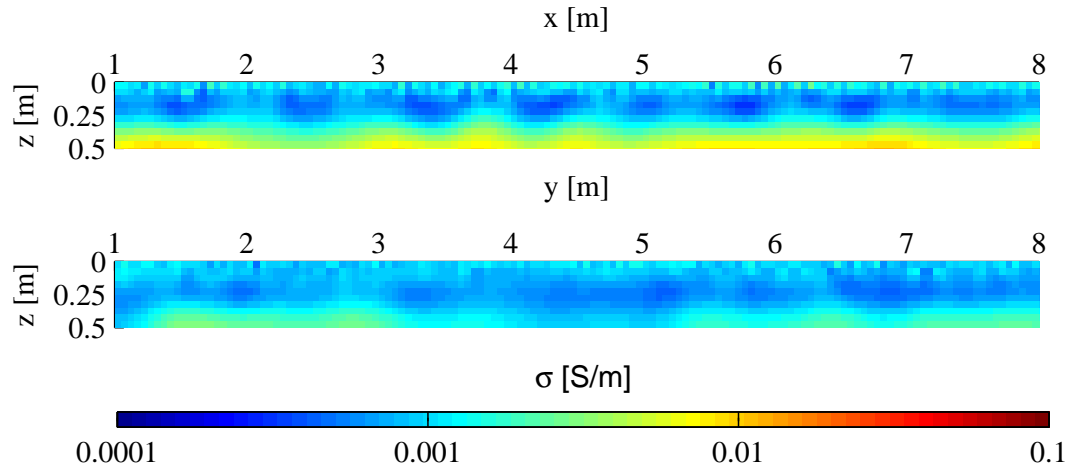


Figure 3.6: Result of the 2D inversion of the dipole-dipole measurements when assuming cylindrical electrodes: x -direction (top), y -direction (bottom). The first part of the 15 m long sections are plotted for better illustration.

the ploughshares or may be an artefact of the inversion, i.e. variabilities in the conductivity of the topsoil may be projected in deeper regions. However, the exact direction of anisotropy cannot be derived from the DC measurements as this would require the presence of measurements in more than two divers directions or at best the presence of 3D measurements on a large area. Such measurements are extremely time consuming so that solely two crossing transects were measured what is feasible in one day.

The geostatistical analysis was applied to the topsoil, i.e. the first 0.25 m of the ground. The first layer beneath the surface (0–0.05 m) is not taken into consideration because it is influenced by the electrodes. Note that the electrode geometry is indeed considered for the correct configuration factors and thus when determining the apparent resistivities and during the forward calculation of the inversion. However, for the FD calculation, currents and voltages are fed and tapped from points on the surface of the model instead from realistically shaped electrodes. Thus, the structure of the ground in the vicinity of the electrodes, i.e. the first layer of the model, cannot be resolved. The area of 0.05–0.25 m is analysed and the distribution function and the variogram in the particular profile direction are determined.

Regarding conductivity the probability density function of both profiles has a positive skewness whereas it is nearly symmetrical when the logarithm is de-

picted (Fig. 3.7). Hence, the conductivity of the topsoil follows approximately a log-normal distribution. The mean conductivity is comparable in both transects whereas the standard deviation is higher in the x -profile data than in the y -profile data.

Figure 3.8 shows the variograms in x - and y -direction. As the variability is higher for the x -profile, the according variogram shows a higher sill. An exponential model is fitted to both experimental variograms yielding a correlation length of $a_x = 0.35$ m and $a_y = 0.5$ m. The left variogram shows some hints of a hole effect¹ caused by the periodic structure in the conductivity distribution along the x -transect which may be caused by former cultivation. However, using models which include a hole effect did not result in a better fit and an exponential model is used as it showed to be the simplest model which describes the data.

¹A hole effect is caused by a periodic data distribution and yields a semivariance which oscillates periodically around the sill whereas the amplitudes of the oscillation decrease with increasing lag distance.

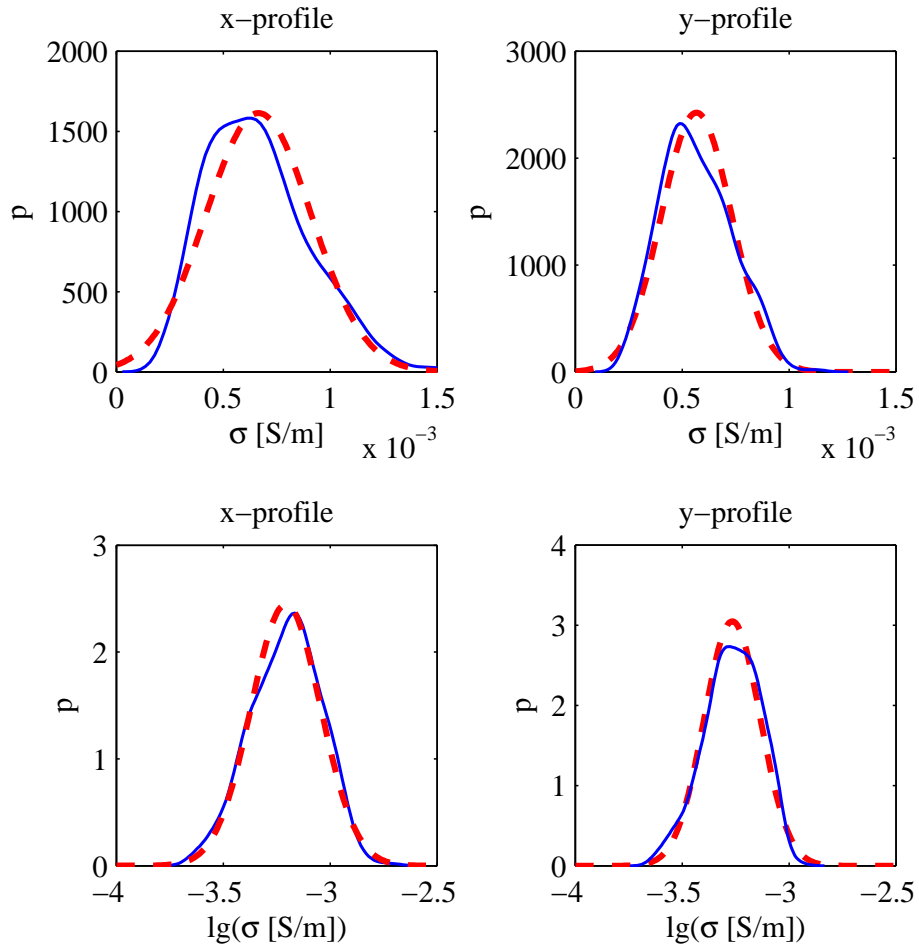


Figure 3.7: Statistical analysis of conductivity at location 1. Experimental probability density function (blue solid) and normal distribution (red dashed) with the same mean and standard deviation as in situ for comparison. The conductivity and the logarithm of conductivity is depicted. The mean and standard deviation are:

Left side, x -profile: $\sigma = 6.6 \cdot 10^{-4} \pm 2.5 \cdot 10^{-4}$ S/m, $\lg(\sigma/(S/m)) = -3.2 \pm 0.16$.

Right side, y -profile: $\sigma = 5.7 \cdot 10^{-4} \pm 1.6 \cdot 10^{-4}$ S/m, $\lg(\sigma/(S/m)) = -3.3 \pm 0.13$.

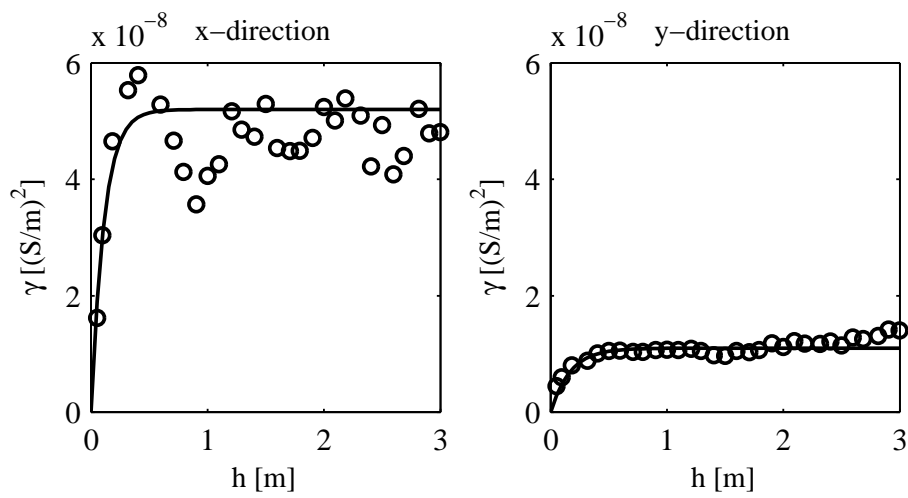


Figure 3.8: Experimental variograms of conductivity distribution at location 1. The semivariance is calculated along the x - and y -profile. The range of the fitted exponential variogram model is $a_x = 0.35$ m and $a_y = 0.5$ m.

4 Dielectric Permittivity ϵ

4.1 Dielectric Properties of Soils

Soil can be regarded as a 3-phase-medium comprising the soil matrix and the pore space which is filled with air and water. The pore water can furthermore be splitted into free and bound water since they electrically behave differently what results in a 4-phase-medium as schematically depicted in Fig. 4.1.

As can be seen from the permittivity values of Fig. 4.1, the dielectric properties of soil are mainly determined by its water content as water has an extraordinary high permittivity compared to the other components.

4.1.1 Mechanisms of Polarisation

If a non-conducting material is exposed to an electric field, the material is polarised. An inner electrical field is induced which is opposed to the outer field yielding a weakened resulting field inside the material. There are four basic polarisation mechanisms which describe the dielectric characteristics of

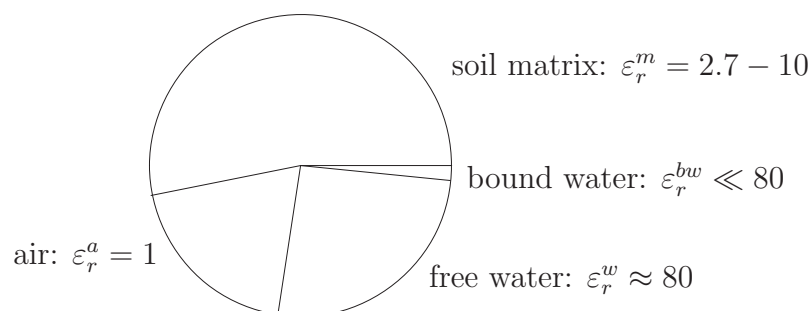


Figure 4.1: Schematic illustration of the soil as a 4-phase-medium. The components soil matrix, air and water (free and bound) are depicted as well as their relative dielectric permittivities ϵ_r (real parts).

a medium depending on the frequency of the outer field.

- **Electronic polarisation:** The electron sheath is displaced relative to the atomic nucleus. This polarisation is always present in any material and mostly superposed by the other polarisation mechanisms. It is the only mechanism occurring at very high frequencies and it determines the optical index of refraction.
- **Ionic polarisation:** The ions of reverse polarity inside a crystal lattice are slightly displaced. This polarisation mechanism describes the dielectric properties of the mineral compounds of soil matrix in the frequency range of GPR.
- **Orientation polarisation:** Usually, the natural dipoles of polar liquids are randomly oriented due to thermal molecular motion. These dipoles are aligned in an outer field. This effect describes the dielectric properties of water in the frequency range of GPR.
- **Interface polarisation:** Interfaces within a composite of different materials may be charged. The displacement of these charges in an outer field results in a polarisation of the medium. This effect determines the behaviour at low frequencies and can be determined e.g. with spectral induced polarisation measurements (SIP).

4.1.2 Dielectric Properties of Water

Liquid water has an extremely high dielectric permittivity $\epsilon_r \approx 80$ compared to most other materials. This is due to the dipole character of the water molecule and its affinity to build clusters (Gerhartz, 1996). The behaviour of liquid water is significantly determined by the orientation polarisation. The dipole molecule is oriented in an electric field by a torsional moment. The thermal movement counteracts the orienting movement of the molecules. Thus, the ratio between orienting electrostatic and disorienting thermal energy describes the alignment of the dipole molecules. For relatively weak electrical fields \vec{E} , as is the case in common GPR applications, the polarisation density \vec{P} is determined by (Demtröder, 1995)

$$\vec{P} = \frac{\varrho_N p^2}{3 k_B T} \vec{E}, \quad (4.1)$$

where ϱ_N is the number of molecules per volume, p its dipole moment, k_B Boltzmann's constant and T the temperature. The relative dielectric permit-

tivity ε_r and the polarisation density are linked by the following relation

$$\vec{P} = \varepsilon_0 (\varepsilon_r - 1) \vec{E}. \quad (4.2)$$

In an ideal dielectric medium the displacement current has a phase lead of 90° with respect to the electric field. With increasing frequency, the dipole cannot follow the alternating electric field and there is a phase shift yielding dielectric losses. Debye (1929) described this phenomenon by a complex frequency dependent permittivity where the imaginary part describes the losses:

$$\varepsilon_r(\omega) = \varepsilon_r'(\omega) - i\varepsilon_r''(\omega). \quad (4.3)$$

The relative permittivity of pure water ε_r^w can be described by a Debye relaxation (Kaatze, 1989):

$$\varepsilon_r^w(\omega, T) = \varepsilon_r^w(\infty, T) + \frac{\varepsilon_r^w(0, T) - \varepsilon_r^w(\infty, T)}{1 + i\omega\tau^w(T)}, \quad (4.4)$$

where $\varepsilon_r^w(\infty, T)$ is the high frequency permittivity, $\varepsilon_r^w(0, T)$ the static permittivity, $\tau^w(T)$ the relaxation time of the water molecule and T the temperature. The temperature dependence of the three parameters can be described by the following empirical functions (Kaatze, 1989).

$$\varepsilon_r^w(0, T) = 10^{1,94404 - 1,991 \cdot 10^{-3} K^{-1} (T - 273.15 \text{ K})} \quad (4.5)$$

$$\varepsilon_r^w(\infty, T) = 5,77 - 2,74 \cdot 10^{-2} K^{-1} (T - 273.15 \text{ K}) \quad (4.6)$$

$$\tau^w(T) = 3,745 \cdot 10^{-15} s \left(1 + 7 \cdot 10^{-5} K^{-2} (T - 300.65 \text{ K})^2\right) e^{\frac{2295,7 \text{ K}}{T}} \quad (4.7)$$

In case of saline water, conduction current contributes to damping. When regarding high frequencies as is the case for GPR, these losses can be added to the dielectric losses and an effective permittivity $\varepsilon_{eff} = \varepsilon_{eff}' - i\varepsilon_{eff}''$ is defined (see section 4.2.2). Equation (4.4) is expanded by a term which only influences the imaginary part and describes the losses due to conduction.

$$\varepsilon_{eff}^w(\omega, T) = \varepsilon_r^w(\infty, T) + \frac{\varepsilon_r^w(0, T) - \varepsilon_r^w(\infty, T)}{1 + i\omega\tau^w(T)} - i \frac{\sigma^w(\omega)}{\varepsilon_0 \omega} \quad (4.8)$$

The real and imaginary part of the relative permittivity of pure water depending on frequency is plotted in Fig. 4.2. The imaginary part and thus the dielectric losses are maximal at the relaxation frequency $\nu_0 = 1/(2\pi\tau^w)$ which is approximately 17 GHz at 293.15 K (20 °C). The curve for water with a conductivity of $\sigma^w = 0.05 \text{ S/m}$ which is a typical value for ground water and

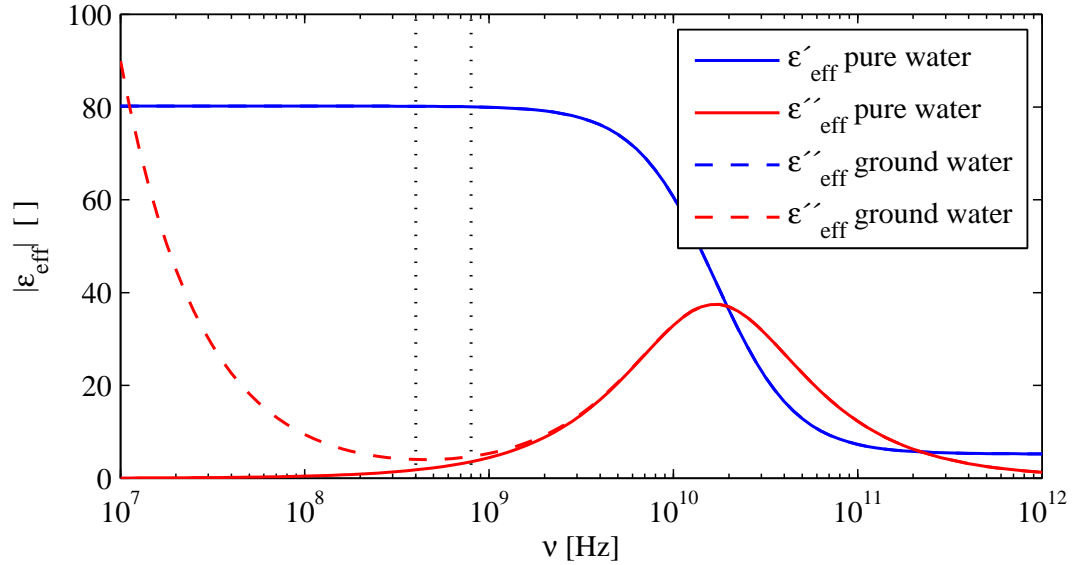


Figure 4.2: Frequency dependent effective complex permittivity ε_{eff} of water at 20 °C. The solid line is for pure water, the dashed line for typical ground water with $\sigma = 0.05$ S/m, whereas the real parts of both coincide. The dotted black lines display the approximate frequency range used later on for the GPR investigations (centre frequencies of the antennas).

corresponds to the tap water used for the experiment in section 3.2.1 is depicted, too. One can note that the lower the frequency the more conductivity will determine the imaginary part of the effective permittivity. In the range of common GPR applications (20 MHz – 1.5 GHz), the imaginary part of the effective permittivity of moist soils has a minimum and wave propagation is possible.

For water with higher salinity, Eq. (4.5) and (4.7) do not hold true any more. The static permittivity is decreasing with increasing salinity due to the hydrate sheath of the ions. The relaxation time also is influenced by the solved ions when the high frequency permittivity seems to be constant (Ulaby et al., 1986). Empirically derived expressions describing the parameters of Eq. (4.8) for water with salinity between 4‰ and 35‰ can be found in Ulaby et al. (1986).

A part of the water in a porous medium is electrically bound¹ water which is

¹This electrically bound water has not to be confounded with bound water in terms of soil sciences or hydrogeology where bound water is the adsorbed water and defined as water

hindered in its orienting movement in an alternating electric field due to interactions of the dipole molecules with the surface of the matrix. The larger the specific surface of the porous material the more the dielectric properties of pore water will be influenced by these interactions. The real part of permittivity is reduced and additional loss effects occur and contribute to the imaginary part (Hübner, 1999). According to Dirksen and Dasberg (1993), the real part of the permittivity of bound water ε_r^{bw} corresponds to the permittivity of ice ($\varepsilon_r^{ice} = 3.15$) whereas Dobson et al. (1985) determine $\varepsilon_r^{bw} \approx 35 - 15i$. The exact definition of bound water and its dielectric properties varies depending on the reference and is an actual research topic. The closer the water molecule is to the soil particle the more the permittivity will correspond to the permittivity of ice. With increasing distance to the soil particle, the dielectric behaviour of the water molecule will match more and more the properties of free water. As only the first few molecule layers close to the mineral grains correspond to electrically bound water (Or and Wraith, 1999), it is only of importance for soils with high specific surface as is the case for clay. The soils where the GPR measurements will be performed have marginal clay content and the effect of bound water is negligible.

4.1.3 Dielectric Properties of Soil Matrix

The dielectric properties of the soil matrix are determined by the ionic and electronic polarisation. In the frequency range of GPR, the permittivity can be regarded as frequency independent. An exception are minerals with high conductivity as is the case for ores or graphite featuring a frequency dependent imaginary part due to the term $\sigma/\omega\varepsilon_0$ which will not be considered in the following. Depending on their mineralogical composition, the permittivity ε_r^m of the soil matrix ranges between 2.7 and 10 (Ulaby et al., 1986). Therefore, dry soils which are composed of mineral grains and air typically feature resulting permittivities between 2 and 4.

4.1.4 Mixing Models

Up to now, the dielectric properties of the individual components of soils have been discussed. We now have to address the issue of how a compound of the soil

which is retained in the soil against gravitational forces. Electrically bound water is only a small part of the adsorbed water.

components matrix, air and water will react on an outer electric field. There exist numerous mixing models describing the permittivity of soils depending on the volumetric fraction V_i of the single components with permittivity ε_i .

Structure-independent models

A general model is the exponential approach (Hübner, 1999):

$$\varepsilon_{res}^\alpha = \sum_i V_i \varepsilon_i^\alpha . \quad (4.9)$$

The exponent α accounts for the geometrical arrangement of the components of the mixture and is confined by the Wiener bounds $-1 < \alpha < 1$ (Moysey and Knight, 2004). If the components are arranged as a serial connection, the resulting permittivity is the harmonic mean of the individual permittivities and $\alpha = -1$. In case the components are arranged as a parallel connection, the resulting permittivity is the arithmetic mean and $\alpha = 1$.

If an electromagnetic wave is considered propagating through a serial connection of layers of the different components, this results in $\alpha = 1/2$:

$$\sqrt{\varepsilon_{res}} = \sum_i V_i \sqrt{\varepsilon_i} , \quad (4.10)$$

which is known as the complex refractive index model (CRIM) (Shen et al., 1985) or occasionally as Birchak formula (Birchak et al., 1974; Hübner, 1999; Roth et al., 1990). The arrangement of the single composites of the soil in parallel homogeneous layers is only a theoretical representation. The three phases matrix, air and water are rather irregularly distributed in natural soils. Hübner (1999) analysed the permittivity of randomly distributed synthetic media by calculating the electric field distribution. He determined the exponent α to be in good agreement with the CRIM formula. An exponent close to $\alpha = 0.5$ is also determined by Roth et al. (1990) for experimental data.

Dobson et al. (1985) analysed five different soils and determined an exponent $\alpha = 0.65$. The discrepancy might be caused by the higher frequencies ($\nu > 1.4$ GHz) they used for their analysis compared to other authors.

Structure-dependent models

These model functions determine the permittivity of a mixture taking into account the geometric shape of the components and therefore giving consideration to the physical effects. Some models are given in Sihvola and Kong (1988), DeLoor (1964) or Shen et al. (1985). But the basic problem is that the geometric shape of the constituents is usually not known and assumptions have

to be made. This is the reason why these model functions are used for petrophysical interpretations of laboratory measurements. However they are rarely used for field applications and structure-independent or empirical functions are preferred.

Site specific calibration functions

It is best to analyse a soil sample at different water contents. Unfortunately, the determination of the permittivity of a soil sample in the laboratory with methods described in the following section needs much time and is not trivial. An empirical function is adopted to the measurements which relates soil permittivity to its water content or vice versa. It has to be considered that a soil sample will not always be representative for a whole area especially when soil variability is high. But this holds true for all mixing models which in a strict sense can only be applied at a specific point of a location.

Empirical functions

A pragmatic alternative which is often applied are empirical functions determined on a variety of representative soils. The most frequently used functions relating soil permittivity to water content and vice versa were deduced by Topp et al. (1980) by fitting a polynomial function to the permittivity of four mineral soils derived at different volumetric water contents Θ_V :

$$\varepsilon_r = 3.03 + 9.3 \Theta_V + 146.0 \Theta_V^2 - 76.7 \Theta_V^3 \quad (4.11)$$

$$\Theta_V = -5.3 \cdot 10^{-2} + 2.92 \cdot 10^{-2} \varepsilon_r - 5.5 \cdot 10^{-4} \varepsilon_r^2 + 4.3 \cdot 10^{-6} \varepsilon_r^3. \quad (4.12)$$

4.1.5 Determining the Dielectric Permittivity of Porous Media

The dielectric permittivity can either be determined with the GPR which uses free electromagnetic waves or by other electromagnetic methods by utilising guided waves. The methods applying GPR will be developed in the next sections. Regarding the second method, one can in principle distinguish two techniques: one operates in frequency domain and the other in time domain. In both cases, the material under test is the media which is penetrated by the electric field of the applied signal. This might be in between Lecher wires, the inner and outer conductor of a coaxial transmission line or inside a hollow waveguide.

In frequency domain, the amplitude and phase of the signal can be determined either in transmission and/or in reflection mode. The complex permittivity

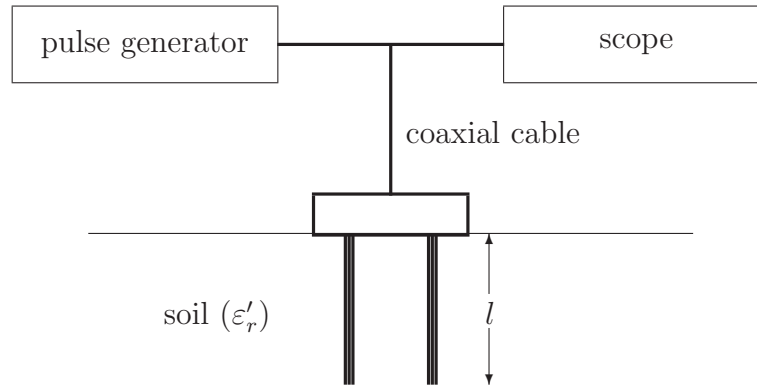


Figure 4.3: Schematic diagram of TDR principle: an electromagnetic pulse is fed on the probe of length l inserted in the soil and is reflected at its end. The traveltime t is recorded with a scope.

can be derived from the amplitude and phase of the transmitted or reflected signal depending on the frequency of the applied electric field (Hübner, 1999).

In time domain, the propagation time of an electromagnetic pulse is determined. The signal propagates along a waveguide of diverse form whereby the soil is the dielectric medium, e.g. the material between the inner and outer conductor of a coaxial transmission line. This material determines the propagation velocity of the pulse. In time-domain reflectometry (TDR), the pulse is reflected at the open end of the waveguide and the travel time of this reflection is determined (Fig. 4.3) (Hübner, 1999; Stacheder, 1996; Topp et al., 1982). As the travel path is known as twice the length l of the transmission line, the transformation of the travel time t in propagation velocity v and finally in real parts of the relative permittivity ϵ'_r is trivial:

$$v = \frac{2l}{t} \quad (4.13)$$

$$\epsilon'_r = \frac{c_0^2}{v^2}. \quad (4.14)$$

Most TDR probes used in field consist of two or three parallel rods which are pushed in the soil representing unsymmetrical and symmetrical waveguides, respectively. The electromagnetic energy is mainly restricted to the space between the rods which corresponds to the approximate sampling volume.

4.2 Theory of Electromagnetic Wave Propagation

In this section, the main principles of electromagnetic wave propagation are described starting with Maxwell's equations and, unlike commonly used simplifications, including all three electromagnetic parameters: magnetic permeability, electric conductivity and permittivity. This allows for assessing the inaccuracy of practical applications if these simplifications are used. E.g. magnetic permeability is usually set to $\mu_r = 1$ or electric conductivity is often neglected. However, this may not be practicable for all soils.

4.2.1 Fundamental Equations of Electrodynamics

The following equations form the fundamentals of the theory of electromagnetic wave propagation. The four Maxwell's equations in differential form are:

$$\vec{\nabla} \cdot \vec{D}(\vec{r}, t) = \rho_{el}(\vec{r}) \quad (4.15)$$

$$\vec{\nabla} \cdot \vec{B}(\vec{r}, t) = 0 \quad (4.16)$$

$$\vec{\nabla} \times \vec{E}(\vec{r}, t) = -\frac{\partial \vec{B}(\vec{r}, t)}{\partial t} \quad (4.17)$$

$$\vec{\nabla} \times \vec{H}(\vec{r}, t) = \vec{j}(\vec{r}, t) + \frac{\partial \vec{D}(\vec{r}, t)}{\partial t}, \quad (4.18)$$

where \vec{E} and \vec{H} are the electric and magnetic field strength, \vec{D} and \vec{B} the electric and magnetic flux density, \vec{j} the free current density and ρ_{el} the free electric charge density. The assumption of relatively weak field strength, as is the case for GPR applications, results in a linear dependency between cause and effect. In this case, the field vectors and currents are linked by the following constitutive equations in frequency domain ²:

$$\vec{D}(\vec{r}, \omega) = \varepsilon_0 \varepsilon_r(\vec{r}, \omega) \vec{E}(\vec{r}, \omega) \quad (4.19)$$

$$\vec{B}(\vec{r}, \omega) = \mu_0 \mu_r(\vec{r}, \omega) \vec{H}(\vec{r}, \omega) \quad (4.20)$$

$$\vec{j}(\vec{r}, \omega) = \sigma(\vec{r}, \omega) \vec{E}(\vec{r}, \omega). \quad (4.21)$$

²The position of \vec{B} and \vec{H} is not the logical, as \vec{E} and \vec{B} are the basic fields which cause a force on a charged particle and a magnetic particle or moving charged particle, respectively. Thus, \vec{B} should be named magnetic field strength instead of \vec{H} . However, the definition and the asymmetry in Maxwell's equations has historical reasons (Sommerfeld, 1967; Fließbach, 2005).

Here, ε_0 and μ_0 are the electric and magnetic field constant, ε_r the relative dielectric permittivity, μ_r the relative magnetic permeability and σ the electric conductivity. The media are considered to be isotropic. In case of anisotropy, the material parameters are no scalar values any more, but tensors. Note that Maxwell's equations are defined in time domain but the constitutive equations are written in frequency domain. Only if the media are non dispersive, i.e. if the parameters ε , μ and σ do not depend on frequency, they hold true in time domain in the same form. Otherwise, the multiplication in frequency domain has to be substituted by a convolution in time domain:

$$\vec{D}(\vec{r}, t) = \varepsilon_0 \varepsilon_r(\vec{r}, t) * \vec{E}(\vec{r}, t) \quad (4.22)$$

$$\vec{B}(\vec{r}, t) = \mu_0 \mu_r(\vec{r}, t) * \vec{H}(\vec{r}, t) \quad (4.23)$$

$$\vec{j}(\vec{r}, t) = \sigma(\vec{r}, t) * \vec{E}(\vec{r}, t). \quad (4.24)$$

We are concerned with a linear, time invariant and causal system with \vec{E} and \vec{H} being the cause and \vec{D} , \vec{B} and \vec{j} being the effect. The functions $\varepsilon_r(\omega)$, $\mu_r(\omega)$ and $\sigma(\omega)$ are the system functions, i.e. the Fourier transforms of the impulse responses $\varepsilon_r(t)$, $\mu_r(t)$ and $\sigma(t)$ of the system. Thus, Eq. 4.22 can be written as (Papoulis, 1962)

$$\begin{aligned} \vec{D}(\vec{r}, t) &= \varepsilon_0 \int_{-\infty}^t \varepsilon_r(\vec{r}, t - \tau) \vec{E}(\vec{r}, \tau) d\tau \\ &= \varepsilon_0 \int_0^{\infty} \varepsilon_r(\vec{r}, \tau) \vec{E}(\vec{r}, t - \tau) d\tau. \end{aligned} \quad (4.25)$$

From this equation one can see that electric flux density $\vec{D}(t_1)$ does not only depend on the electric field strength $\vec{E}(t_1)$ but also on the field $\vec{E}(t < t_1)$. Equations (4.23)–(4.24) can be formulated in the same way.

Alternatively, Maxwell's equations can be transformed to frequency domain which will permit to apply the constitutive equations in the form of Eq. (4.19)–(4.21). The pair of integrals of the Fourier transformation is defined as follows where $\vec{A}(t)$ and $\vec{A}(\omega)$ is the vector field to be transformed from time to frequency domain:

$$\vec{A}(t) = \frac{1}{2\pi} \int_{-\infty}^{\infty} \vec{A}(\omega) e^{i\omega t} d\omega \quad (4.26)$$

$$\vec{A}(\omega) = \int_{-\infty}^{\infty} \vec{A}(t) e^{-i\omega t} dt. \quad (4.27)$$

One has to assume transient vector fields $\vec{D}(t)$ and $\vec{B}(t)$, i.e. they are vanishing for $t \rightarrow \pm\infty$. Then, Maxwell's equations in frequency domain are:

$$\vec{\nabla} \cdot \vec{D}(\vec{r}, \omega) = \delta(\omega) \varrho_{el}(\vec{r}) \quad (4.28)$$

$$\vec{\nabla} \cdot \vec{B}(\vec{r}, \omega) = 0 \quad (4.29)$$

$$\vec{\nabla} \times \vec{E}(\vec{r}, \omega) = -i\omega \vec{B}(\vec{r}, \omega) \quad (4.30)$$

$$\vec{\nabla} \times \vec{H}(\vec{r}, \omega) = \vec{j}(\vec{r}, \omega) + i\omega \vec{D}(\vec{r}, \omega), \quad (4.31)$$

with $\delta(\omega)$ being Dirac's delta function.

4.2.2 Dispersion Relation

In the following, some additional assumptions have to be made:

- The regarded region is solenoidal, i.e. free of electric charge.
- The region is homogeneous, i.e. ε , μ and σ do not depend on the specific location \vec{r} .³

Then, Eq. (4.28) and (4.19) leads to

$$\vec{\nabla} \cdot (\varepsilon_0 \varepsilon_r(\omega) \vec{E}(\vec{r}, \omega)) = 0. \quad (4.32)$$

Using the relation $\vec{\nabla} \cdot (a\vec{A}) = a(\vec{\nabla} \cdot \vec{A}) + (\vec{\nabla} a) \cdot \vec{A}$ and assuming a homogeneous medium, Eq. (4.32) results in:

$$\vec{\nabla} \cdot \vec{E}(\vec{r}, \omega) = 0. \quad (4.33)$$

By applying the curl to Eq. (4.30) and using the identity $\vec{\nabla} \times \vec{\nabla} \times \vec{A} = \vec{\nabla}(\vec{\nabla} \cdot \vec{A}) - \vec{\nabla} \cdot (\vec{\nabla} \vec{A})$ (Bronstein and Semendjajew, 1991) and constituting Eq. (4.33), this leads to:

$$\vec{\nabla} \cdot \vec{\nabla} \vec{E}(\vec{r}, \omega) = i\omega \vec{\nabla} \times \vec{B}(\vec{r}, \omega). \quad (4.34)$$

$\vec{B}(\vec{r}, \omega)$ can be expressed by the constitutive equation (4.20). When using the relation $\vec{\nabla} \times (a\vec{A}) = a(\vec{\nabla} \times \vec{A}) + (\vec{\nabla} a) \times \vec{A}$ and assuming the constance of μ_r inside the regarded area, Eq. (4.34) results in:

$$\Delta \vec{E}(\vec{r}, \omega) = i\omega \mu_0 \mu_r(\omega) \vec{\nabla} \times \vec{H}(\vec{r}, \omega), \quad (4.35)$$

³This assumption will be abandoned later on when reflection and diffraction of waves at an interface will be discussed

where Δ is the Laplace operator. $\vec{H}(\vec{r}, \omega)$ can be expressed by Maxwell's equation (4.31). Using Ohm's law (Eq. (4.21)), the above equation finally yields:

$$\Delta \vec{E}(\vec{r}, \omega) = -\omega^2 \mu_0 \mu_r(\omega) \varepsilon_0 \left(\varepsilon_r(\omega) - i \frac{\sigma(\omega)}{\varepsilon_0 \omega} \right) \vec{E}(\vec{r}, \omega). \quad (4.36)$$

Generally, the material parameters are complex values, where the imaginary parts of the dielectric permittivity and magnetic permeability describe loss effects. In the following, the complex conductivity and relative permittivity and permeability are defined as:

$$\sigma(\omega) = \sigma'(\omega) - i\sigma''(\omega) \quad (4.37)$$

$$\varepsilon_r(\omega) = \varepsilon_r'(\omega) - i\varepsilon_r''(\omega) \quad (4.38)$$

$$\mu_r(\omega) = \mu_r'(\omega) - i\mu_r''(\omega), \quad (4.39)$$

where the negative definition of the imaginary parts in Eq. (4.37)–(4.39) is of no physical significance but historical and has only practical reasons for plotting. The dielectric loss effects are caused when the alignment of the electric dipoles in an alternating electrical field is retarded by the thermal Brownian movement of the dipole molecules. The process can be characterised by a Debye relaxation (Debye, 1929), Eq. 4.4. In case of magnetic losses, the process is principally the same but the dipole molecules have to be replaced by magnetic moments aligned in an alternating magnetic field. In the frequency range of GPR, displacement currents are usually higher than conduction currents. When conduction increases, more and more diffusion will occur and the waves will be damped as is the case for clayey or salty humid soils. In media where GPR works satisfactorily and displacement exceeds conduction, one can define an effective relative permittivity

$$\varepsilon_{eff}(\omega) = \varepsilon'_{eff}(\omega) - i\varepsilon''_{eff}(\omega) = \varepsilon_r'(\omega) - i \left(\varepsilon_r''(\omega) + \frac{\sigma(\omega)}{\varepsilon_0 \omega} \right). \quad (4.40)$$

The real part of the conductivity acts as an additional loss process to the losses due to dielectric relaxation. According to Du (1996), the imaginary part of the complex conductivity can be neglected for conductivities < 1 S/m. In soils where conductivity is mainly determined by ionic transport in the pore fluid, the frequency dependence of conductivity is negligible. In materials with high specific surface compared to their porosity, for example salt rock or soils with high clay content, surface conductivity may exceed ionic conductivity and the frequency dependence is not negligible any more. But these soils are usually characterised by high absolute conductivity values and no wave propagation

will occur. Thus, in Eq. (4.40), $\sigma(\omega)$ can be replaced by the real electric DC conductivity σ , when restricting to media where GPR works properly.

The differential equation (4.36) can be solved using a plane-wave ansatz

$$\vec{E}(\vec{r}, \omega) = \vec{E}_0 e^{i(\vec{k} \cdot \vec{r} - \omega t)}, \quad (4.41)$$

and the solution is the dispersion relation

$$k^2(\omega) = \omega^2 \mu_0 \varepsilon_0 \mu_r(\omega) \varepsilon_{eff}(\omega). \quad (4.42)$$

In lossy media the wavenumber k is a complex value, $k = \beta(\omega) + i\alpha(\omega)$, where α is the attenuation constant and β the phase constant. From Eq. (4.42) follows:

$$\beta = \frac{\omega}{c_0} \sqrt{\frac{\mu_r(\omega) \varepsilon'_{eff}(\omega)}{2} \left(\sqrt{1 + \tan^2 \delta} + 1 \right)} \quad (4.43)$$

$$\alpha = \frac{\omega}{c_0} \sqrt{\frac{\mu_r(\omega) \varepsilon'_{eff}(\omega)}{2} \left(\sqrt{1 + \tan^2 \delta} - 1 \right)} \quad (4.44)$$

$$\text{with } \tan \delta = \frac{\varepsilon''_{eff}}{\varepsilon'_{eff}}$$

$$\text{and } c_0 = \frac{1}{\sqrt{\varepsilon_0 \mu_0}}.$$

The loss tangent $\tan \delta$ is the ratio of conduction current and displacement current. In low-loss media where $\varepsilon''_{eff} \ll \varepsilon'_{eff}$ and where wave propagation will occur, $\tan \delta$ approaches zero. Then, the phase velocity of electromagnetic waves can be expressed by:

$$v_{ph} = \frac{\omega}{\beta} \quad (4.45)$$

$$= \frac{c_0}{\sqrt{\frac{1}{2} \mu_r(\omega) \varepsilon'_{eff}(\omega) \left(\sqrt{1 + \tan^2 \delta} + 1 \right)}} \quad (4.46)$$

$$\approx \frac{c_0}{\sqrt{\mu_r(\omega) \varepsilon'_r(\omega)}}. \quad (4.47)$$

Olhoeft (1998) mentions significant magnetic relaxation losses in iron bearing sands, but states that most naturally occurring magnetic minerals have never been measured at radar frequencies. As even soils with very high content of

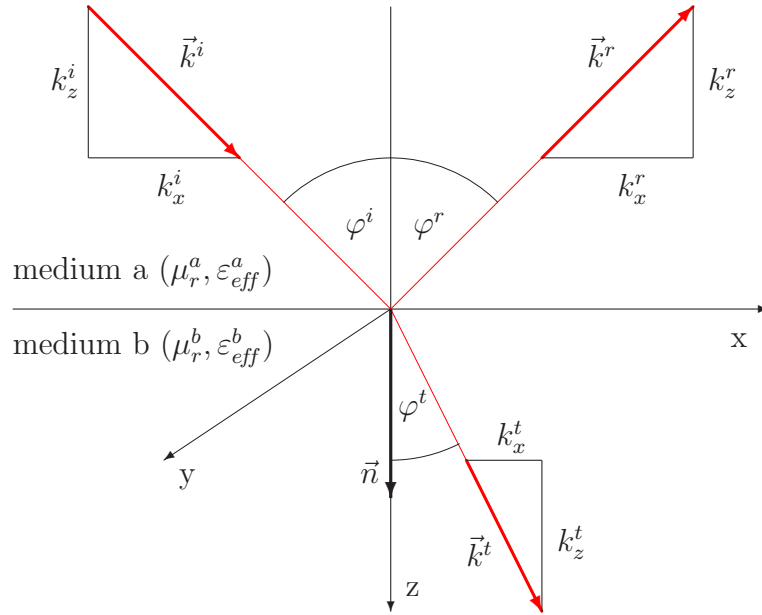


Figure 4.4: Reflection and transmission of an electromagnetic plane wave at a planar interface.

ferrimagnetic minerals like e.g. ferralsols (FAO, 2006) formed from basalt have typically values of $\mu'_r \leq 1.1$ (own measurements), the dielectric properties will predominantly characterise the soils at high frequencies. Thus, the relative magnetic permeability can be set to the value of 1 as is usually done when regarding radar frequencies. The phase velocity of electromagnetic waves simplifies to the well-known relation for non-magnetic media with negligible losses:

$$v_{ph} \approx \frac{c_0}{\sqrt{\varepsilon'(\omega)}}. \quad (4.48)$$

4.2.3 Reflection of Electromagnetic Waves

Up to now, the media were considered to be homogeneous, i.e. the three material parameters were considered to be constant in space. Let us now deal with what will happen if a plane wave (Eq. (4.41)) reaches an interface. A part of the incident energy will be reflected, the other part will be transmitted and refracted to the lower medium. A coordinate system is chosen as depicted in Fig. 4.4. The interface between the two media is the x - y -plane and the x - z -plane defines the incident wave k-vector, \vec{k}^i . From Maxwell's equations one

can deduce the following boundary conditions: The tangential component of \vec{E} and \vec{H} and the normal component of \vec{D} and \vec{B} are continuous at the interface (see e.g. Jackson (1999)). As the fields have to be temporally and spatially continuous, the phase factors of the incident, reflected, and transmitted wave have to be equal:

$$\left(\vec{k}^i \cdot \vec{r} - \omega_i t\right) \Big|_{z=0} = \left(\vec{k}^r \cdot \vec{r} - \omega_r t\right) \Big|_{z=0} = \left(\vec{k}^t \cdot \vec{r} - \omega_t t\right) \Big|_{z=0} \quad \forall t, \vec{r}. \quad (4.49)$$

As Eq. (4.49) has to hold true for all times t , the frequencies of the three waves are identical:

$$\omega_i = \omega_r = \omega_t. \quad (4.50)$$

Besides the temporal changes, the spatial changes of the phase factor have to be equal along the interface. As $r_z = 0$ on the interface and with the incident wave lying in the x - z -plane ($k_y^i = 0$), the following can be deduced:

$$0 = k_y^r = k_y^t \quad (4.51)$$

$$k_x^i = k_x^r = k_x^t. \quad (4.52)$$

Eq. (4.51) means that the incident, reflected, and transmitted waves lie in the same plane. From Eq. (4.52) and Fig. 4.4 follows:

$$\sin \varphi^i k^i = \sin \varphi^r k^r = \sin \varphi^t k^t, \quad (4.53)$$

which is Snell's law, when expressing k by Eq. (4.42):

$$\frac{\sin \varphi^i}{\sin \varphi^t} = \frac{k^t}{k^i} = \sqrt{\frac{\mu_r^b \varepsilon_{eff}^b}{\mu_r^a \varepsilon_{eff}^a}} \quad (4.54)$$

$$\varphi^r = \varphi^i. \quad (4.55)$$

The material parameters usually depend on frequency and are complex values. Thus, k and φ generally are complex.

After having deduced the kinematic law of refraction, we deduce the dynamics, i.e. the amplitudes of the reflected and transmitted wave. Substituting the \vec{E} and \vec{B} fields in Maxwell's equation (4.30) by a plane wave ansatz

$$\vec{E} = \vec{E}_0 e^{i(\vec{k}\vec{r} - \omega t)} \quad (4.56)$$

$$\vec{B} = \vec{B}_0 e^{i(\vec{k}\vec{r} - \omega t)}, \quad (4.57)$$

and taking into consideration that the equation has to hold true $\forall (\vec{r}, t)$, the following can be deduced:

$$\omega = \tilde{\omega} \quad (4.58)$$

$$\vec{k} = \tilde{\vec{k}} \quad (4.59)$$

$$\vec{k} \times \vec{E}_0 = -\omega \vec{B}_0. \quad (4.60)$$

The electric and magnetic fields oscillate with the same frequency and propagate in the same direction. \vec{E} and \vec{B} are both perpendicular one to another and perpendicular to \vec{k} . Thus, we are concerned with a transverse electromagnetic wave (TEM). We define a vector \vec{n} normal to the interface (see Fig. 4.4). Then, using Eq. (4.60), the continuity of the fields at the interface can be expressed as:

$$\left(\varepsilon_r^a \vec{E}_0^i + \varepsilon_r^a \vec{E}_0^r - \varepsilon_r^b \vec{E}_0^t \right) \cdot \vec{n} = 0 \quad (\vec{D}_n \text{ cont.}) \quad (4.61)$$

$$\left(\vec{k}^i \times \vec{E}_0^i + \vec{k}^r \times \vec{E}_0^r - \vec{k}^t \times \vec{E}_0^t \right) \cdot \vec{n} = 0 \quad (\vec{B}_n \text{ cont.}) \quad (4.62)$$

$$\left(\vec{E}_0^i + \vec{E}_0^r - \vec{E}_0^t \right) \times \vec{n} = 0 \quad (\vec{E}_t \text{ cont.}) \quad (4.63)$$

$$\left(\frac{1}{\mu^a} \vec{k}^i \times \vec{E}_0^i + \frac{1}{\mu^a} \vec{k}^r \times \vec{E}_0^r - \frac{1}{\mu^b} \vec{k}^t \times \vec{E}_0^t \right) \times \vec{n} = 0 \quad (\vec{H}_t \text{ cont.}) \quad (4.64)$$

When applying the continuity of the fields at the interface, one can consider an incident wave with \vec{E}_0^i either parallel or perpendicular to the plane of incidence: $\vec{E}_{0\parallel}^i$ and $\vec{E}_{0\perp}^i$. Any other polarisation can be expressed by linear combination of both elementary polarisations. Due to the symmetry of the interface to the incident plane, the polarisation cannot be changed when the wave is reflected or transmitted (Fließbach, 2005). Thus, we can treat both elementary directions separately. First, we regard the case of $\vec{E}_{0\perp}^i$, i.e. $\vec{E}_0^i \perp \vec{n}$. From Eq. (4.63) follows:

$$E_0^i + E_0^r - E_0^t = 0. \quad (4.65)$$

When applying some vector algebra to Eq. (4.64) and inserting $k_z = k \cos \varphi$ one can deduce:

$$\frac{1}{\mu^a} (k^i \cos \varphi^i E_0^i - k^r \cos \varphi^r E_0^r) - \frac{1}{\mu^b} k^t \cos \varphi^t E_0^t = 0. \quad (4.66)$$

Substituting Eq. (4.65) and (4.66) and considering that $k^i = k^r = k^a$ and $k^t = k^b$ and expressing φ^t by Snell's law, one can deduce the coefficient of

reflection ρ and transmission τ ⁴, the so-called Fresnel formulas for $\vec{E}_{0\perp}^i$:

$$\rho_{\perp} = \frac{E_0^r}{E_0^i} = \frac{\mu_r^b k^a \cos \varphi^i - \mu_r^a \sqrt{(k^b)^2 - (k^a)^2 \sin^2 \varphi^i}}{\mu_r^b k^a \cos \varphi^i + \mu_r^a \sqrt{(k^b)^2 - (k^a)^2 \sin^2 \varphi^i}} \quad (4.67)$$

$$\tau_{\perp} = \frac{E_0^t}{E_0^i} = \frac{2\mu_r^b k^a \cos \varphi^i}{\mu_r^b k^a \cos \varphi^i + \mu_r^a \sqrt{(k^b)^2 - (k^a)^2 \sin^2 \varphi^i}}. \quad (4.68)$$

In analogy, the equations of continuity can be used to deduce the Fresnel formulas for $\vec{E}_{0\parallel}^i$ (Ward and Hohmann, 1988):

$$\rho_{\parallel} = \frac{E_0^r}{E_0^i} = \frac{\mu_r^b k^a \sqrt{(k^b)^2 - (k^a)^2 \sin^2 \varphi^i} - \mu_r^a (k^b)^2 \cos \varphi^i}{\mu_r^b k^a \sqrt{(k^b)^2 - (k^a)^2 \sin^2 \varphi^i} + \mu_r^a (k^b)^2 \cos \varphi^i} \quad (4.69)$$

$$\tau_{\parallel} = \frac{E_0^t}{E_0^i} = \frac{2\mu_r^b k^a k^b \cos \varphi^i}{\mu_r^a (k^b)^2 \cos \varphi^i + \mu_r^b k^a \sqrt{(k^b)^2 - (k^a)^2 \sin^2 \varphi^i}}. \quad (4.70)$$

The k values are defined by the dispersion relation, Eq. (4.42), when the appropriate parameters of medium a or b are used:

$$k^{a,b} = \omega \sqrt{\mu_0 \mu_r^{a,b} \varepsilon_0 \varepsilon_{eff}^{a,b}}. \quad (4.71)$$

Thus, the coefficient of reflection and transmission depend on the physical parameters of the media on both sides of the interface, the frequency, the angle of incidence, and the polarisation of the incident wave. When assuming normal incidence ($\varphi^i = 0$), which is often the case for GPR applications, the polarisation is of no significance any more and Eq. (4.67)–(4.70) simplify to:

$$\rho = \frac{\mu_r^b \sqrt{\mu_r^a \varepsilon_{eff}^a} - \mu_r^a \sqrt{\mu_r^b \varepsilon_{eff}^b}}{\mu_r^b \sqrt{\mu_r^a \varepsilon_{eff}^a} + \mu_r^a \sqrt{\mu_r^b \varepsilon_{eff}^b}} \quad (4.72)$$

$$\tau = \frac{2\mu_r^b \sqrt{\mu_r^a \varepsilon_{eff}^a}}{\mu_r^b \sqrt{\mu_r^a \varepsilon_{eff}^a} + \mu_r^a \sqrt{\mu_r^b \varepsilon_{eff}^b}}. \quad (4.73)$$

When regarding common soils, μ_r can usually be set to the value of 1. Then, only the contrast in ε_{eff} determines ρ . When a wave propagating in a medium with k^a is reflected at an interface to a medium with $k^b > k^a$ (e.g. $\varepsilon_r^{b'} > \varepsilon_r^{a'}$), the coefficient of reflection gets negative. Thus, the phase shift is π when

⁴Note, the coefficient of reflection and transmission is defined as ratio of field strength and not energy as is sometimes the case.

the wave is reflected at an optically denser material. Generally, the material parameters are complex values and depend on frequency. This also holds for the coefficient of reflection and transmission. In case of complex coefficients, the incident wave will not only be reflected and transmitted but also a phase shift will occur.

Let us now regard two media with negligible losses and $k^a > k^b$. Then, Snell's law yields:

$$\sin \varphi^i = \frac{k^b}{k^a} \sin \varphi^t . \quad (4.74)$$

As the angle of refraction is limited to $\varphi^t \leq 90^\circ$, the refracted wave can maximally propagate parallel to the interface. Therefore, the critical angle of incidence is:

$$\varphi_c^i = \arcsin \frac{k^b}{k^a} . \quad (4.75)$$

When the angle of incidence is getting larger than φ_c^i then $\sin \varphi^t > 1$ which signifies φ^t is complex (Jackson, 1999). The radicand in Eq. (4.67) and (4.69) is negative and thus the square root is purely imaginary, which yields:

$$\rho_\perp = +1, \quad \rho_\parallel = -1 \quad \forall \varphi^i > \varphi_c^i . \quad (4.76)$$

Thus, the whole incident wave is reflected at the interface and the component with an E -field parallel to the plane of incidence suffers a phase change.

4.2.4 Horizontal Resolution – 1st Fresnel Zone

The Huygens' principle is one of the basic principles of wave propagation. Every point of a wave front can be regarded as the origin of a new spherical wave. Thus, when a wave is reflected by a plane interface, every point will emit such an elementary wave. As a simplification, we consider a zero offset measurement, i.e. the wave is emitted and recorded at the same point. We can divide the reflecting interface into different zones in such a way that the reflected energy from every single zone interferes constructively at the antenna. This means that every wave reflected inside each individual Fresnel zone has a maximal travel-path difference (two way) of $\lambda/2$. The first Fresnel zone is a circle followed by concentric circular discs as Fresnel zones of higher order.

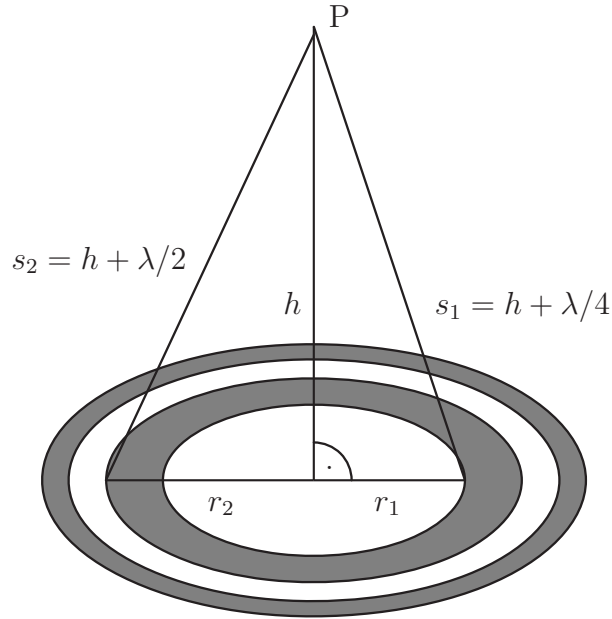


Figure 4.5: First four Fresnel zones of a reflecting interface; the transmitting and receiving antennas are placed at point P.

From Fig. 4.5 follows the radius r_n of the n -th Fresnel zone:

$$h^2 + r_n^2 = s_n^2 = \left(h + n\frac{\lambda}{4}\right)^2 \quad (4.77)$$

$$r_n = \frac{1}{2}\sqrt{2nh\lambda + \frac{n^2\lambda^2}{4}}, \quad (4.78)$$

where h is the height of the antenna to the interface and λ is the dominant wavelength. If $h \gg \lambda$, adjacent Fresnel zones have approximately the same surface. Thus, they will all provide the same contribution, if spherical divergence due to different wave paths is neglected. As adjacent zones interfere destructively, the total amplitude at the point of observation P is:

$$\begin{aligned} E(P) &= \sum_{n=1}^N E_n \\ &= |E_1| - |E_2| + |E_3| - |E_4| + \dots \pm |E_N| \end{aligned} \quad (4.79)$$

$$\text{with } E_n = \frac{E_0}{2s_n}, \quad (4.80)$$

where E_0 is the emitted field strength, E_n the contribution of the n -th Fresnel zone to the field strength at point P and s_n the single travel path of the wave.

A mathematical series like (4.79) can be written as (Demtröder, 1995):

$$E(P) = \frac{1}{2}|E_1| + \left(\frac{1}{2}|E_1| - |E_2| + \frac{1}{2}|E_3| \right) + \left(\frac{1}{2}|E_3| - |E_4| + \frac{1}{2}|E_5| \right) + \dots + \frac{1}{2}|E_N|. \quad (4.81)$$

If $h \gg \lambda$, s_n will not change much from the n -th to the $(n+1)$ -th zone. Then E_n can be approximated to:

$$|E_n| \approx \frac{1}{2} (|E_{n-1}| + |E_{n+1}|). \quad (4.82)$$

When substituting Eq. (4.82) into (4.81), all terms of the series cancel except for the first and the last term:

$$E(P) = \frac{1}{2}|E_1| + \frac{1}{2}|E_N|. \quad (4.83)$$

As the last term is negligible, only the first fresnel zone contributes to the amplitude at the point of observation. The maximal horizontal resolution of GPR is determined by the diameter $d = 2r_1$ of the first Fresnel zone:

$$r_1 = \frac{1}{2} \sqrt{2h\lambda + \frac{\lambda^2}{4}}. \quad (4.84)$$

Objects which are separated by less than d cannot be distinguished. When a wave is reflected at a widespread plane interface, the recorded signal does not originate from a point but from the area of the first Fresnel zone. Thus, the physical properties of this zone will determine the reflected amplitude.

In a strict sense, the deductions above only hold true if the distance of the antenna to the reflecting interface is large compared to the wavelength. This assumption is violated by most GPR applications, but the deduced relations are frequently used as approximations. The often used pulse radar systems do not emit a single frequency but a frequency spectrum of some octaves. As the radius of the Fresnel zone depends on frequency, one will usually define the Fresnel zones for the centre frequency of the emitted radar pulse.

4.2.5 Homogeneous and Inhomogeneous Waves – the Groundwave of GPR

So far, we have considered homogeneous plane waves, i.e. k was real in media with negligible losses. Inhomogeneous waves have a complex wavenumber

vector $\vec{k} = \vec{k}' + i\vec{k}''$. A plane inhomogeneous wave thus has the form:

$$\vec{E} = \vec{E}_0 \underbrace{e^{i(\vec{k}' \cdot \vec{r} - \omega t)}}_{e^{i\phi}} \underbrace{e^{-\vec{k}'' \cdot \vec{r}}}_A. \quad (4.85)$$

The planes with constant phase $\Phi = c_1$ and constant amplitude $A = c_2$ are described by:

$$k'_x x + k'_y y + k'_z z = c_1 \quad (4.86)$$

$$k''_x x + k''_y y + k''_z z = c_2. \quad (4.87)$$

In non-dissipative media, we require the following equation to be satisfied for all values of k (Brekhovskikh, 1980):

$$k_x^2 + k_y^2 + k_z^2 = k^2. \quad (4.88)$$

If k is real, the imaginary part of equation (4.88) has to vanish:

$$2k'_x k''_x + 2k'_y k''_y + 2k'_z k''_z = 0, \quad (4.89)$$

which is identical to:

$$\vec{k}' \cdot \vec{k}'' = 0. \quad (4.90)$$

A non-trivial solution of Eq. (4.90) is when $\vec{k}' \perp \vec{k}''$. The planes with constant phase are perpendicular to the planes with constant amplitude. Inhomogeneous waves are not damped in the direction of propagation \vec{k}' , but perpendicular to this direction. When the medium is lossy, a homogeneous wave has already a complex wave vector $k = \beta + i\alpha$. In case of an inhomogeneous wave, the planes of equal phase and equal amplitude are not perpendicular one to another any more (Brekhovskikh, 1980).

We can define a coordinate system in that way that \vec{k}'_y and \vec{k}''_y vanish, i.e. we restrict on a wave propagating in the x - z -plane. Then, the remaining components can be expressed as:

$$k_x = k \sin \alpha \quad (4.91)$$

$$k_z = k \cos \alpha. \quad (4.92)$$

For complex k_x and k_z , the angle α will also be complex. Thus, inhomogeneous waves can be described by complex angles. When discussing Snell's law, we defined a critical angle of incidence when a homogeneous plane wave is refracted from an optically denser to a less dense medium. When this angle is exceeded, the angle of refraction is getting complex. Thus the homogeneous plane wave

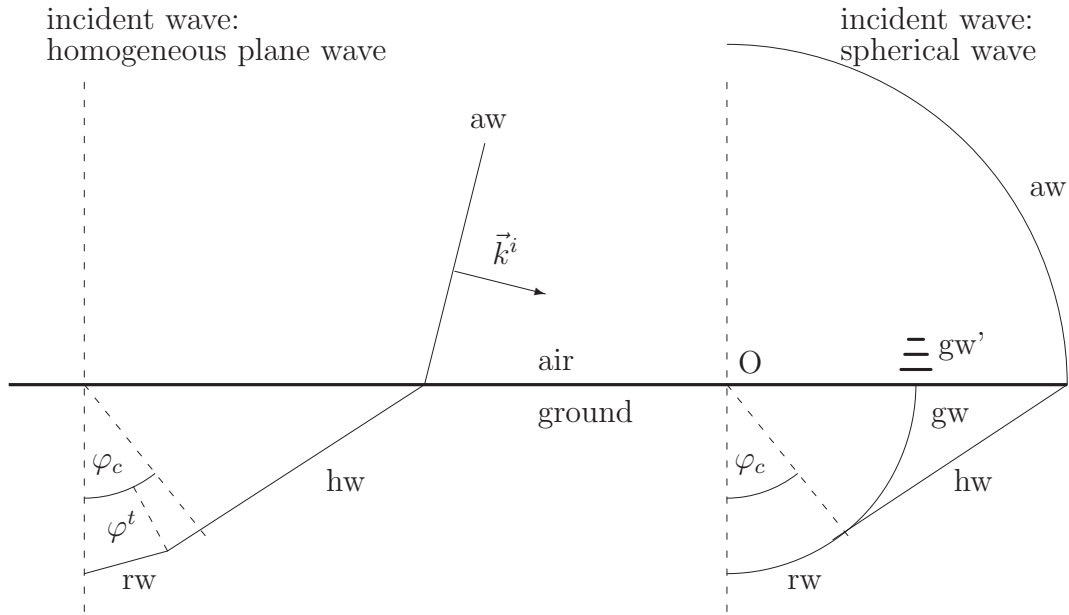


Figure 4.6: Wave fronts of different wave types at the interface air–soil: air wave (aw), groundwave (gw), inhomogeneous wave excited by the groundwave (gw'), head wave (hw), refracted wave (rw). On the left side a homogeneous plane waves reaches the interface from the air: no wave is refracted at $\varphi^t > \varphi_c$. On the right side, a spherical wave is emitted by the source placed at the point O just above the ground surface: the wave is also refracted at $\varphi^t > \varphi_c$ forming the groundwave.

is refracted as an inhomogeneous plane wave when the angle of incidence is larger than the critical angle. Vice versa, an inhomogeneous plane wave can convert into a homogeneous plane wave during transition from an optically less dense to a denser medium.

If a homogeneous plane wave is refracted from air ($\varepsilon_r^{air} = 1$) into soil, the angle of refraction φ^t will be smaller than the angle of incidence φ^i which is limited to 90° . Thus, these waves can only be refracted to a maximum angle $\varphi_{max}^t = \varphi_c = \arcsin(k^{soil}/k^{air})$. A typical value for moist soils is $\varepsilon_r^{soil} = 9$, yielding a critical angle of $\varphi_c \approx 20^\circ$. Beyond this angle, no homogeneous plane waves will be refracted into the soil (Fig. 4.6, left side).

As a first approximation, a GPR antenna emits spherical waves which can mathematically be described as superposition of homogeneous and inhomogeneous plane waves (Brekhovskikh, 1980). As the latter have a complex angle

of incidence, they can be refracted as homogeneous waves with an angle of refraction larger than the critical angle, as shown above. Thus, energy is also refracted in the angular range $\varphi_c < \varphi^t < 90^\circ$ (Fig. 4.6, right side). The wave with $\varphi^t = 90^\circ$ will propagate parallel to the interface soil–air and is called the groundwave of GPR. This homogeneous wave declines with the square of the distance to the source. The groundwave excites an inhomogeneous wave in air, declining exponentially with rising distance to the interface (King et al., 1992). It is this wave (gw’), and not the groundwave (gw) itself, which is recorded by the receiving antenna placed at the interface air–soil. The groundwave (gw and gw’) is of opposite phase to the air wave (Du, 1996). It is also of opposite phase to reflected waves if the k -values increase with depth which holds true for most GPR applications, as soil moisture usually will rise with depth.

The considerations above describe the principles of development of the groundwave and illustrate why energy can be refracted into the angular range beyond the critical angle. The dynamics, i.e. the amplitudes of the groundwave is of rather complicated nature as it is a function of the dielectric properties of the soil, the layout of the antenna and the measuring setup. As only traveltimes of the groundwave will be analysed, the exact mathematical solution describing the field strength will not be deduced. An analytical solution for a horizontal electric dipole at a plane boundary can be found in King et al. (1992).

4.3 Determining Permittivity by the Coefficient of Reflection

4.3.1 Coefficient of Reflection at the Interface Air – Soil

We have already deduced the coefficient of reflection when a plane wave is reflected at an interface. Regarding the interface air–soil and with the well-known parameters of air, $\varepsilon_r^{air} = 1$, $\mu_r^{air} = 1$ and $\sigma^{air} = 0$ S/m, Eq. (4.72) simplifies to:

$$\rho = \frac{\mu_r^{soil} - \sqrt{\mu_r^{soil} \varepsilon_{eff}^{soil}}}{\mu_r^{soil} + \sqrt{\mu_r^{soil} \varepsilon_{eff}^{soil}}}. \quad (4.93)$$

For most applications (Chanzy et al., 1996; Grote et al., 2005; Huisman et al., 2003a; Serbin and Or, 2003), only the relative permittivity of soil is considered

and the permeability as well as the conductivity of soil is neglected:

$$\rho = \frac{1 - \sqrt{\varepsilon_r^{soil}}}{1 + \sqrt{\varepsilon_r^{soil}}} . \quad (4.94)$$

In Fig. 4.7 the coefficient of reflection is plotted versus the magnetic permeability, the dielectric permittivity and the electric conductivity of soil using Eq. (4.93) at a frequency of 800 MHz which corresponds to the centre frequency of the used antenna. The depicted range of the parameters corresponds to the maximal range of natural soils. The relative permeability is between 1 and 1.1 which corresponds to completely non-magnetic and highly magnetic soils (own measurements on tropical soils⁵) where the relative permittivity rises from 2.5 to 30 according to dry and water saturated soils. The maximum conductivity is 0.2 S/m which represents a quite conductive soil where GPR will begin to work not properly any more. When conductivity is unequal zero, the coefficient of reflection is getting complex. Not only a part of the energy will be reflected, but also a phase shift will occur and the wavelet will be deformed.

Figure 4.7 demonstrates that only the permittivity of soil will significantly determine the coefficient of reflection. The effect of permeability and conductivity can be neglected when common soils are considered. When regarding an ordinary moist soil ($\varepsilon_r^{soil} = 9$) for example, a large increase in conductivity from $\sigma = 0.001$ S/m to $\sigma = 0.1$ S/m will only lead to a relatively small overestimation of the deduced permittivity compared to the true permittivity ($\varepsilon_r^{deduced} = 9.45$).

The effect of the Debye relaxation of water (Eq. (4.4)) on the imaginary part of the effective permittivity is not taken into consideration in the determination of the coefficient of reflection as it is negligible. When regarding the interface air–water at a temperature of 20 °C, the effect of Debye relaxation on ρ at 800 MHz is only 0.02% for the absolute value and 0.04% for the phase. These are the maximal effects which may be encountered. As we see, approximation (4.94) is justified and results in:

$$\varepsilon_r^{soil} = \left(\frac{1 - \rho}{1 + \rho} \right)^2 . \quad (4.95)$$

⁵The magnetic permeability of iron and aluminium rich tropical soils (ferralsols (FAO, 2006)) was measured at frequencies from 50 Hz to 1 kHz. Due to the lack of measurements of the magnetic susceptibility of natural soils at radar frequencies (Olhoeft, 1998), the measurements at relatively low frequencies are taken as maximum values as susceptibility generally decreases with increasing frequency.

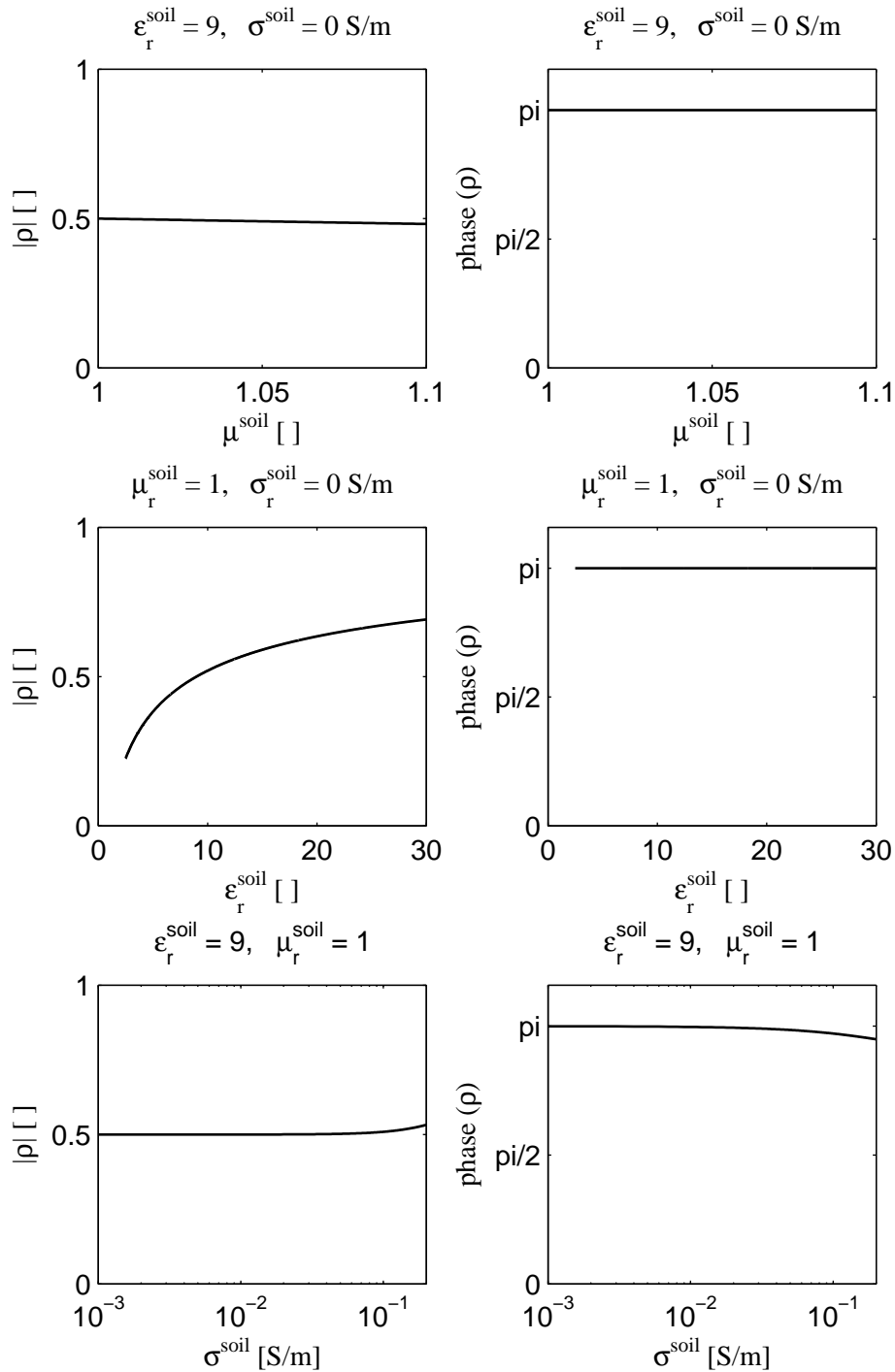


Figure 4.7: Coefficient of reflection ρ at the interface air–soil at 800 MHz depending on the soil properties: relative permeability, relative permittivity, and conductivity. The absolute value (left side) and the phase (right side) is plotted. Note, that ρ is real when $\sigma = 0 \text{ S/m}$ and is getting complex when the conductivity is not negligible.

Since we do not know the amplitude of the emitted wave, we can not calculate the coefficient of reflection directly by using the absolute amplitude of the reflection. We will have to calibrate the system by recording the reflected amplitude of a metal plate which has to be at least as large as the first Fresnel zone and is placed at the same distance as the interface air–soil. As we know the coefficient of reflection of a metal plate to be equal to $\rho_{metal} = -1$, the coefficient of reflection at the interface air–soil is:

$$\rho_{soil} = -\frac{E_0^{soil}}{E_0^{metal}} , \quad (4.96)$$

where E_0^{soil} is the amplitude of the reflection from the soil surface and E_0^{metal} the amplitude of the reflection from the metal surface.

The coefficient of reflection is determined by the contrast in permittivity at the interface air–soil. When using high frequencies, the measuring depth is restricted to the first few centimetres of the soil (Serbin and Or, 2003; Ulaby et al., 1996).

The Fresnel formulas and therefore Eq. (4.95) only hold true for smooth interfaces. An increase in surface roughness will decrease the magnitude of the reflected signal as energy will be scattered away from the antenna. In radar remote sensing, when assuming normal incident waves, surfaces with roughness of the order of $\lambda_{air}/10$ are considered smooth (Makinde et al., 2005). Other authors (Chanzy et al., 1996) use the Rayleigh criterion and define a surface as smooth when the average variation of the height $h < \lambda_{air}/8$. When using a 1 GHz horn antenna (0.8 GHz centre frequency) and assuming normal incidence, the interface air–soil can be regarded as smooth when the RMS deviation σ_h of micro topography is smaller than:

$$\sigma_h = \sqrt{\frac{1}{N} \sum_{i=1}^N (h_i - \bar{h})^2} < \frac{\lambda_{air}}{10} = \frac{c_0}{10\nu} \approx 0.04 \text{ m} , \quad (4.97)$$

where h_i is the height of the surface above a reference and \bar{h} its mean. For the locations where the measurements were carried out, this constraint is maintained, i.e. σ_h inside an area corresponding to the first fresnel zone is smaller than 0.04 m.

Another factor potentially affecting the amplitude of the reflected wave is vegetation (Serbin and Or, 2003). The height of the vegetation and its density will influence the amplitude. Also the direction of the culms in regard to the



Figure 4.8: Picture of experimental setup to determine the coefficient of reflection: A 1 GHz GSSI horn antenna is mounted on a sledge 0.53 m above the ground.

\vec{E} -field and the moistening, e.g. by dew or rain, influences the effects. The higher the frequency, the higher the horizontal resolution, but the more surface roughness or vegetation affects the results.

4.3.2 Experimental Setup

As we already have shown, we can deduce the permittivity of the soil surface by determining the coefficient of reflection at the interface air–soil. An air launched 1 GHz GSSI horn antenna is used which is mounted on a sledge to be operated at a constant distance to the soil (Fig. 4.8). The minimal distance antenna–soil is determined to the distance at which the reflected wave and the direct wave do not interfere any more.

Figure 4.9 shows three exemplarily radar traces using the described setup on a metal plate, on soil without vegetation and on soil with vegetation (approximately 0.2 m long grass). The amplitudes are normalised so that the maximal amplitude of the metal reflection is 1. The primary wavelet starting at 1 ns is a superposition of different waves emitted by the transmitter and reaching the receiver inside the antenna housing and therefore is not representative for the emitted wavelet. The reflected wave appears at 6 ns. The first strong deflec-

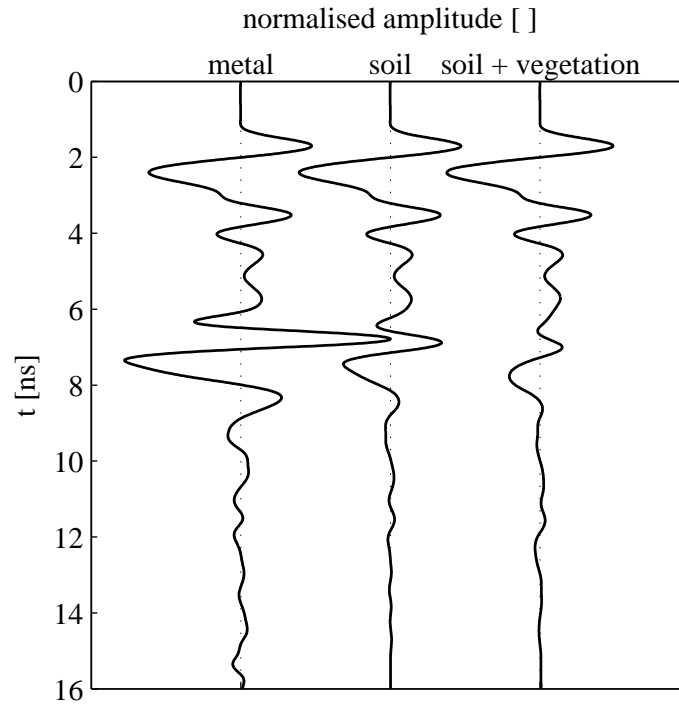


Figure 4.9: Radar trace of a 1 GHz horn antenna showing a wave reflected at a metal plate, a soil surface without vegetation and a soil surface with vegetation. The amplitude is normalised to the maximum amplitude of the metal reflection.

tion to the right at approximately 6.5 ns is used for calculating the coefficient of reflection. This phase is preferred to later phases or to the envelope because it can easily be identified and picked. Furthermore, the first maximum is the phase which is less disturbed by reflections of the sledge or interfaces within the soil.

The horizontal resolution is commonly estimated by the first Fresnel zone because only this area contributes to the energy recorded at the antenna. With the dominant frequency of the horn antenna of 0.8 GHz and the height of the antenna above ground of 0.53 m, the diameter of the first Fresnel zone is approximately 0.65 m (Eq. (4.84)). In the strict sense, the Fresnel zone is only defined for mono-frequency signals, but not for broad band impulse-radar signals. Furthermore, the Fresnel zone is a rather rough estimation of the horizontal resolution as a horn antenna has a focusing characteristic yielding a higher resolution.

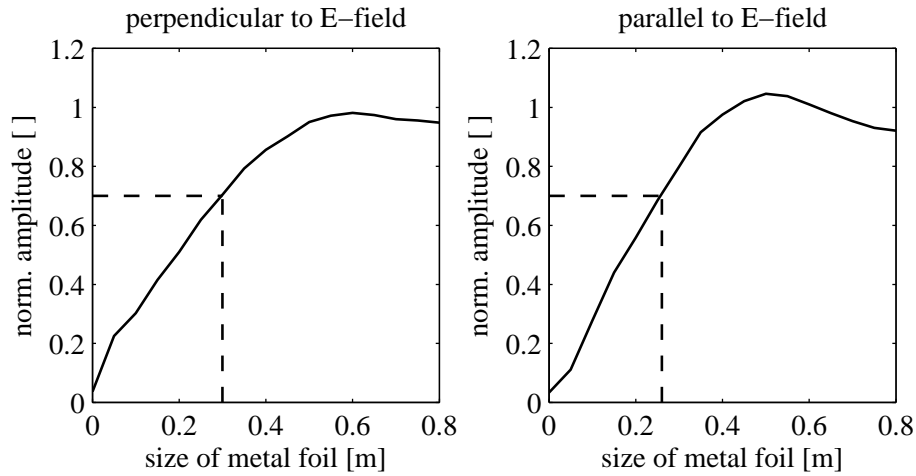


Figure 4.10: Experimental determination of the footprint of the horn antenna. The size of a metal foil which is serving as a reflector is varied in the direction perpendicular to the E-field and parallel to the E-field of the emitted waves. The amplitudes are normalised to the reflection of a large metal plate. The -3 dB (70%) criterion is plotted to determine the footprint.

Therefore, the footprint⁶ of the used horn antenna was determined by an experiment. The antenna was mounted at the same height above a plastic plate as it will be operated above soil during the field measurements. The plastic plate itself caused no significant reflection. On this plate, an aluminium foil was placed causing a part of the energy to be reflected. The size of the foil was varied stepwise and a radar trace was recorded in each case. In Fig. 4.10 the amplitude of the reflected wave was plotted versus the size of the metal reflector. The size was varied in the direction perpendicular to the E-field of the emitted waves (i.e. the common profile direction of the antenna, see Fig. 4.8) while it was held constant and was larger than the first Fresnel zone in the other direction (i.e. perpendicular to the normal profile direction). Then, the same experiment was carried out in the other direction, i.e. the size of the metal reflector was varied parallel to the E-field. The amplitudes normalised to the reflection of a large metal plate are plotted in Fig. 4.10. The amplitude of the reflected wave rises from nearly 0 when there is no metal foil to approximately 1 when the foil is getting larger. According to the -3 dB criterion which is commonly used in antenna theory to determine the main coils

⁶The footprint is the area which is illuminated by an antenna and defines the lateral resolution (Wessel, 2006).

of radiation and the footprint of an antenna (Rothammel and Krischke, 2001; Wessel, 2006), the footprint is determined to the size of the metal reflector yielding to -3 dB of the maximal amplitude. In other words the footprint is the area which causes 70% of the recorded amplitude. From Fig. 4.10 one can read that the footprint in profile direction is approximately 0.3 m and 0.25 m in the perpendicular direction. This area is more than five times smaller than the area of the first Fresnel zone. Thus, for the used horn antenna and setup, spatial resolution is actually much higher than specified by the Fresnel zone.

Figure 4.11 shows the results of a profile measurement on a green land (location 2, Appendix B). The top of the soil was quite dry during the experiments. The measurement with the horn antenna using a space increment of 0.05 m along a 10 m profile was carried out before and after the grass had been cut to the ground. The measurement with vegetation yields smaller amplitudes of the reflected waves (see Fig. 4.9) and therefore lower coefficients of reflection and consequently lower deduced permittivities. This is caused by the fact that grass reflects and scatters a part of the energy and the impedance contrast between air and soil is not that sharp with grass than without. Despite the shift between both curves, they show similar features.

To check the results, the permittivity was determined every 0.1 m using a TDR probe. The individual readings are displayed as well as a running average over 0.3 m in order to emulate the integrating character of the GPR method. TDR yields higher permittivities than deduced by the coefficient of reflection. This is probably caused by different measuring depth of both techniques. When the coefficient of reflection is determined by only the first few centimetres of the ground (Serbin and Or, 2003), the TDR probe provides an integral value over the length of the rods (see Fig. 4.3) which is 0.11 m for the used probe. As usually porosity is higher and water content is lower at the surface than in deeper regions this will result in a rise of permittivity from the surface to deeper regions. Furthermore, both methods provide different horizontal resolution. The permittivity derived by GPR represents an area of approximately 0.3 m \times 0.25 m, whereas TDR yields a more punctual measurement. The volume of influence of the used TDR probe (IMKO TRIME P2) is restricted to slightly more than the volume in between the two rods, i.e. the volume corresponds to a cylinder with 0.03 m diameter and 0.11 m length (Stacheder, 1996). Measuring accuracy of water content of the TDR system is specified to 1–2vol% what corresponds to an accuracy of approximately 0.5–1 in relative permittivity ϵ_r . The TDR data can only be averaged along the profile direction and not perpendicular to this as due to the measuring expenditure

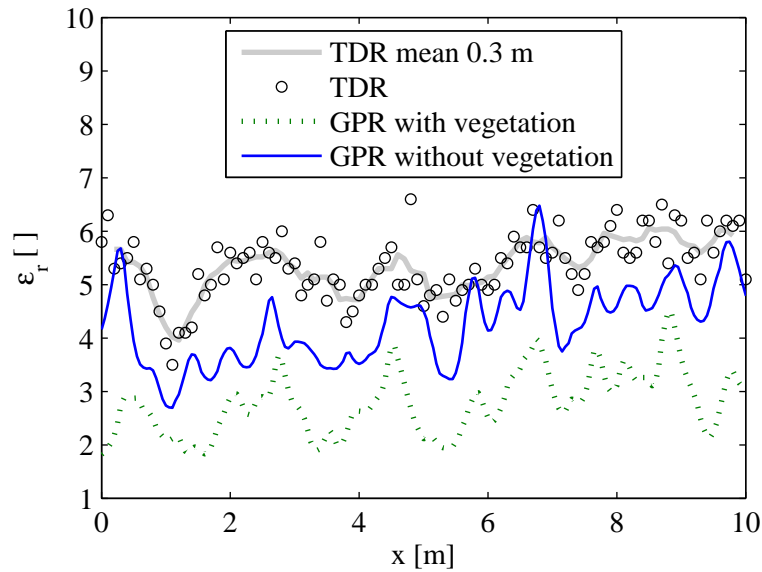


Figure 4.11: Permittivity distribution along a 10 m profile on a green land determined by the coefficient of reflection. The measurement has been carried out before and after cutting the grass. The permittivity determined with a TDR probe is displayed for comparison.

of TDR only a measurement along the profile, but no areal measurement was carried out. Recapitulating, as TDR and GPR provide different horizontal and vertical measuring areas, they will not coincide exactly but they show the same characteristics as can be seen in Fig. 4.11.

Estimation of accuracy

The accuracy of the deduced permittivities is determined by the inaccuracy of the radar equipment, e.g. a temporal drift of the amplitudes, and by deviations of the assumed model to reality, e.g. by effects of vegetation or surface topography.

Generally, a GPR device shows a drift when it is operated for a longer length of time. In order to determine the drift of the used device (GSSI SIR 20), the setup which is described above (Fig. 4.8) is used to determine the coefficient of reflection of a metal plate during 3 hours. The central unit was turned on for 10 minutes before starting the measurement as this corresponds approximately to the time one will need to adjust the settings before carrying out a field measurement. The normalised amplitude of the first strong onset of the reflected wavelet is depicted in Fig. 4.12 as well as the traveltime of the

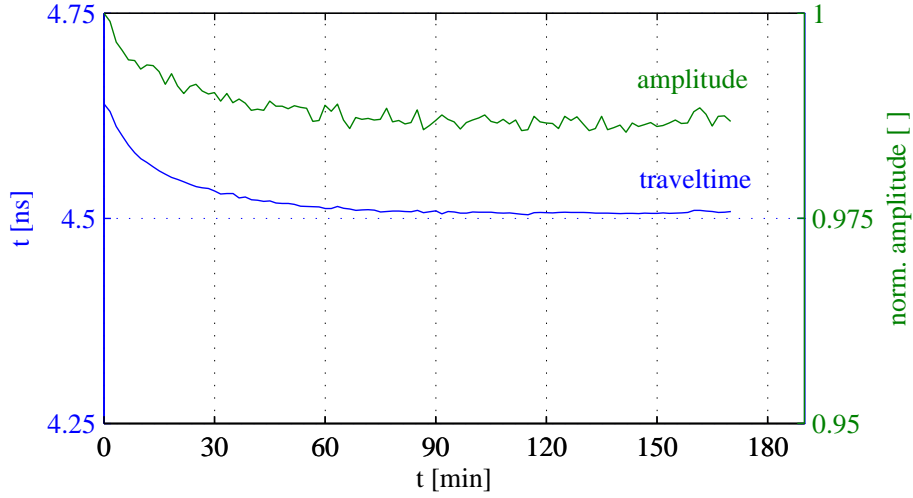


Figure 4.12: Amplitude and time drift of the GPR system (GSSI SIR 20 and 1 GHz horn antenna). The first onset of the reflected wave is picked to determine the amplitude and the first zero-crossing is picked for the traveltime.

first zero-crossing. The temporal drift of traveltime and amplitude seem to correlate. It is higher during the first hour and is marginal for longer times. The drift of the normalised amplitude during 3 h is approximately 0.015. The resulting error in permittivity is deduced from Eq. (4.95) to:

$$\Delta\epsilon_r = \left| \frac{\partial\epsilon_r}{\partial\rho} \right| \Delta\rho = \left| 4 \frac{1-\rho}{(1+\rho)^3} \right| \Delta\rho. \quad (4.98)$$

When assuming a moist soil with a permittivity of $\epsilon_r^{soil} = 9$, the coefficient of reflection is $\rho = -0.5$. Then, the amplitude drift of the GPR device results in an error of $\Delta\epsilon_r = 0.72$.

A source of error hard to quantify is surface roughness and vegetation. The influence of vegetation is illustrated in Fig. 4.11 and will be discussed in the next section. Vegetation reduces the apparent relative permittivity of the soil as well as its variability. It should be removed or at least trimmed if accurate permittivity values have to be determined. Otherwise, only variations and trends of the spacial distribution can be deduced. Surface roughness reduces the coefficient of reflection because a part of the energy is scattered and does not reach the receiving antenna. Thus, the relative permittivity appears to be lower than it actually is. This has to be taken into consideration in case surface roughness cannot be neglected. But at the investigated locations,

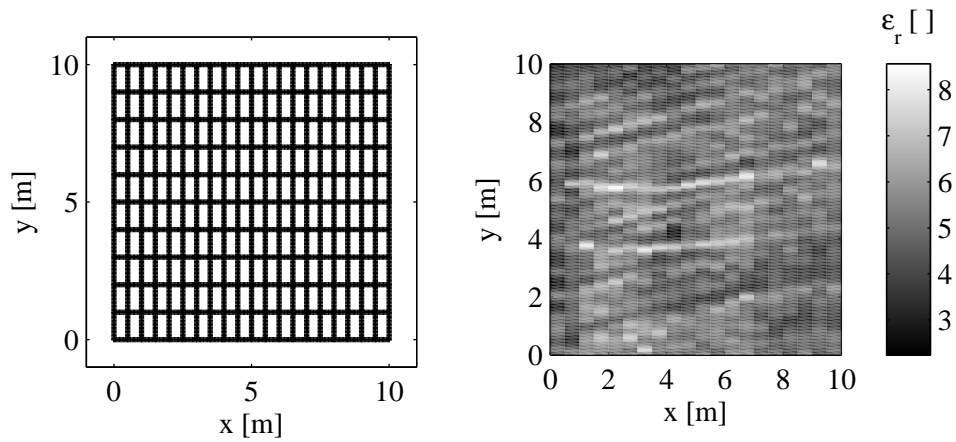


Figure 4.13: Measuring grid (left) and deduced permittivities from the coefficient of reflection of the profiles in y -direction without vegetation (right).

micro-topography was below the critical value of Eq. (4.97).

4.3.3 Spatial Field Measurements and Statistical Analysis

Location 2

The field measurements were carried out on location 2 (see Appendix B). The coefficient of reflection was determined on a 10 m \times 10 m area along a regular grid (Fig. 4.13) before and after removing the vegetation. In Fig. 4.14, the experimental probability density function of the in situ permittivity distribution is depicted as well as a graph of a normal distribution with the same mean and standard deviation as the experimental data for comparison. Both distributions match the normal distributions quite well, so the permittivity can be regarded as normal distributed. The mean and the standard deviation is smaller with vegetation than without ($\epsilon_r = 3.6 \pm 0.8$ compared to $\epsilon_r = 4.6 \pm 0.9$) which is an effect of the reduced absolute values and variation of the permittivity by the vegetation as demonstrated in Fig. 4.11.

On the right of Fig. 4.13 the permittivity along the profiles in y -direction is displayed. One can recognise a parallel structure in the permittivity distribution inclined by approximately 15° to the x -axis. Due to this structure, the variogram was calculated in different directions. The variograms in the two directions in which the radar measurements were carried out are displayed in

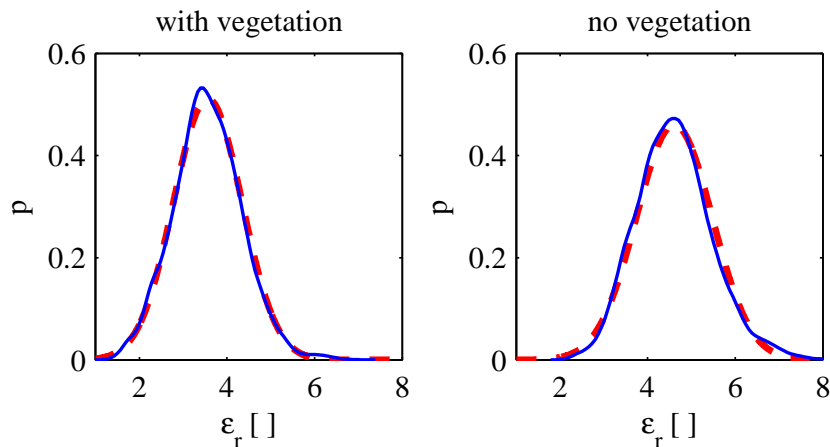


Figure 4.14: Experimental probability density function of permittivity distribution in situ (blue solid) and normal distribution with same mean and standard deviation as in situ for comparison (red dashed). Soil with vegetation (left) and soil without vegetation (right). The mean and the RMS deviation are: with vegetation $\varepsilon_r = 3.6 \pm 0.8$; without vegetation $\varepsilon_r = 4.6 \pm 0.9$.

Fig. 4.15. The variograms show lower sill values for the measurements with vegetation than without due to the reduced variance by the vegetation (see Fig. 4.11). The correlation length are comparable with and without vegetation.

The variograms in x -direction differ significantly from the variograms in y -direction. An exponential model is fitted to the experimental data yielding different ranges in x - and y -direction. The adapted exponential models have similar sills in the two directions, but different ranges: $a_x = 1.7$ m and $a_y = 0.5$ m with vegetation and $a_x = 1.8$ m and $a_y = 0.45$ m without vegetation. Thus, we are concerned with a geometrical anisotropy of the permittivity distribution. As the used measuring grid does not provide a very good azimuthal resolution, the major direction of anisotropy is set to the direction of the parallel structure to $\alpha \approx 15^\circ$. The anisotropy factor is determined by analysis of the variograms to $\lambda = a_{max}/a_{min} \approx 5$. This factor only represents the mean characteristics of the permittivity pattern at the location but not the maximum length of individual structures. Some of them expand on larger areas in direction of $\alpha \approx 15^\circ$ than indicated by variogram analysis.

The deduced parameters are used for kriging the data and the results are displayed in Fig. 4.16. One can clearly recognise the parallel structure in the

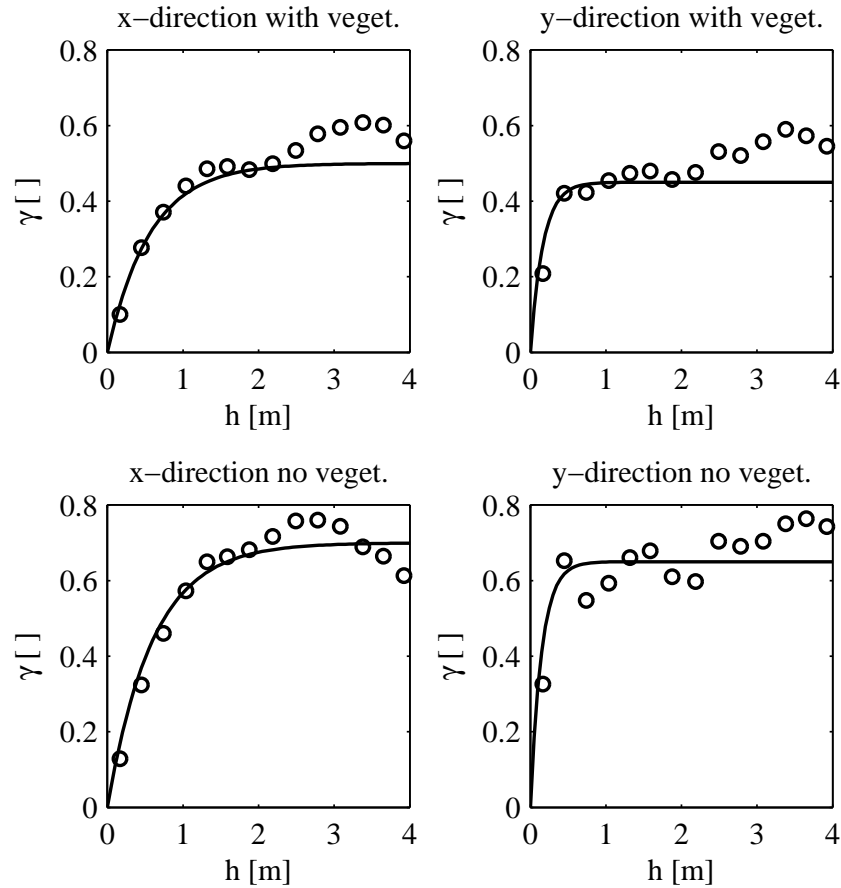


Figure 4.15: Variograms of permittivity distribution determined by the coefficient of reflection at location 2 before removing the vegetation (top) and after removing the vegetation (bottom). The directional variogram is calculated in x and y direction and an exponential model is fitted to the curves. The range of the fitted model is: with vegetation $a_x = 1.7$ m, $a_y = 0.5$ m; without vegetation $a_x = 1.8$ m, $a_y = 0.45$ m.

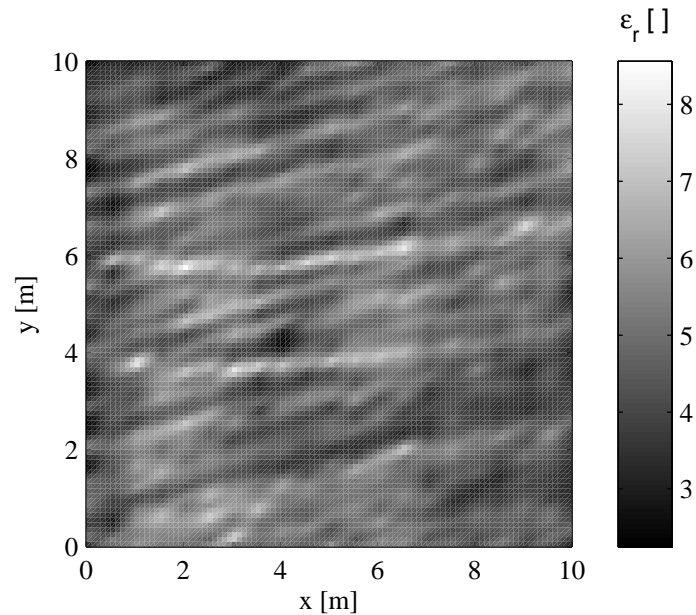


Figure 4.16: 2D distribution of the permittivity deduced from the coefficient of reflection at location 2 after removing the vegetation. The data are gridded with 10 cm increment by kriging using an anisotropic variogram model (Fig. 4.15).

permittivity distribution which can already be seen in Fig. 4.13.

The direction of the structure corresponds to the former direction of cultivation and ploughing as the area was used as an acre up to two years ago. Then, herbage has been sown in the same direction and the area has been used as an extensively landscaped greenland for 2 years. The periodical structure might be a relict of ploughing i.e. due to compaction of the soil or might be related to the grass routs and the augmented evapotranspiration. In any case, it is evoked by the cultivation of the area. At $y = 4$ m and 6 m one can notice two parallel traces of high permittivity which deviate from the 15° direction of the other structures. The parallel lines are probably the trace of an agricultural vehicle which compacted the topsoil layer and consequently raised the permittivity.

Location 3

The permittivity distribution has also been determined on location 3 (see Appendix B) after removing the vegetation. Figure 4.17 shows the experimental probability density function of the deduced permittivities. A graph of a normal distribution is plotted for comparison. One can recognise that the permittivity has a positive skewness but fits the normal distribution quite well when the log-

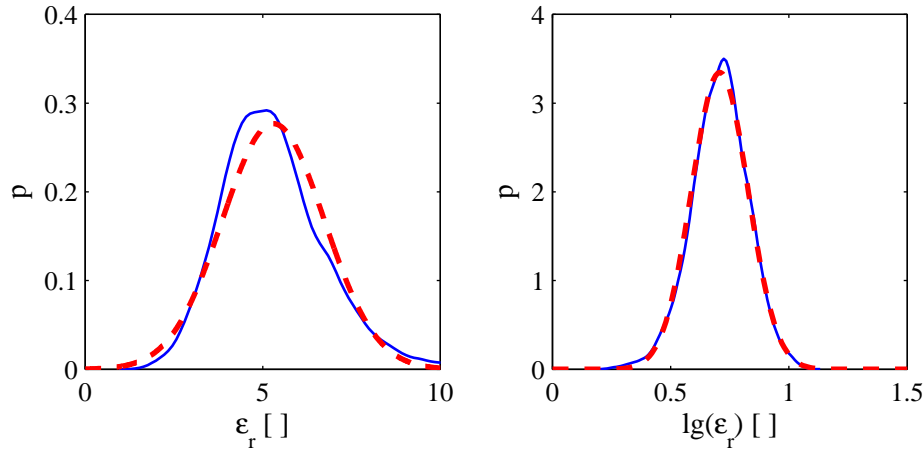


Figure 4.17: Statistical analysis of the permittivity distribution determined by the coefficient of reflection at location 3. Experimental probability density function (blue solid) and normal distribution (red dashed) with the same mean and standard deviation as in situ for comparison. Left side, relative permittivity: $\varepsilon_r = 5.0 \pm 1.0$. Right side, logarithm of permittivity: $lg(\varepsilon_r) = 0.69 \pm 0.08$.

arithm of permittivity is analysed. Thus, we are concerned with a log-normal distribution of the permittivity at location 3 with $lg(\varepsilon_r) = 0.69 \pm 0.08$.

The directional variograms in x - and y -direction do not differ so that the omnidirectional variogram is depicted in Fig. 4.18. As due to the horizontal resolution of the method the first point of the semivariance γ is at $h = 0.3$ m, the rise of the variogram is only determined by one data point. Aware of the fact that other models could also explain the data, an exponential variogram model ($a = 0.45$ m) is fitted because it shows to be the simplest model which easily describes the data. The exponential model could be superposed by a linear function to describe the rise of the semivariance beyond the range. As the slope is small and will not influence the small-scale parameter distribution which is of interest in this work, the linear rise is neglected. However, it should be taken into consideration if the permittivity distribution is regarded on larger scales.

The data are gridded by a kriging algorithm using the exponential variogram model function and are depicted in Fig. 4.19. The spatial pattern of the permittivity shows no directionality and no correlation over larger distances.

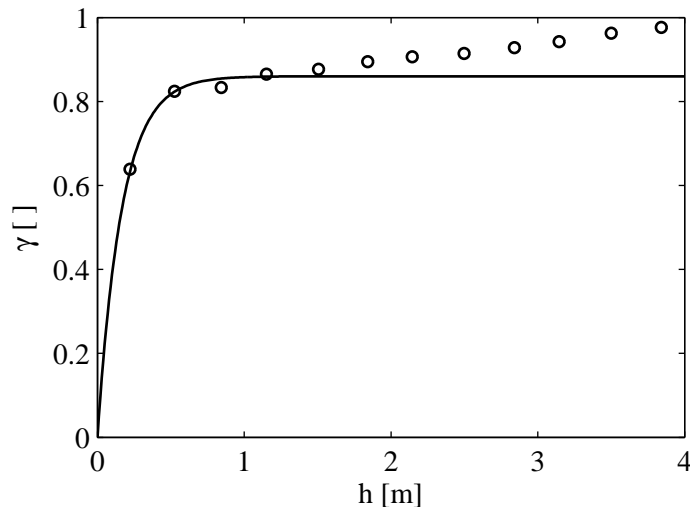


Figure 4.18: Statistical analysis of the permittivity distribution determined by the coefficient of reflection at location 3. Omnidirectional experimental variogram and exponential model with range $a = 0.5$ m.

On this site, the horizontal resolution of the reflection coefficient technique is at its limit.

4.4 Determining Permittivity by Using the Groundwave

4.4.1 Velocity of Radar Waves in Soil

In the last section, the permittivity was determined with the coefficient of reflection. In the following, a technique will be developed using the correlation between the permittivity of a medium and the propagation velocity of electromagnetic waves. Just as the coefficient of reflection, wave velocity depends on the three electromagnetic parameters. In Fig 4.20 the velocity is plotted versus the magnetic permeability, the dielectric permittivity and the electric conductivity using Eq. (4.46) and according to the ranges of common soils. The same ranges are used as for the coefficient of reflection. As for frequencies $\nu < 1.5$ GHz the relative permittivity ϵ_r shows only a weak dependence

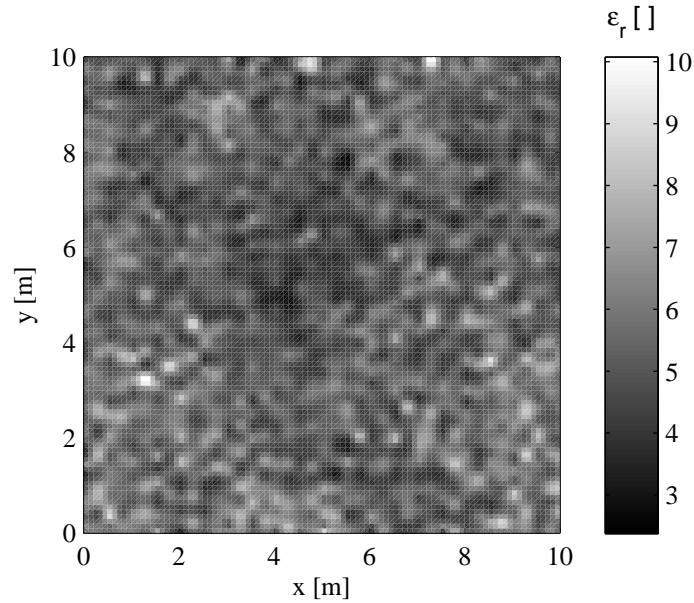


Figure 4.19: 2D distribution of the permittivity derived by the coefficient of reflection at location 3. The data are gridded with 0.1 m increment by kriging using the isotropic variogram model of Fig. 4.18.

on frequency (Dam et al. (2005) and Fig. 4.2), it is regarded as constant. Therefore, the frequency dependence of ε_{eff} is only determined by the electric conductivity (Eq. (4.40)).

Figure 4.20 demonstrates that the permittivity is the parameter which determines the velocity of electromagnetic waves and that the effect of permeability and conductivity can be neglected when regarding common soils (see section 4.3) in which radar waves propagate.

In analogy to section 4.3, the effect of Debye relaxation on the imaginary part of ε_{eff} is not considered in Fig. 4.20. When regarding 100% water at 20 °C which represents a worst case scenario, the effect of the imaginary part of ε_{eff} on the velocity v due to relaxation processes of the water molecule is only 0.02% and therefore negligible.

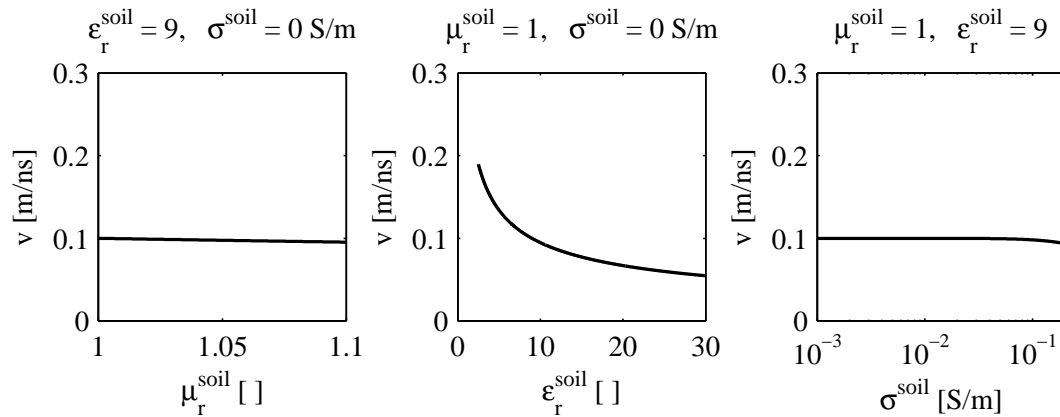


Figure 4.20: Phase velocity v at 400 MHz depending on the soil properties: relative permeability, relative permittivity and conductivity.

4.4.2 Groundwave Measurements – State of the Art

The groundwave of GPR is a plane wave traveling in the soil parallel to the interface soil–air. Its appearance by over-critical refraction of spherical waves has been discussed in section 4.2.5. Due to constraints of continuity, an inhomogeneous wave is excited in the air by the groundwave (see Fig. 4.6). As radar antennas usually are operated above the soil surface, it is not the groundwave gw itself which is registered with the receiver antenna, but the guided inhomogeneous wave in air gw'. Both waves, gw and gw', propagate with the same lateral velocity and have opposite phase compared to the air wave and waves reflected at optically denser media.

The groundwave of GPR has been used to determine the permittivity for deducing soil moisture for about 10 years. It is the only wave traveling through the ground with a propagation path that is a priori known. It has proven to be a fast technique which can be used to map large areas and to yield reasonable results when compared to other methods like TDR or gravimetric soil moisture determination (Du, 1996; Galagedara et al., 2005; Grote et al., 2003; Hubbard et al., 2002; Huisman et al., 2001, 2002, 2003a,b; Overmeeren et al., 1997; Sperl, 1999; Wollny, 1999).

There are two principle modes a groundwave measurement can be carried out. The first one is to perform a moveout (MO)⁷ or a common mid point (CMP)

⁷A moveout (MO) measurement is also known as wide angle reflection and refraction

measurement by separating both antennas (Overmeeren et al., 1997; Huisman et al., 2001). When plotting the travel time versus the distance of the transmitter and receiver antenna, the air wave and the groundwave appear as a straight line and their slopes correspond to the reciprocal value of the wave velocity in air $1/c_0$ and soil $1/v_{soil}$, respectively (Fig. 4.21 left part, $x < x_{opt}$). This holds true for soils which can be regarded as homogeneous. In this case, the permittivity of the soil can be determined at the location where the CMP or MO measurement was carried out by fitting a straight line to the groundwave.

The prolongation of the air and groundwave (dashed lines in Fig. 4.21) intersect at the origin and this point is used to define time-zero in practice.

The second method is to carry out a constant offset (CO) measurement by moving the fixed transmitter–receiver layout along a profile and measure lateral changes in the velocity of the groundwave (Grote et al., 2003) (Fig. 4.21 right part, $x > x_{opt}$). In this mode, the permittivity distribution along a profile can be deduced rapidly. However, it can be a challenge to identify the groundwave in solely a CO measurement especially in laterally and vertically heterogeneous soils where numerous phases will interfere.

A combination of both methods was proposed by Du (1996) and showed to be the most appropriate to this date. First, a moveout measurement is carried out by separating the transmitter and receiver antenna. The optimal transmitter–receiver offset x_{opt} is determined to the distance where the air and groundwave are separated and do not influence one another or interfere with reflected or critically refracted waves⁸. Then, the setup is fixed and the profile is mapped with a CO setup as illustrated in Fig. 4.21. This procedure ensures the correct identification of the different phases in the radargram.

The approach introduced above has some basic disadvantages:

- Measurements in two modes (MO and CO) have to be carried out which require a modification of the layout and thus are time consuming.
- Processing and interpretation of the mixed MO and CO data is time consuming, too. This is especially the case when 2D permittivity distributions are to be determined which requires a large amount of parallel profiles.
- If soil is heterogeneous, the groundwave will not appear as a linear phase

(WARR) measurement.

⁸Critically refracted waves are reflected waves which reach the soil–air interface under the critical angle and therefore are refracted in the air parallel to the interface.

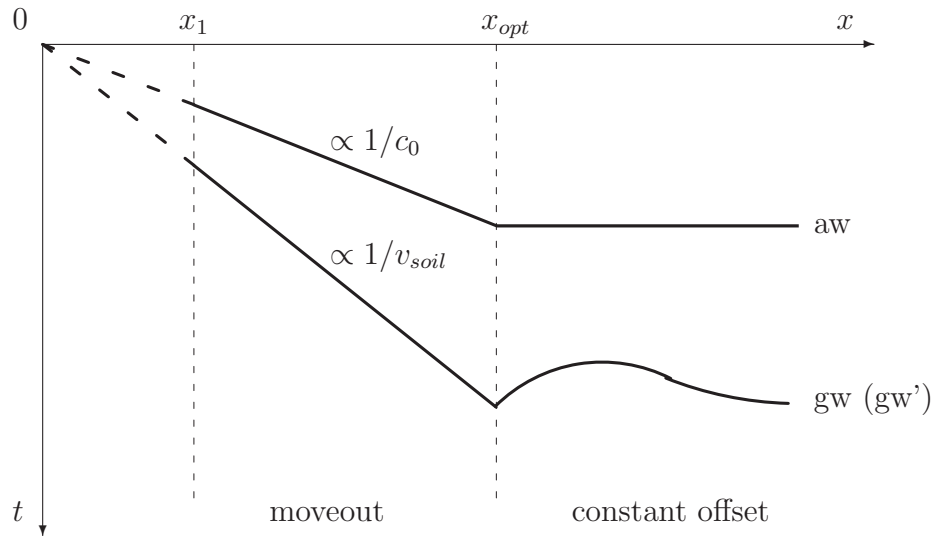


Figure 4.21: Schematic traveltime diagram of a groundwave measurement consisting of a moveout measurement from x_1 to x_{opt} followed by a constant offset measurement at $x > x_{opt}$ (aw: air wave, gw: groundwave).

in the MO measurement. It will be curved or undulating (see chapter 5) and identifying the groundwave and determining its velocity by adapting a straight line may not be possible.

- In the CO mode one will have to operate the antennas at a minimal offset at which the air and groundwave are separated. This distance determines the lateral resolution of the measurement which is in between about half and a few metres depending on the used antennas and the permittivity of the soil. Thus, the optimal separation can vary across a field making it difficult to choose an appropriate antenna separation (Huisman et al., 2003a). The smaller the antenna offset the higher the spatial resolution but the more difficulties will arise to pick the right phase due to interfering air and groundwaves (Galagedara et al., 2005; Grote et al., 2003; Hubbard et al., 2002; Sperl, 1999).

To overcome the relatively poor lateral resolution which is determined by the transmitter–receiver offset, Müller et al. (2003) and Schmalholz (2007) proposed to use a smaller space increment than antenna offset and to carry out overlapping measurements along a profile. The velocity distribution along the profile is determined by an inversion of the picked traveltimes resulting in a better lateral resolution than with a conventional interpretation. With this

technique, a resolution of less than 0.2 m can be achieved when using 1 GHz antennas (Schmalholz, 2007). But the other points still limit the measuring progress and the accuracy especially in heterogeneous soils. At last, carrying out an inversion is time consuming and the result will at some point depend on the chosen inversion parameters.

Some authors point out the integrating character being an advantage of ground-wave measurements with conventional technique over the more point-like TDR measurements. However, it is always better to achieve a high resolution and eventually interpolate the data afterwards instead of determining an averaged distribution. One will get additional information on the variance of the parameter in situ. Therefore, the groundwave technique should be optimised towards high lateral resolution.

4.4.3 Experimental Setup Using 2 Receivers

In the following, a new measurement and interpretation technique will be introduced compensating the disadvantages of the standard technique that are listed above. The essential difference compared to the standard technique is to use two receiver antennas and to determine only traveltime differences between them. Consequently, the lateral resolution is not determined by the distance of the transmitter to the receiver any more but by the distance of both receiver antennas. They can be placed closely one to another yielding a short measuring distance and therefore a high lateral resolution whereas the transmitter can be placed at an optimal distance avoiding superposition of different wave types.

As only traveltime differences are sampled one will not need to determine the air wave for time-zero calibration of the system. Thus, shielded antennas can be used and the first wave detected at the receivers is the groundwave as the air wave and critically refracted waves will not be recorded. The only calibration which is needed is the synchronisation of the two receiving channels at the beginning of the measurement. This calibration is needed e.g. to counterbalance for different cable length to the antennas. The absolute time difference between the channels can for instance be determined by a simple transmission measurement through air. The transmitting antenna is placed vis-à-vis to the two receivers so that the direct wave reaches the two receivers at the same time. Alternatively, a single moveout measurement can be performed separating the transmitter from both receivers and time-zero can be determined in analogy

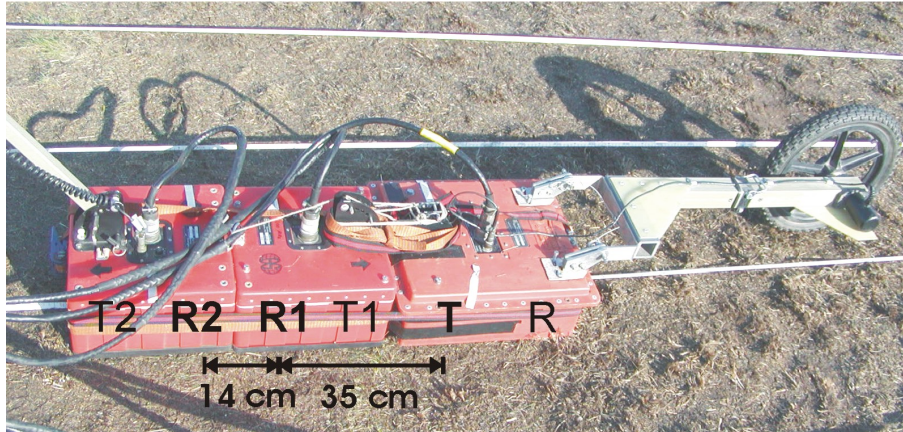


Figure 4.22: Setup used for the measurement of the groundwave. A shielded bistatic 500 MHz GSSI antenna is used as transmitter and 2 shielded bistatic 400 MHz GSSI antennas are the receivers. The position of the antennas in the housing is indicated whereas the actually used antennas are in boldface: T = transmitter, R1 = 1st receiver, R2 = 2nd receiver.

to the standard groundwave technique.

Figure 4.22 shows a picture of the used setup. A 500 MHz GSSI antenna is used as transmitter and two 400 MHz antennas function as the receivers. The slightly different nominal frequency will, if at all, affect both channels in the same way because the two receiving antennas are identical. As impulse radar systems use broadband antennas, the small mismatch in the nominal frequencies is not relevant and enough energy is recorded. The separation between both receiving antennas is 0.14 m and the distance between the transmitter and the first receiver is 0.35 m.

The horizontal resolution is determined by the distance between the two receivers. In order to test this hypothesis, a finite difference calculation was carried out. Anomalies of different sizes and permittivities were placed in a homogeneous medium and a measurement was simulated using a setup resembling the one described above. The centre frequency of the point source was 400 MHz and the dipoles were placed 0.01 m above the ground surface. As no shielded antennas can be simulated with the used software (Sandmeier, 2006), the air wave will interfere with the groundwave when using the same transmitter–receiver distance as in field (0.35 m) where shielded antennas are used. Therefore, the distance from the transmitter to the first receiver is enlarged to 0.7 m, whereas the two receivers have the same separation as in field

(0.14 m). The permittivity of the soil is $\varepsilon_r^{soil} = 3$ corresponding to dry soil and the permittivity of the anomaly is set to $\varepsilon_r^{anom} = 9$ which corresponds to moist soil with a volumetric water content of $\Theta_V \approx 17\text{vol}\%$ when using equation Eq. (4.12), (Topp et al., 1980).

Figure 4.23 shows the results of the FD calculation for a 0.1 m large anomaly. The upper radargram is from the 1st receiver (0.7 m offset) where the lower represents the 2nd receiver (0.84 m offset). The x -axis represents the location of the receiving antenna. The first wave arriving at approximately 3 ns is the air wave which will not be registered in field when using shielded antennas and the second wave is the groundwave. This wave shows undulations when the anomalous zone with higher permittivities is between the transmitter and the particular receiver. The first zero crossing of the groundwave is picked to determine the traveltimes differences between both radargrams and is by way of example marked in red in the upper radargram. The inclined phases at both sides of the anomaly are reflected waves at the sharp lateral interface of the anomaly.

In accordance with Eq. (4.48), the traveltimes differences are transformed in permittivity values resulting in

$$\varepsilon_r = \left(\frac{c_0 (t_2 - t_1)}{\overline{R1R2}} \right)^2 \quad (4.99)$$

when using the setup with two receiving antennas and

$$\varepsilon_r = \left(\frac{c_0 t_1}{\overline{TR1}} \right)^2 \quad (4.100)$$

when using the classical setup. $\overline{TR1}$ is the distance between the transmitter and the first receiver, $\overline{R1R2}$ the distance between the two receiving antennas and t_1, t_2 the traveltimes to the first and second receiver, respectively.

The derived permittivities using the conventional setup and the improved setup are plotted in Fig. 4.24 as well as the model of the anomaly. The x -axis represents the midpoint between the transmitter and receiver for the conventional setup and the midpoint of the two receivers for the improved layout.

Due to the large offset $\overline{TR1}$ of 0.7 m which would be a minimal offset for field applications, the anomaly is blurred when using the classical technique. In contrast, there is a good accordance with the model when using the new technique. Especially the size of the anomaly can be well resolved whereas

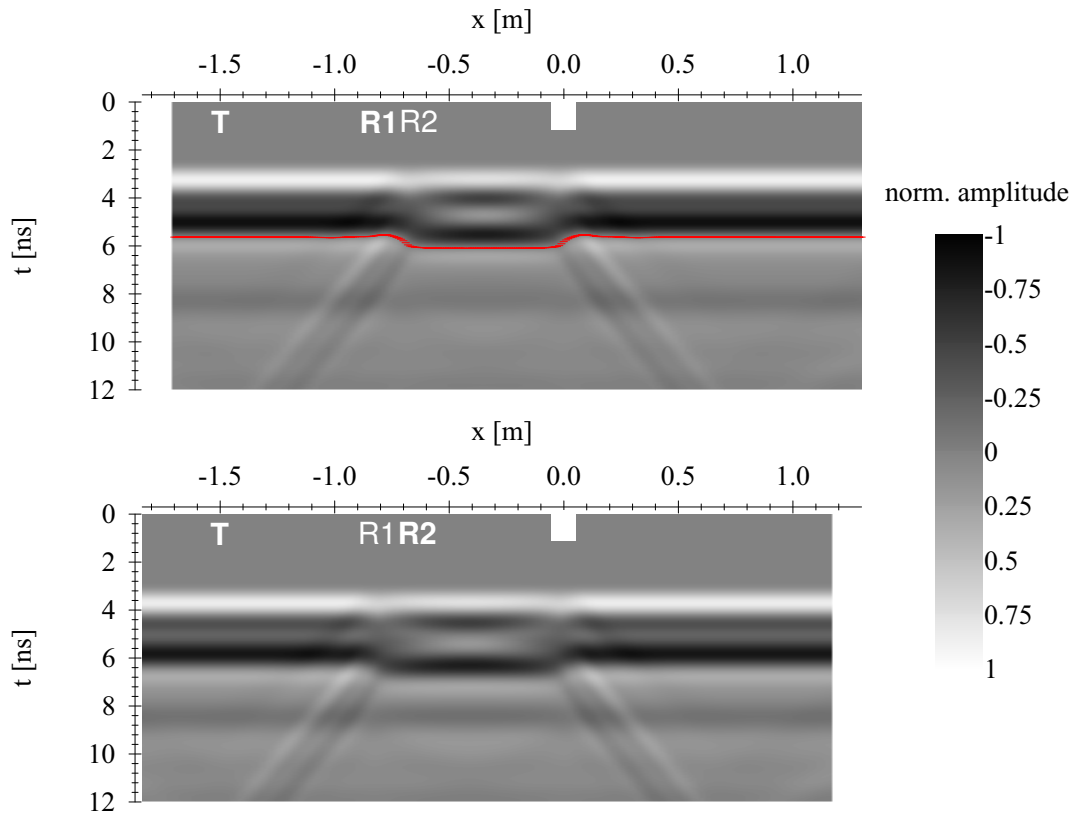


Figure 4.23: FD simulation of CO groundwave measurement on a homogeneous ground with a 0.1 m large anomaly at $x = 0$ m (white box). The active antennas are depicted in boldface (compare 4.22). The distance $\overline{TR1}$ is 0.7 m (upper radargram) and $\overline{TR2}$ is 0.84 m (lower radargram). The x -coordinate corresponds to the position of the transmitter. The first zero crossing of the groundwave is picked (red line) to determine the velocity.

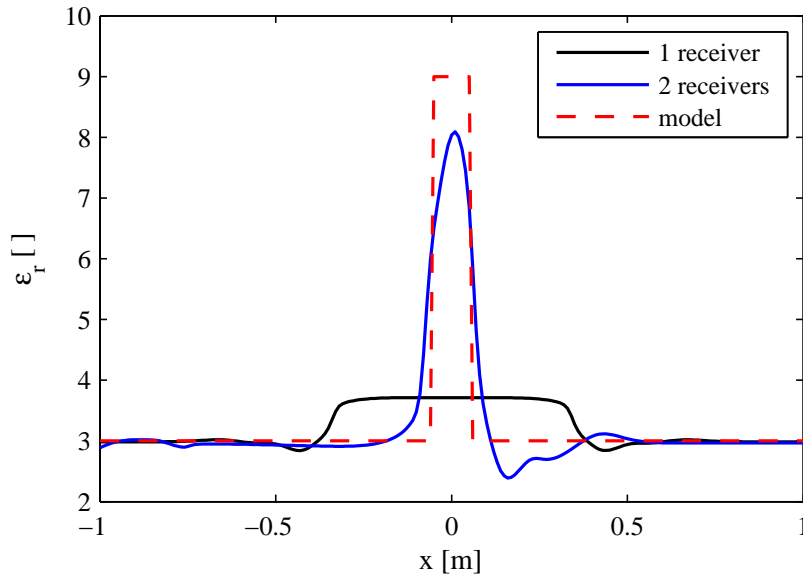


Figure 4.24: Results of FD groundwave analysis. The model is plotted in red and the permittivity distribution deduced from the simulated GPR measurement with 2 receiving antennas is in blue. The results of a classical groundwave interpretation ($T-R = 0.7$ m) is plotted in black for comparison.

the permittivity value is not completely reached. The undulation and underestimation on the right side of the anomalous zone is caused by the reflections at the sharp lateral interfaces of the anomaly which interfere with the groundwave (Fig. 4.23).

To quantify the deviation of the deduced permittivity values compared to the input model, the root mean square deviation of the data d_i and the model M_i is normalised to the mean of the model. This coefficient of deviation CD is in analogy to the coefficient of variation which relates the standard deviation to the mean:

$$CD = \frac{\sqrt{\frac{1}{N} \sum_i (d_i - M_i)^2}}{\frac{1}{N} \sum_i M_i}. \quad (4.101)$$

When comparing the anomalous zone, the RMS deviation is reduced from $CD = 0.50$ to $CD = 0.21$ when using the two receiver technique instead of the classical. The coefficient of deviation depends on the width of the zone for which the deduced permittivity values are compared to the model and this width is set to $-0.5 \text{ m} \leq x \leq 0.5 \text{ m}$ for this and the following comparisons.

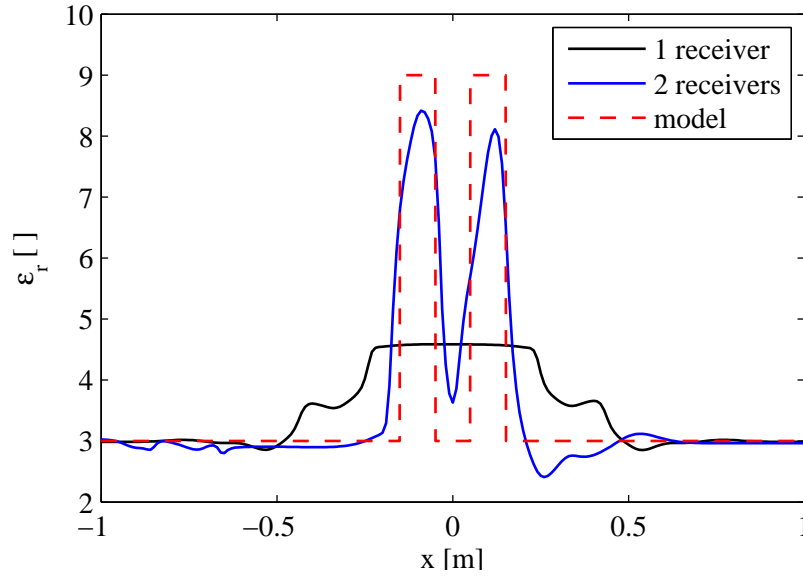


Figure 4.25: Results of FD groundwave analysis. The model is plotted in red and the permittivity distribution deduced from the simulated GPR measurement with 2 receiving antennas is in blue. The results of a classical groundwave interpretation ($T-R = 0.7$ m) is plotted in black for comparison.

The horizontal resolution corresponds to the distance between two anomalies at which they just can be distinguished. A model with 2 anomalies of 0.1 m separated by 0.1 m was used for a FD calculation. Fig. 4.25 shows the deduced permittivities using the two groundwave analysis methods. One can clearly distinguish the two anomalies when using two receiving antennas whereas there appears only one anomaly when the classical technique is used. Therefore, a horizontal resolution of at least 0.1 m can be deduced when the new technique is used. When comparing the new technique and the standard technique in the vicinity of the anomaly ($-0.5 \text{ m} < x < 0.5 \text{ m}$), the standardised root mean square deviation is reduced from $CD = 0.52$ to $CD = 0.25$.

The new layout has been experimentally tested in a sandbox. The sand was totally dry $\varepsilon_r^{sand} = 3$ and an anomaly consisting of wetted sand ($\Theta_V \approx 10\text{vol}\%$ and $\varepsilon_r^{anom} = 5.8$) which was packed in a plastic foil was buried flush with the top sandbox surface. The same measuring layout was used as in Fig. 4.22, i.e. $T-R1 = 0.35$ m and $R1-R2 = 0.14$ m and the results of the analysis is depicted in Fig. 4.26. The determined permittivities and the underground

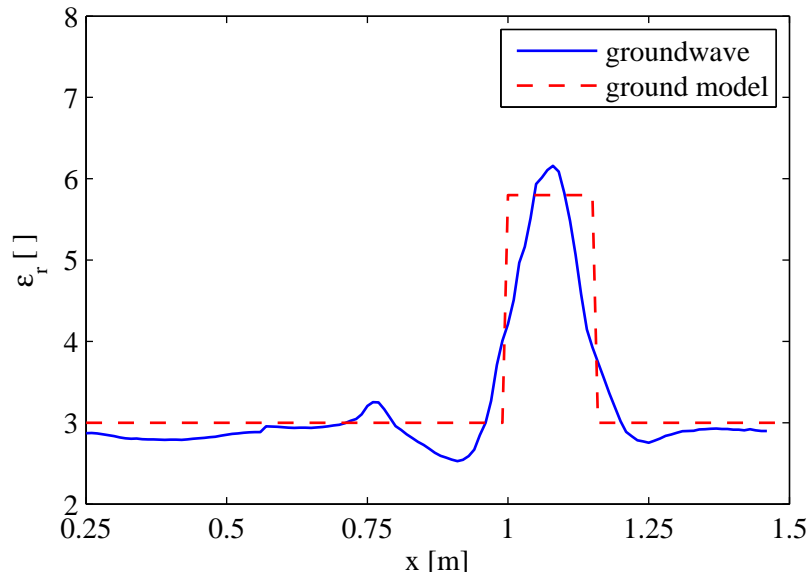


Figure 4.26: Groundwave analysis of sandbox experiment using the 2-receiver setup. A 0.15 m large anomaly of wet sand ($\epsilon_r = 5.8$) is buried in dry sand ($\epsilon_r = 3$). The result of the groundwave analysis is depicted as well as the underground model (ϵ_r -values of dry and wet sand according to TDR measurements).

model, i.e. the permittivities determined with the TDR, fit quite well. Besides the anomaly there is a small under-estimation of the permittivity of the dry sand probably caused by reflections at the sharp lateral interface of the wet sand body. This under-estimation occurs on the side of the measuring layout to which the transmitting antenna is placed. For the sandbox experiment, the T was placed towards negative x -values and for the FD calculation towards positive x -values. Thus, the effect occurs on different sides of the anomaly.

Recapitulating, when using the new technique and the setup described in Fig. 4.22, anomalies in the range of 1 decimetre can yet be resolved. The absolute values may diverge a little but the lateral boundaries of the anomaly are quite well resolved.

Figure 4.27 shows the results of a profile field measurement on location 2 at a place with nearly no vegetation as it has been treated with herbicides for soil-scientific experiments. Here again, the separation of both receivers was 0.14 m. The area 9–11 m has been irrigated before the experiment and has higher water contents and thus higher permittivities. The permittivities have

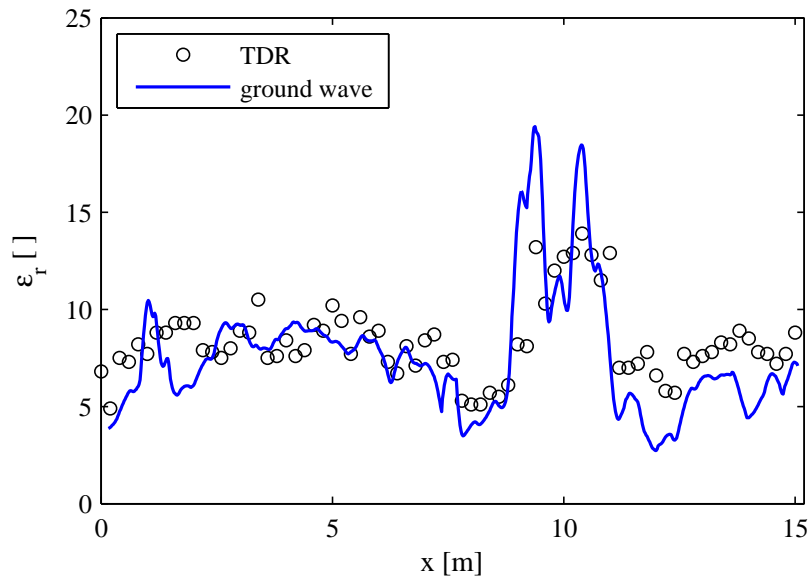


Figure 4.27: Groundwave field measurement on a sandy soil and results of TDR measurements. The area 9–11 m has been irrigated.

been determined every 0.2 m with a TDR probe for verification. Both methods feature the same principle trends but show some differences. These differences are probably caused by the elapsed time between the two measurements. After precipitation, the soil moisture is not stationary but may change due to infiltration and evaporation. Another factor is the inaccuracy of the TDR probe of $\Delta\epsilon \approx \pm 1$ plus the errors due to soil compaction and air gaps along the rods caused when inserting the probe into the soil. Furthermore, both methods feature different measuring volumes (see section 4.3.2).

Estimation of accuracy

The accuracy of the deduced velocity and thus of permittivity is determined by errors in travel path and travel time. The travel path of the groundwave is not exactly known, especially concerning the small gap between the antenna dipole and the soil. But this partition is of no relevance as only travel path differences in between both receiving antennas are regarded. The coupling to the soil is the same for both receiving antennas as they are identical in construction. This is a further advantage of the two-receiver layout compared to the classical technique. As the setup of transmitter and both receivers is fixed, the geometry will not vary during the measurement and thus changes in

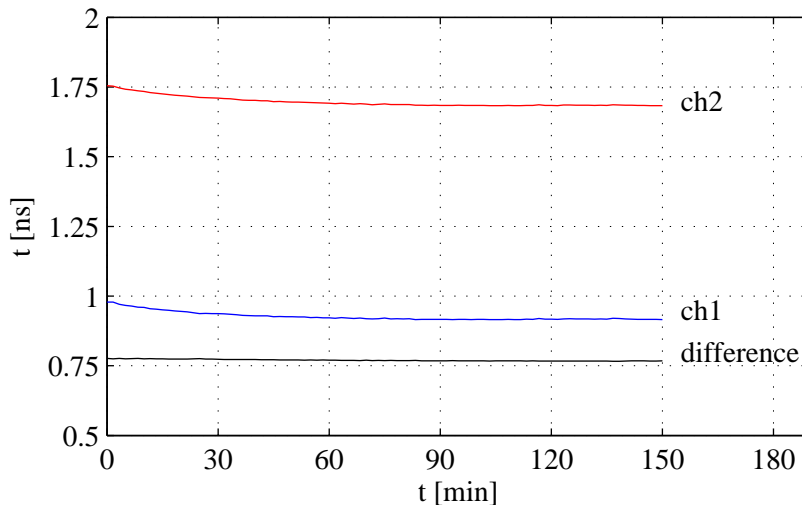


Figure 4.28: Time drift of GSSI GPR system: The transmitter was placed opposed to the two receivers and a transmission measurement was carried out during 2.5 hours. The absolute time of the two receiving channels is depicted as well as the time difference between both channels.

the travelpath length between both receivers can be excluded.

Several factors affect the measured traveltime of the groundwave. In general, a GPR device will show a drift when operated for a longer length of time due to warming up and dilatation of the electronic modules. In order to determine the drift of the used device, the transmitter was placed opposed to the two receivers and a transmission measurement was carried out during 2.5 hours. The central unit (GSSI SIR 20) was turned on for 10 minutes before starting the measurement. This corresponds approximately to the time one will need to adjust the settings before carrying out a field measurement. The travel time of the first arrival at the two receiving antennas is depicted in Fig. 4.28 as well as the difference between both channels. During the first hour, the time drift of the recording channels is at about 0.1 ns. As both channels have nearly the same drift, the time difference shows only a small drift of less than 0.01 ns during 2.5 h.

The discretisation of the data also limits the time resolution. A rate of 2048 samples/scan which still allows to collect the data at walking speed with a trace spacing of 0.02 m results in a sampling interval of approximately 0.01 ns.

The resulting error in permittivity is deduced from Eq. (4.99) to

$$\Delta\epsilon_r = \left| \frac{\partial\epsilon_r}{\partial(t_2 - t_1)} \right| \Delta(t_2 - t_1) = \frac{2c_0^2(t_2 - t_1)}{R_1 R_2^2} \Delta(t_2 - t_1). \quad (4.102)$$

When summing up the time errors to maximally 0.02 ns and presuming a velocity of 0.173 m/ns, the permittivity can be deduced to $\epsilon_r = 3 \pm 0.15$ when using the described setup. This estimated error is in good accordance with the variation of the derived permittivity in the sandbox experiment outside the anomaly, i.e. on homogeneous sand (see. Fig. 4.26, $x = 0.25\text{--}0.75$ m). Here, i.e. under ideal conditions, the deduced permittivity is $\epsilon_r = 3 \pm 0.2$. If the measurements are carried out on moist soil (for example $\epsilon_r^{\text{soil}} = 9$), the error will be $\Delta\epsilon_r = 0.26$.

One source of error hard to quantify is surface roughness, vegetation and discontinuous soil layering. The first two will influence antenna coupling and can at worst result in partial dropouts of the groundwave. This was the case on location 2 without removing the 0.2 m high grass so that no reasonable interpretation was possible. Soil layering can cause significant reflections and e.g. critically refracted waves that might interfere with the groundwave especially when non shielded antennas are used. Thus, at difficult locations a MO measurement should be carried out as well with the 2-receiver setup in order to determine an ideal antenna separation and to ensure a correct groundwave identification.

4.4.4 Spatial Field Measurements and Statistical Analysis

Location 2

The groundwave technique was applied to the same locations as the coefficient of reflection. The permittivity was determined on a 10 m \times 10 m area on a regular grid (Fig. 4.29) after removing the grass. The groundwave onsets are automatically picked with a phase follower and only corrected if the automatic tracking algorithm loses the phase or if strong reflections superpose the groundwave as is the case at some few position on the location. The spatial permittivity distribution is similar to the distribution determined with the coefficient of reflection (Fig. 4.13). Figure 4.30 shows the probability density of the permittivity distribution at location 2. The experimental data resembles quite well a normal distribution. The mean and standard deviation of the permittivity is $\epsilon_r = 5.3 \pm 0.85$.

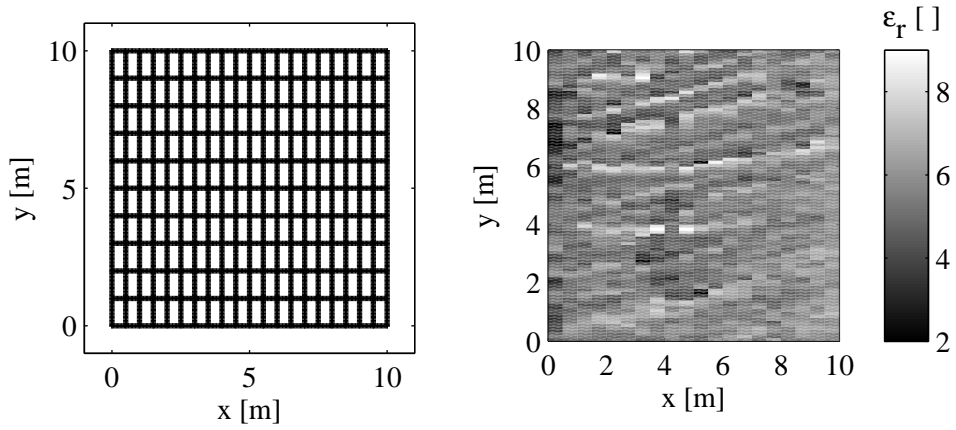


Figure 4.29: Measuring grid (left) and deduced permittivities from the groundwave of the profiles in y -direction without vegetation (right).

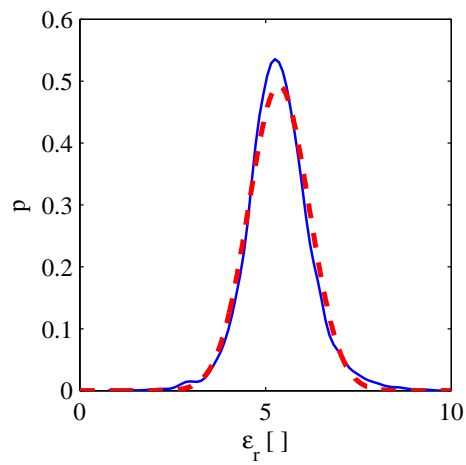


Figure 4.30: Statistical analysis of the permittivity distribution determined with the groundwave at location 2. Experimental probability density function (blue solid) and normal distribution (red dashed) with the same mean and standard deviation as in situ for comparison: $\epsilon_r = 5.3 \pm 0.85$.

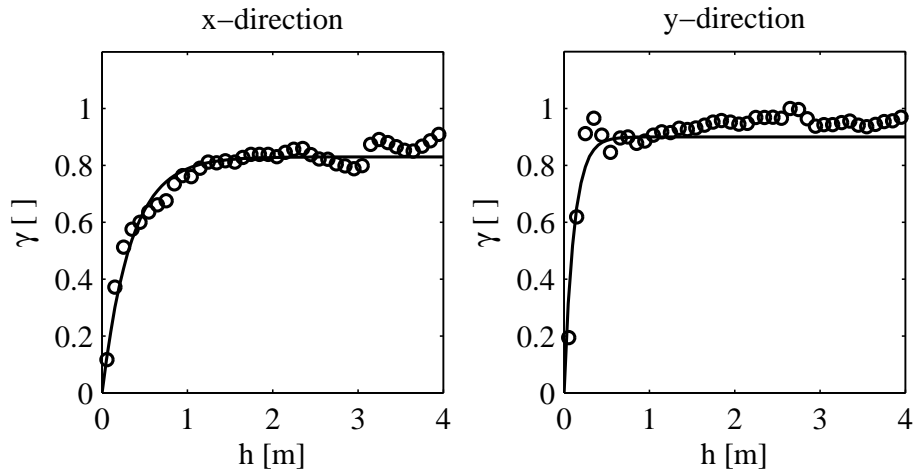


Figure 4.31: Statistical analysis of the permittivity distribution determined with the groundwave at location 2. The directional variogram is calculated in x - and y -direction and an exponential model is fitted to the curves. The range of the fitted models is: $a_x = 1.0$ m and $a_y = 0.3$ m.

Due to the structure of the spatial permittivity distribution already mentioned in the last section, the directional variogram in x - and y -direction is calculated and depicted in Fig. 4.31. The variogram in x -direction ($a_x = 1.0$ m) differs significantly from the variogram in y -direction ($a_y = 0.3$ m). Here again, the direction of the anisotropy is set to the direction of the structure (15°) and an anisotropic variogram is fitted to the data with an anisotropy factor of $\lambda = a_{max}/a_{min} \approx 4.5$.

The directional variogram is used for kriging the data to a grid spacing of 0.1 m (Fig. 4.32 top). The spatial permittivity distribution determined with the groundwave shows the same parallel structure as the reflection mode (Fig. 4.32 bottom). This structure is probably caused by the former cultivation of the area as discussed in section 4.3. The parallel lines at $y = 4$ m and 6 m which can also be observed in this data might be explained as the trace of a vehicle.

Location 3

The groundwave technique was applied to location 3 after removing the vegetation. Figure 4.33 shows the statistical analysis of the permittivity distribution. The experimental probability density function has a positive skewness. To the right of Fig. 4.33 the experimental PDF of the logarithm of the relative permittivity is depicted. The normal distribution now fits the data quite well signifi-

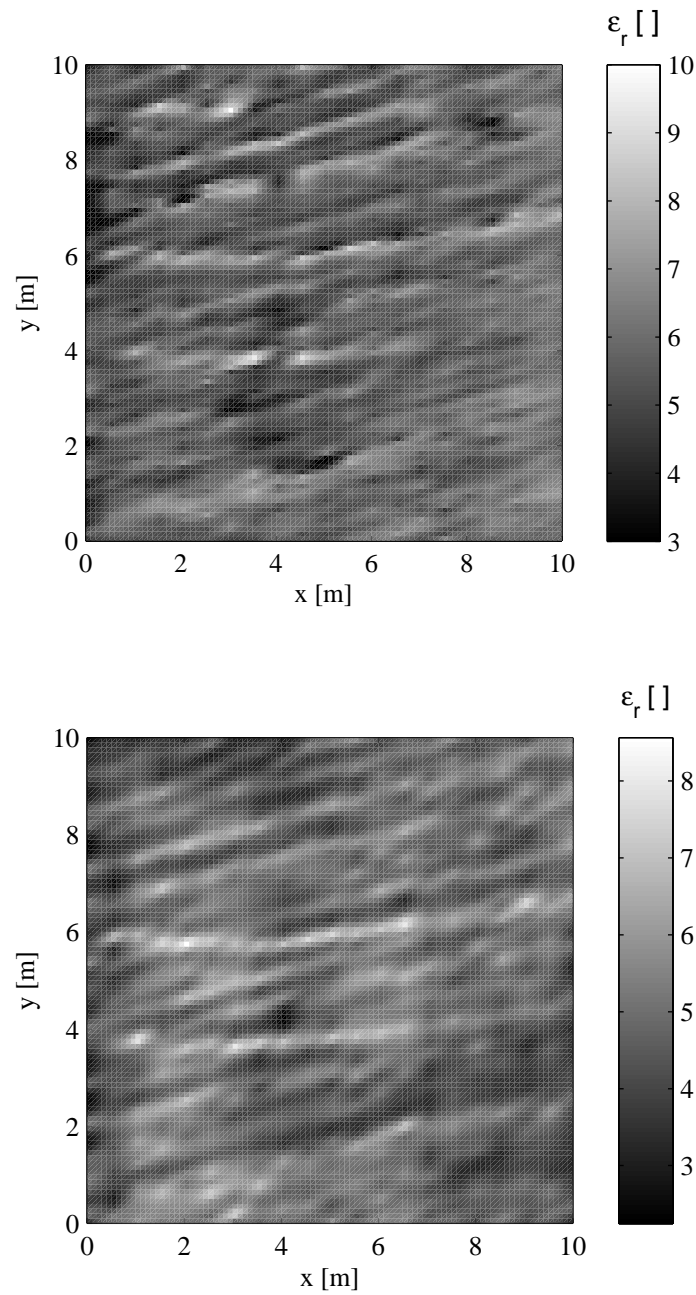


Figure 4.32: top: 2D distribution of the permittivity at location 2 derived with the groundwave. The data are grided with 0.1 m increment by kriging using the isotropic variogram model of Fig. 4.31. bottom: Permittivity distribution deduced from the coefficient of reflection for comparison (Fig. 4.16).

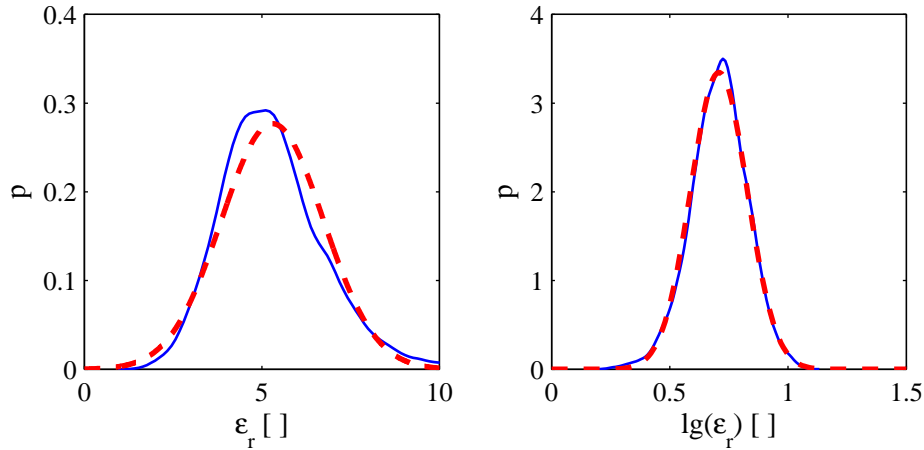


Figure 4.33: Statistical analysis of the permittivity distribution determined with the groundwave at location 3. Experimental probability density function (blue solid) and normal distribution (red dashed) with the same mean and standard deviation as in situ for comparison. Left side, relative permittivity: $\epsilon_r = 5.3 \pm 1.4$. Right side, logarithm of permittivity: $lg(\epsilon_r) = 0.71 \pm 0.12$.

fying that the permittivity is log-normal distributed with $lg(\epsilon_r) = 0.71 \pm 0.12$.

Fig. 4.34 shows the variogram of the spatial permittivity distribution. The directional semivariograms in x - and y -direction do not differ what indicates an isotropic distribution. Therefore, the omnidirectional variogram is depicted. An exponential model function is fitted to the experimental data yielding a range of $a = 0.35$ m. As the first rise of the variogram is not determined due to the resolution limit of the method, other models might also fit the experimental data, e.g. a Gaussian model including a nugget effect. However, the model that is used is the simplest which describes the data and therefore is to be preferred.

The data are gridded by a kriging algorithm using the variogram model of Fig. 4.34 and are plotted in Fig. 4.35. The spatial permittivity distribution shows no directionality and a small correlation length.

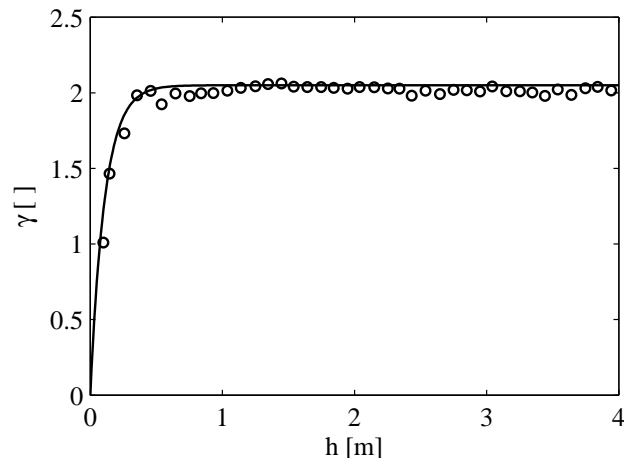


Figure 4.34: Statistical analysis of the permittivity distribution determined with the groundwave at location 3. Omnidirectional experimental variogram and fitted exponential model with range $a = 0.35$ m.

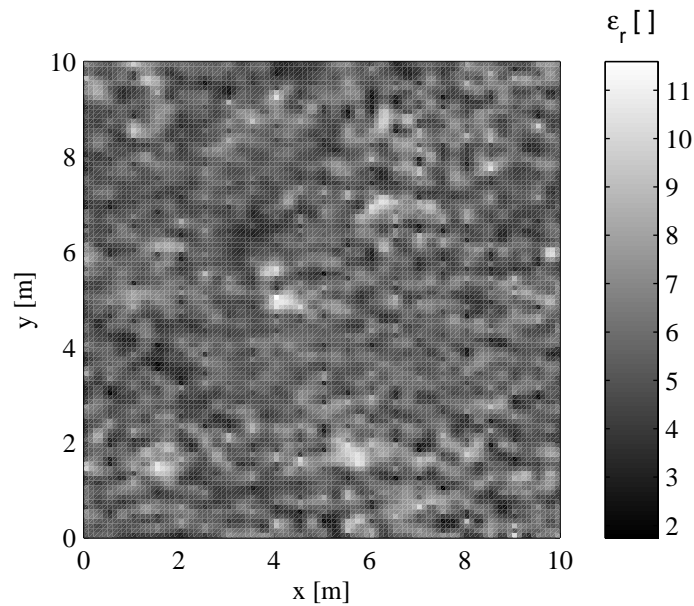


Figure 4.35: 2D distribution of the permittivity derived with the groundwave. The data are gridded with 0.1 m increment by kriging using the isotropic variogram model of Fig. 4.34.

5 Influence of Soil Variability on Geophysical measurements

In this chapter, FD calculations are carried out using random models based on the statistical parameters of the physical properties which are determined in chapters 3 and 4. For several reasons the variograms were calculated only in lateral direction but not in vertical:

- Both GPR techniques only provide a 2D permittivity distribution.
- In most cases, there is a pronounced difference between the physical properties of the humus rich topsoil and the subsoil. As the topsoil is commonly restricted to approximately the first 0.3 m, only a correlation length up to 0.15 m can be determined in vertical direction (see chapter 2).
- Anisotropy in the physical properties distribution is not likely to occur in the topsoil as the upper horizon is homogenised due to ploughing, soil freezing and biological activity. The roots of grass, which are mostly restricted to the topsoil, compensate vertical gradients in soil moisture which might be caused by evaporation.

Thus, an anisotropic distribution of physical properties is, if at all, caused by different soil layers but is not likely to occur in the topsoil. In the following, an isotropic distribution is assumed when generating the FD models. If physical properties were distributed anisotropically, they could easily be implemented in geostatistical simulations.

5.1 Influence of Conductivity Variations on DC Measurements

5.1.1 Accuracy of Dipole-Dipole Measurements to Determine Statistical Properties

In the following will be discussed whether the 2D dipole-dipole configurations used in section 3.3.2 are suitable for determining the statistical properties of conductivity distribution in soil. The key questions are:

- Can a 3D heterogeneous conductivity distribution be adequately determined by only 2D measurements?
- Is the probability density function adequately reproduced?
- Is the correlation length adequately reproduced?

The measurements are simulated on a 3D synthetic heterogeneous medium using a 3D FD calculation (Günther, 2004). Figure 5.1 shows the resistivity distribution of a model as well as the position of the electrodes. The discretisation of the model is 0.05 m. A log-normal distribution function ($\lg(\rho/\Omega\text{m}) = 3.2 \pm 0.16$) was used to simulate the random medias which is in good accordance with the resistivities derived in situ (section 3.3.2). An exponential variogram function with range $a = 0.2, 0.5$ and 2.0 m was used representing the whole span of correlation length which was regarded in the previous chapters. A margin consisting of two regular and four prolonged cells featuring the mean resistivity ($10^{3.2} = 1585 \Omega\text{m}$) was appended to the model boundaries.

First, a 2D dipole-dipole measurement parallel to the x -axis was simulated at $y = 0$ m. The electrodes were placed from $x = -0.5$ m up to 10.5 m using a spacing of 0.1 m (Fig. 5.1 central electrode line). The dipole-dipole configurations up to the tenth separation were calculated and used as synthetic data for further analysis after adding 3% random noise.

In addition, four further electrode lines were placed at $y = \pm 0.1$ and ± 0.2 m. The radial dipoles up to the tenth separation were simulated as above resulting in a 3D dipole-dipole measurement using 5 parallel electrode lines (Fig. 5.1).

The data of the single line and the data of the five lines were inverted using a 2D and a 3D Gauss-Newton algorithm with smoothness constraints, respectively

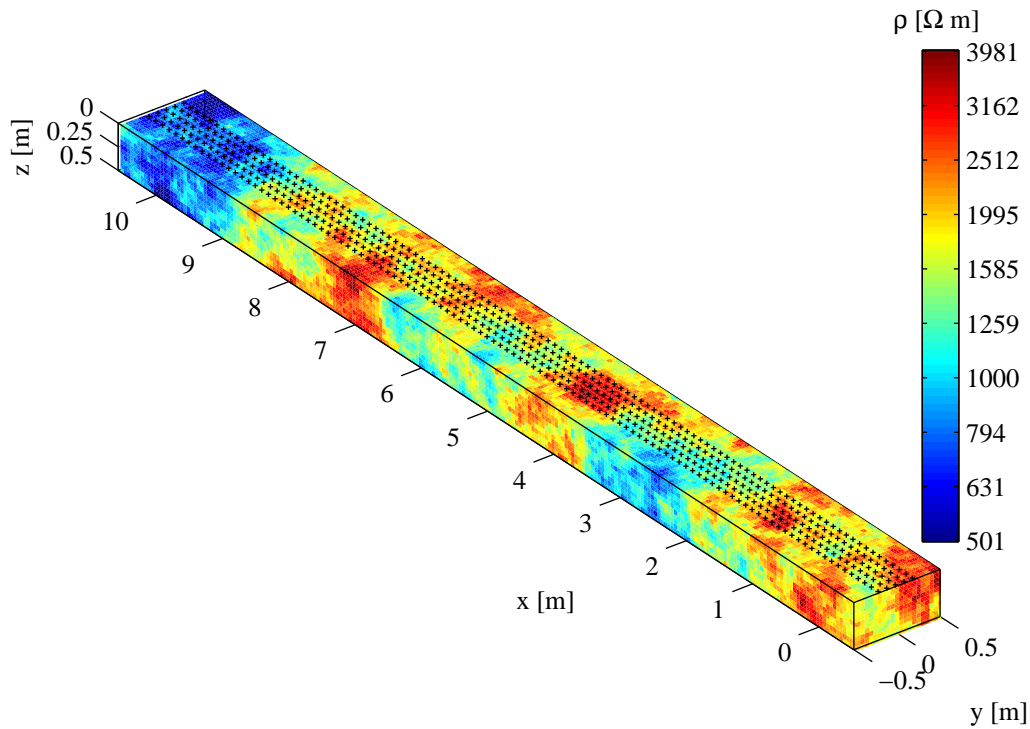


Figure 5.1: 3D model of resistivity distribution and position of electrodes used to simulate 3D and 2D dipole-dipole measurements. A log-normal distribution with $\lg(\rho/\Omega\text{m}) = 3.2 \pm 0.16$ and an exponential variogram function with range $a = 2$ m was used to generate the random medium.

(Günther, 2004). The discretisation was the same as for the model generation (0.05 m) and the regularisation parameter was determined by means of minimal χ^2 -deviations between original and fitted data (Eq. 3.21).

In case of the larger correlation length of 2 m, the fit of the 3D model is as good as resulting in a relative root-mean square data deviation of $\text{RRMS} = 3.1\%$. This corresponds almost perfectly to the random noise of 3% which was added to the simulated measurements. The fit of the 2D model is not as accurate because the 3D structures affecting the measurements cannot be completely explained by a 2D model. This yields a RRMS data error of 7% which is quite a good result and comparable to 2D field-data inversions.

Regarding the medium correlation length ($a = 0.5$ m), the fit was not as accurate and results in RRMS of approximately 3.3% for the 3D inversion and 6.5% for the 2D inversion. In case of $a = 0.2$ m correlation length, the RRMS of the 3D and 2D inversion was 3.5% and 14%. The smaller the correlation length, the more 3D effects influence the 2D measurements. The degree of freedom of the 2D model is smaller than for the 3D model and thus the data influenced by 3D structures cannot be adequately described. When correlation length is large, there is few resistivity variation in the sensitivity range of the measuring configuration. The smaller the correlation length, the more different resistivity values are captured by the configuration which have to be explained by the model. A 3D model features enough degrees of freedom which can be adapted and thus the data are well reproduced even in case of a highly variable underground.

A slice at $y = 0$ m was extracted from the original 3D model and the 3D inverted model in order to compare them to the 2D inverted model (Fig. 5.2, 5.3 and 5.4). The 3D and 2D inversions both reproduce the principle near-surface structures of the input models. The 3D model shows quite good consistence in deeper regions for the model with larger correlation length ($a = 2$ m) whereas the 2D model shows deviations for depths deeper than 0.3 m (Fig. 5.2). The smaller the correlation length of the original model, the worse are the variabilities reproduced in deeper regions. This is an effect of decreasing resolution with depth. The coverage of the lower model layers is rather bad when restricting to dipole separations of 1.0 m. The effect is stronger for the 2D inversion than for the 3D inversion. In Fig. 5.3 ($a = 0.5$ m), structures deeper than 0.25 m are not reproduced by the 2D inversion, whereas the 3D model shows nameable deviations only in deep regions. Regarding the results when correlation length is small ($a = 0.2$ m) only the very top layers of the original model are reproduced by the DC inversions (Fig. 5.4). This are the first 0.25 m for the 3D model and 0.1 m for the 2D model, respectively.

In the following, only the upper 0.25 m of the models are statistically analysed which is in accordance with the interpretation of the field data in section 3.3.2. The beginning and the end of the profile have also been removed because they may be affected by boundary effects, i.e. the area $0 \text{ m} \leq x \leq 10 \text{ m}$ and $0 \text{ m} \leq z \leq 0.25 \text{ m}$ is analysed. The probability density function as well as the directional variogram in x -direction are depicted in Fig. 5.5. The standardised semivariance γ_{std} , i.e. the semivariance divided by the variance, is plotted for better comparison of the different models as they show different standard deviations.

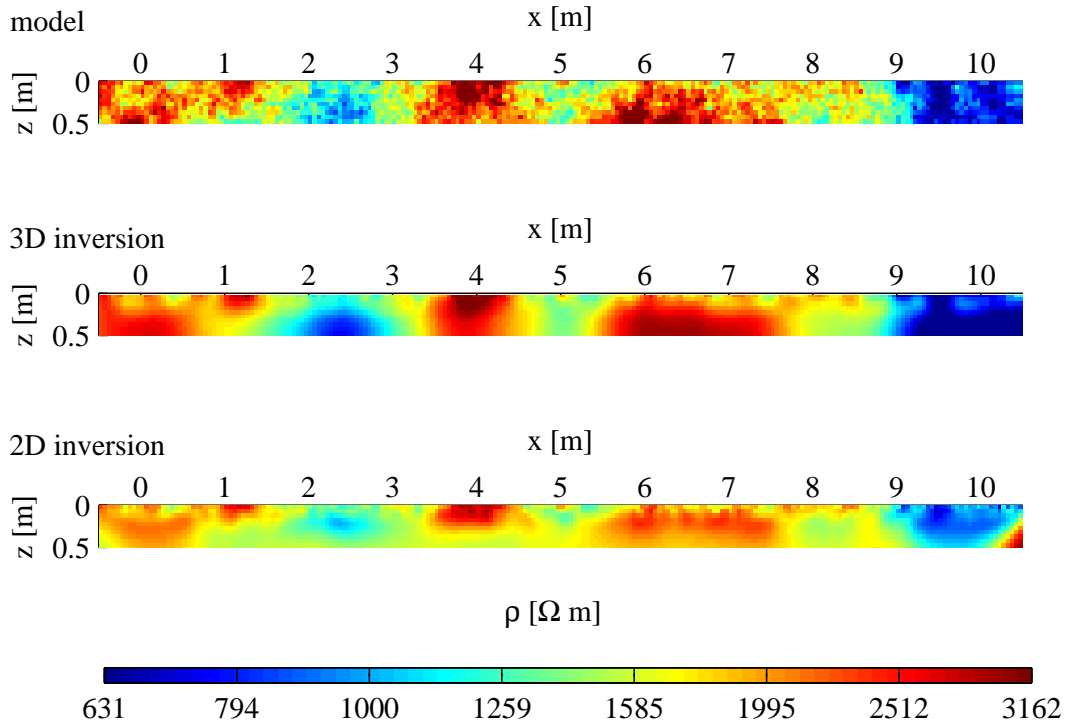


Figure 5.2: Comparison of 2D and 3D measurement on a heterogeneous medium with range $a = 2$ m. Section at $y = 0$ m through the 3D model used to simulate the measurement (see Fig. 5.1), section through the inverted model of the 3D data, inverted model of the 2D data.

In case of large correlation length ($a = 2$ m), there is a misfit of the input random model to the statistical input functions due to ergodic fluctuations (see chapter 2) which are caused by the relative large correlation length compared to the model dimensions. The probability density function as well as the variogram of the input random model are well reproduced by the inverted DC measurements (Fig. 5.5 a). This holds true especially for the 3D measurement but also the 2D measurement shows only little deviation in the probability density function.

In case of shorter correlation lengths, the input random model fits the statistical input function quite accurately. The variograms of the 2D and 3D inverted measurements show good accordance with the variogram of the input model and the range is only slightly underestimated by the DC measurements. In contrast, the probability density function shows some discrepancy (Fig. 5.5 b and c). The standard deviation is smaller for the DC inversion model than

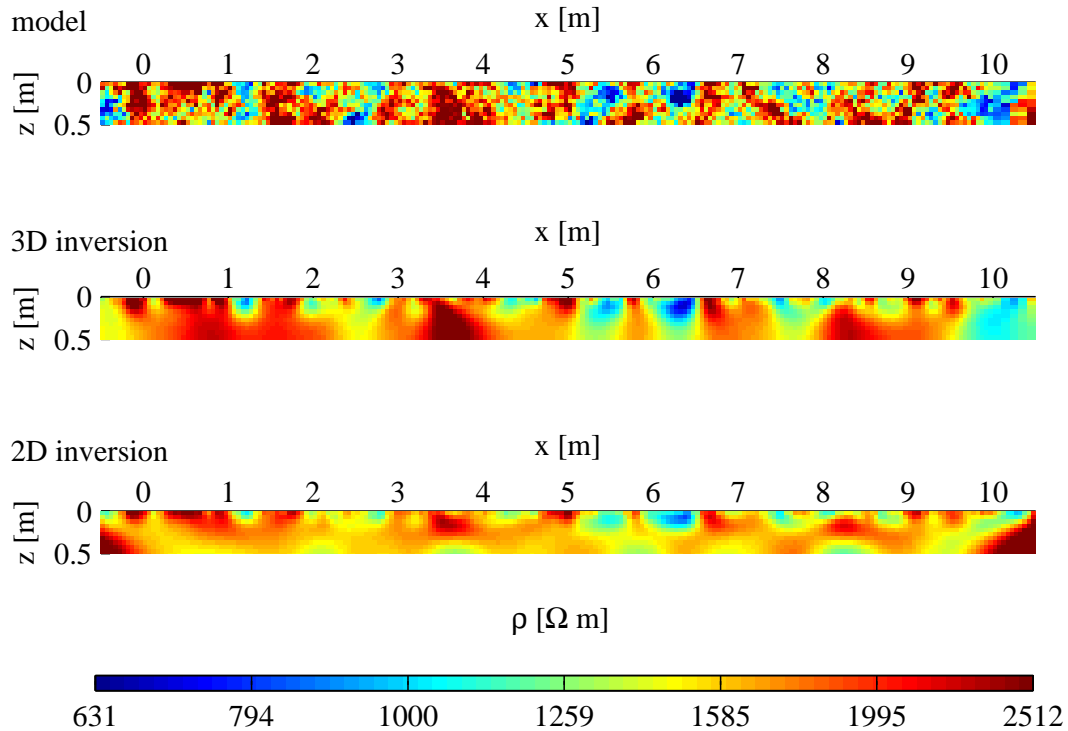


Figure 5.3: Comparison of 2D and 3D measurement on a heterogeneous medium with range $a = 0.5$ m. Section at $y = 0$ m through the 3D model used to simulate the measurement, section through the inverted model of the 3D data, inverted model of the 2D data.

for the input model. This effect is stronger for the 2D measurement than the 3D measurement and increases with decreasing correlation length. In case of the shortest correlation length ($a = 0.2$ m) the standard deviation of the logarithms of resistivity are underestimated by more than 50%. However, the mean as well as the shape of the distribution is reproduced. Thus, it can be determined whether the original distribution is symmetric or not. The measuring layout or the inversion algorithm or both act as a filter diminishing the spread of the conductivity distribution but conserving the spatial pattern.

Recapitulating, the spatial distribution of conductivity can be determined accurately by either a 3D or a 2D measurement. The used dipole-dipole setups reproduce the variogram of the true topsoil conductivity distribution very well in a large range of correlation lengths. The variability is underestimated by the DC measurements for short correlation length pretending smaller standard

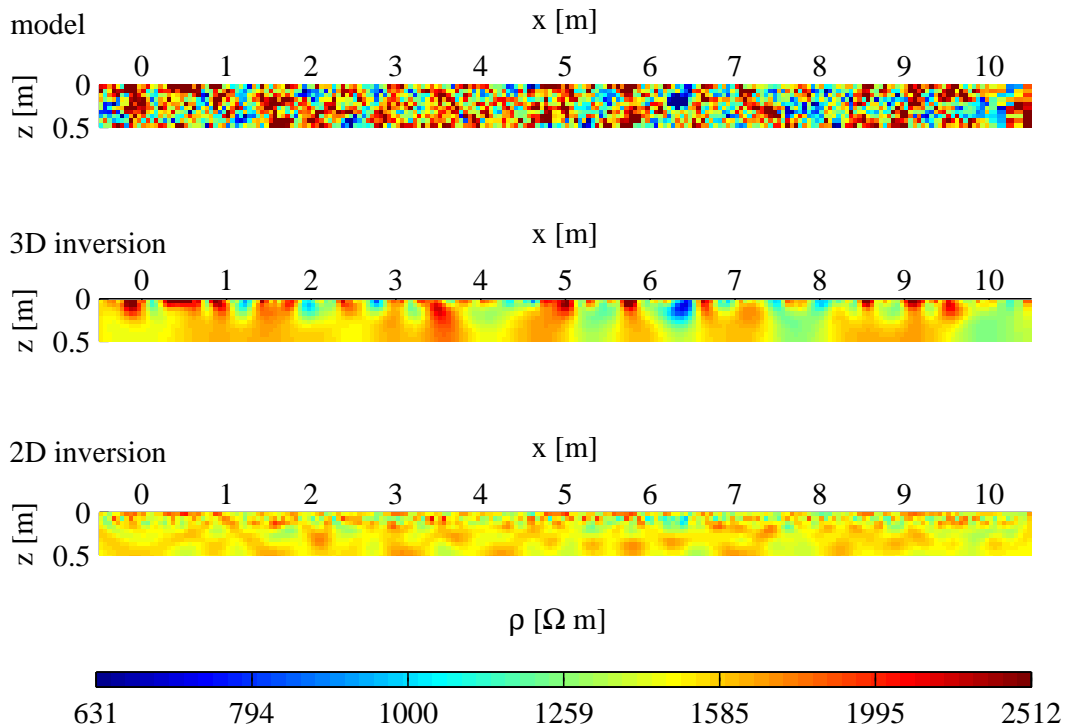


Figure 5.4: Comparison of 2D and 3D measurement on a heterogeneous medium with range $a = 0.2$ m. Section at $y = 0$ m through the 3D model used to simulate the measurement, section through the inverted model of the 3D data, inverted model of the 2D data.

deviations. Therefore, variability of conductivity is probably underestimated in section 3.3.2 but the mean and the shape of the probability density function is still correctly determined.

5.1.2 Influence on Resistivity Soundings

The effect of soil heterogeneity on geoelectrical measurements is exemplarily demonstrated and analysed for Schlumberger soundings. The small-scale variability of the topsoil usually cannot be resolved by Schlumberger layouts and causes fluctuations in the measured curves and inverted layers.

The used models consist of three layers featuring resistivities of $\rho = 1300, 100$ and $1300 \Omega\text{m}$. A 4 m wide cutout of the homogeneously layered basic model is plotted to the left of Fig. 5.6. The basic model was varied by inserting a

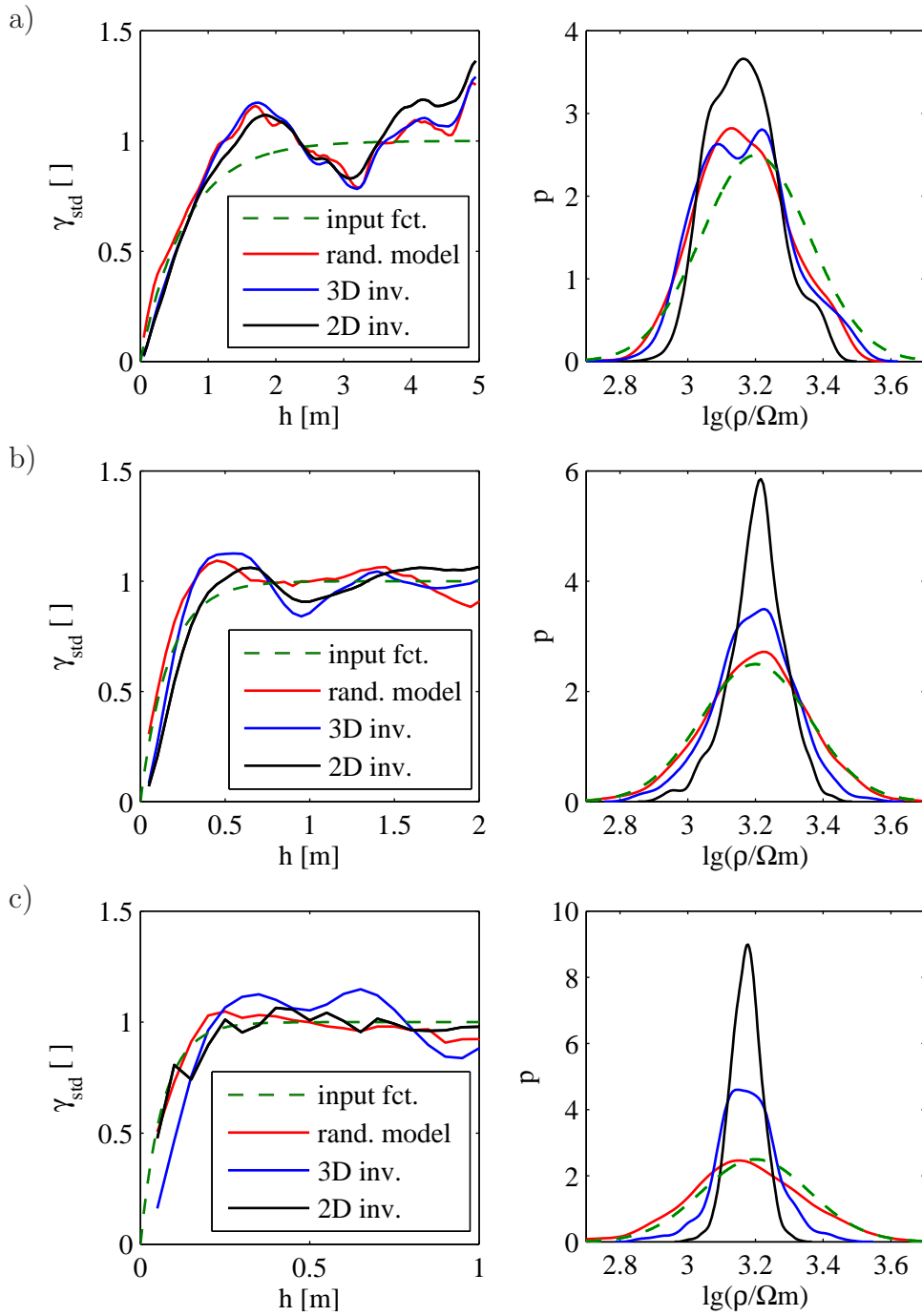


Figure 5.5: Statistical analysis of the upper part ($0 \leq z \leq 0.25$ m) of the model used for the forward calculation and the 3D and 2D inverted models. Standardised directional variogram in x -direction (left) and probability density function (right). a: range $a = 2$ m, Fig. 5.2; b: range $a = 0.5$ m, Fig. 5.3; c: range $a = 0.2$ m, Fig. 5.4. Note the different scale of the variogram h -axis.

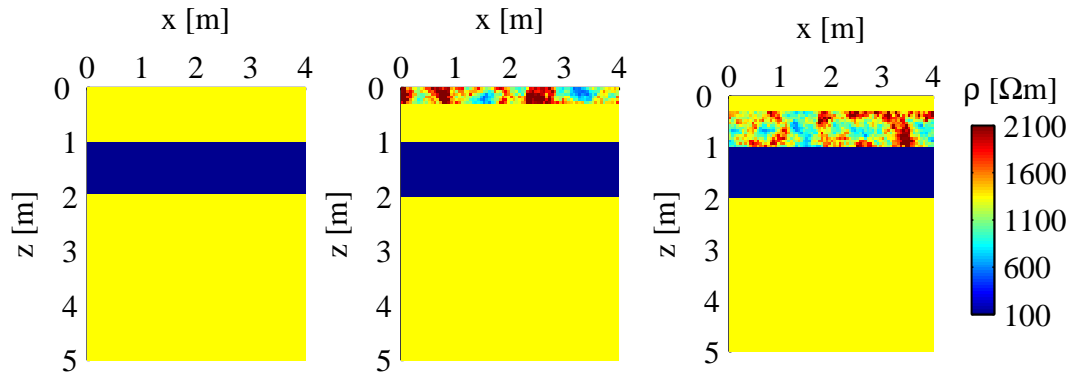


Figure 5.6: Models used for the FD calculations to simulate Schlumberger soundings. Only a cutout of the 21 m large 2D model is depicted for better illustration. Homogeneously layered model with $\rho = 1300/100/1300 \Omega\text{m}$ (left side), model with heterogeneous topsoil (0–0.3 m) (centre) and heterogeneous subsoil (0.3–1.0 m) (right side). The statistical parameters of the heterogeneous soil layers are: $\lg(\rho/\Omega\text{m}) = 3.1 \pm 0.15$, exponential variogram model with range $a = 0.4 \text{ m}$.

heterogeneous topsoil from $z = 0\text{--}0.3 \text{ m}$ (Fig. 5.6, centre) or a heterogeneous subsoil from $z = 0.3\text{--}1.0 \text{ m}$ (Fig. 5.6, to the right). A log-normal distribution function ($\lg(\rho/\Omega\text{m}) = 3.1 \pm 0.15$) and an exponential variogram function with range $a = 0.4 \text{ m}$ was used to simulate the random medium. These parameters are in good accordance with the parameters deduced in situ on location 1 (section 3.3.2). Ten different realisations of the heterogeneous models were simulated. A Schlumberger sounding was calculated for each realisation yielding a set of 10 differing sounding curves per model. The potential electrodes (M, N) were fixed at $x = \pm 0.1 \text{ m}$ and the current electrodes (A, B) were moved from $x = \pm 0.2 \text{ m}$ to $x = \pm 10 \text{ m}$ in 0.1 m steps.

Figure 5.7 shows the resulting sounding curves for the homogeneously layered basic model and the models with heterogeneous topsoil. The apparent resistivities corresponding to the 10 statistical realisations are scattered above and below the data of the basic model.

A 1D Marquart-type inversion (Marquardt, 1963) was applied to the data yielding a resistivity-depth model whereby the number of layers was fixed to three as a priori information. The fitted models are plotted in the centre of Fig. 5.7. The lower boundary of the second layer and the resistivity of the third layer is not reproduced very accurately. The fit would be better if data with larger electrode separations ($AB/2 \geq 60 \text{ m}$) were available describing the

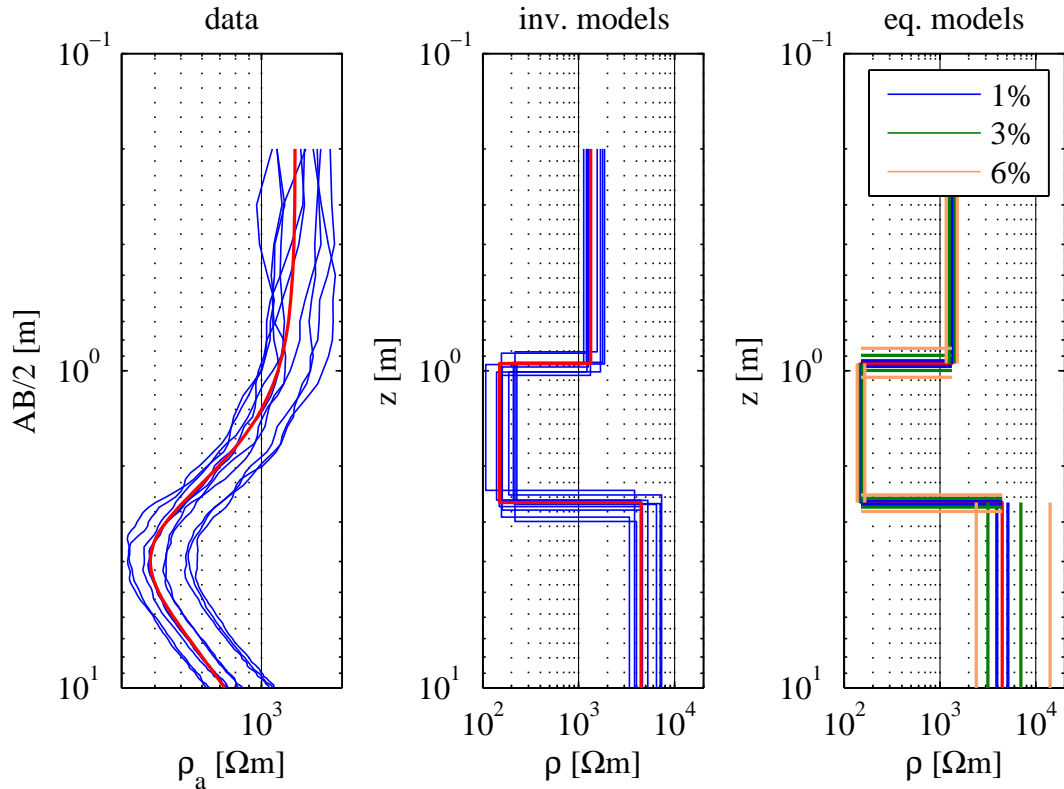


Figure 5.7: FD simulated Schlumberger soundings on heterogeneous topsoil: simulated data (left side), inverted models (centre), equivalent models assuming a data noise of 1, 3 and 6% (right side). The red lines are the data corresponding to the homogeneous model (Fig. 5.6 left side) and the blue lines correspond to the 10 realisations of the heterogeneous model (Fig. 5.6 centre).

asymptotic convergence of the apparent resistivity towards the true resistivity of the lower layer. This large separation would be needed due to the high contrast between the layers (1300 Ωm vs. 100 Ωm). But the calculation of such data requires large memory and long calculation times due to the fine discretisation of 0.05 m needed to calculate the influence of the near-surface heterogeneities correctly. Alternatively, one could use a larger grid spacing for the lower model parts and a grid refinement of the upper soil layers featuring the small-scale heterogeneities. Then, larger models can be calculated and the resistivity plateau of the lowest layer will be reached.

Nevertheless, the variations of the inverted models can be analysed as is the case for Schlumberger measurements in the field, where the resistivity plateau

of the lowest layer is frequently not completely reached due to a lack of very large layouts. In analogy to the simulated data, the 10 inverted models corresponding to the heterogeneous topsoil scatter around the basic homogeneously layered model. The used statistical parameters of the heterogeneous resistivity distribution can be assumed as typical values for sandy soils. At such locations, DC Schlumberger soundings can only determine the underground electrical properties inside the range of the scattered curves of Fig. 5.7, centre. Even though the basic model features a high contrast in resistivity of more than one decade, the variations caused by realistic topsoil heterogeneities cause considerable scatter yielding significant deviations of the inverted models. If the resistivity contrast is lower, the effect of soil heterogeneity will be larger.

To the right of Fig. 5.7, the equivalent models associated with the homogeneously layered model are plotted assuming a data noise of 1, 3 and 6%. The equivalent models correspond to the range in which the fitted models explain the data varying inside the given noise and were determined by analysis of parameter variation, i.e. resistivity and thickness of the layers. The estimation of data error is crucial for the significance of the equivalent models. Typically, the statistical errors of the measuring device are $\leq 1\%$ resulting in low deviations of the equivalent models. The other sources of errors, e.g. discrepancies in electrode position and soil heterogeneity, are often supposed to sum up to approximately 3%. However, as can be seen in Fig. 5.7, topsoil heterogeneity yields higher fluctuations of the models than the equivalent models indicate when assuming 3% data error. An error of 6% leads to a range of equivalent models comparable to the overall fluctuations caused by the heterogeneities. When having a more precise look, the uncertainty in resistivity and boundary depth described by the equivalent models strongly depends on the regarded layer whereas the uncertainty described by the 10 statistical realisations does only weakly. Topsoil variability seems to evoke a comparable uncertainty on all layers of the inverted model.

In Fig. 5.8, the sounding curves corresponding to the heterogeneous subsoil models are depicted. Even though in the used model the subsoil is more than twice as thick as the topsoil, the effects of heterogeneous subsoil is minor compared to the effect of heterogeneous topsoil. This is a result of the higher sensitivity of the measurement configuration in the near-surface area than in deeper areas. A heterogeneous subsoil evokes uncertainties which can be compared to the range of equivalent models when approximately 2% data error is assumed.

Recapitulating, it is not the measuring accuracy of the device of typically 1%

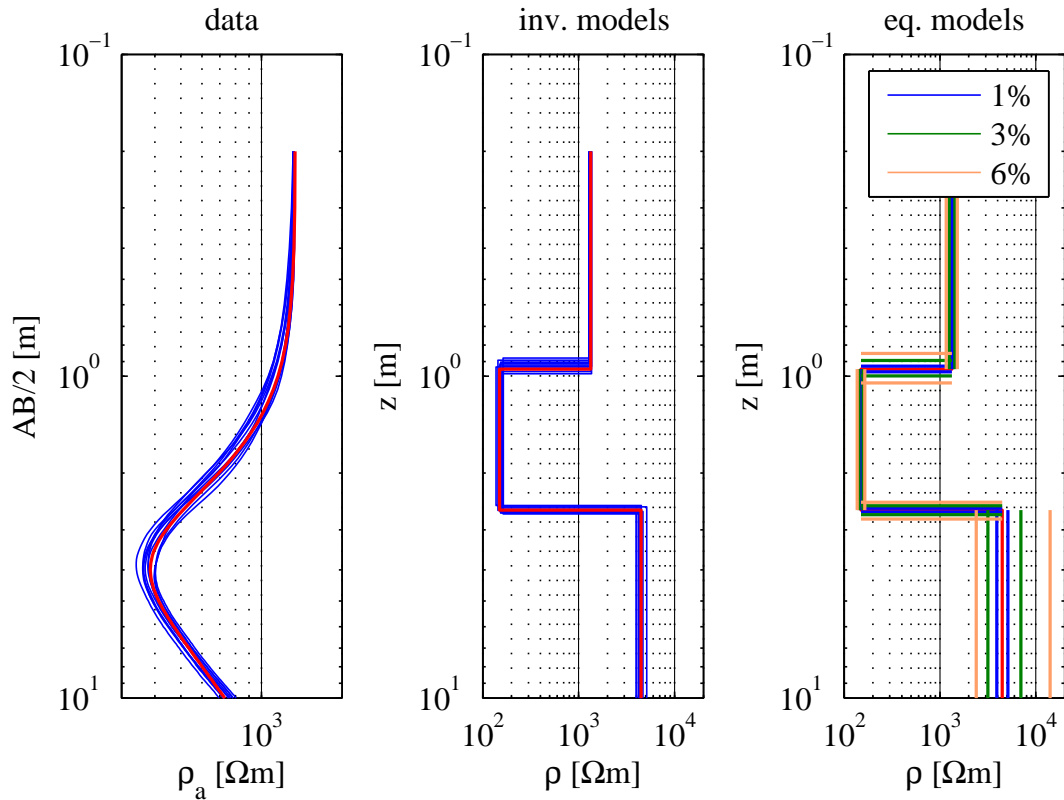


Figure 5.8: FD simulated Schlumberger soundings on heterogeneous subsoil: simulated data (left side), inverted models (centre), equivalent models assuming a data noise of 1, 3 and 6% (right side). The red lines are the data corresponding to the homogeneous model (Fig. 5.6 left side) and the blue lines correspond to the 10 realisations of the heterogeneous model (Fig. 5.6 right side).

which restricts the resolution of resistivity soundings in most cases but the influence of soil heterogeneity. The influence of topsoil (0–0.3 m) variability is much higher than the effect of subsoil (0.3–1.0 m) variability. Typical topsoil heterogeneity as determined on a sandy soil in section 3.3.2 yield variances of the inverted models comparable to the range of equivalent models corresponding to approximately 6% RMS error of the data. As the variability of conductivity is to some extent underestimated by the high-resolution dipole-dipole measurements used to determine soil variability in situ (see subsection 5.1.1), heterogeneity and thus the variances of Schlumberger soundings might even be stronger.

The absolute errors of the inverted models depend on the analysed basic model, i.e. the depth of the interfaces as well as the resistivity contrasts. Thus, models corresponding to the expected or determined subsurface structures should be used to simulate fluctuations caused by topsoil resistivity variability in order to get realistic ranges of uncertainty. These studies can be carried out prior to a field campaign to analyse whether a structure can be resolved or not when using a specific setup. Furthermore, uncertainties determined by FD calculations can be used for resolution analysis, e.g. to calculate equivalent models for 1D inversions of Schlumberger soundings as shown above or to perform a resolution analysis for 2D/3D inversions as described by Friedel (2003).

5.2 Influence of Conductivity and Permittivity Variations on GPR Measurements

5.2.1 Accuracy of Groundwave Measurements to Determine Statistical Properties

The high lateral resolution of the groundwave technique using two receivers has been demonstrated in section 4.4. In order to demonstrate the ability of this method to determine the statistical parameters correctly, a groundwave measurement is simulated on a heterogeneous soil. 3D FD simulations of electromagnetic wave propagation on personal computers are restricted to relatively small areas of typically $1\text{ m} \times 1\text{ m} \times 1\text{ m}$ due to the fine discretisation which is needed when using higher frequencies (typically 0.01 m for 500 MHz). These small areas are not suited for geostatistical analysis wherefore a 2D simulation was calculated simulating a measurement on a 10 m profile. When carrying out groundwave measurements and when a 3D distribution is present, the determined permittivity will represent the area defined by the width of the antennas and the distance between transmitter and receiver (Sperl, 1999) or the two receivers when using the improved technique. This 3D effect might influence the determination of correlation length smaller than the antenna width, which is approximately 0.2 m for the used 400 MHz antennas, but will only weakly distort the determination of larger correlation lengths. The influence of antenna width is an effect difficult to determine in practice.

A cutout of the used model is depicted in Fig. 5.9. The permeability and

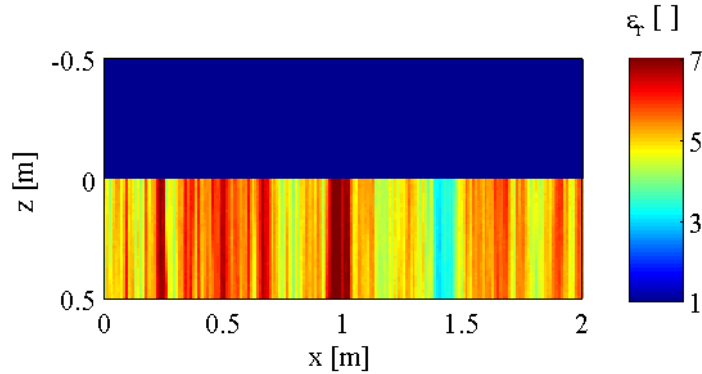


Figure 5.9: Cutout of the model used to simulate groundwave measurements on heterogeneous soil: $-0.5 \text{ m} \leq z \leq 0 \text{ m}$: air, $0 \text{ m} \leq z \leq 0.5 \text{ m}$: soil. The permittivity distribution is depicted ($\varepsilon_r = 5 \pm 1$, range $a_x = 0.3 \text{ m}$). The permeability and conductivity are constant ($\mu_r = 1$, $\sigma = 0 \text{ S/m}$).

conductivity of the soil is constant whereas the permittivity is variable. The permittivity corresponds to a slightly moist soil featuring a normal distributed permittivity as determined in chapter 4 ($\varepsilon_r = 5 \pm 1$). The correlation length in x -direction is 0.3 m . The dielectric properties do not vary in z -direction as only lateral variations are mapped with the groundwave technique. Vertical variations of the physical properties cause reflections which interfere with the groundwave to some extent and may cause difficulties when picking groundwave traveltimes if heterogeneity is high.

A FD simulation was calculated using the 2-receiver setup with a receiver distance of 0.14 m (see Fig. 4.23). The resulting radargrams of both receivers are plotted in Fig. 5.10. The groundwave shows undulations caused by the heterogeneity of the permittivity distribution. The time differences between the groundwaves of both radargrams stand for the permittivity of the soil between both receivers.

The traveltimes of the groundwaves were picked and transformed into permittivity values. The experimental density function fits the density function of the input model quite well (5.11). The directional variograms were calculated along the x -axis and the variogram of the groundwave data and the model show comparable correlation lengths of 0.3 m . Thus, the new groundwave technique is suited to determine accurately the statistical parameters of permittivity distribution even for a small correlation length of 0.3 m .

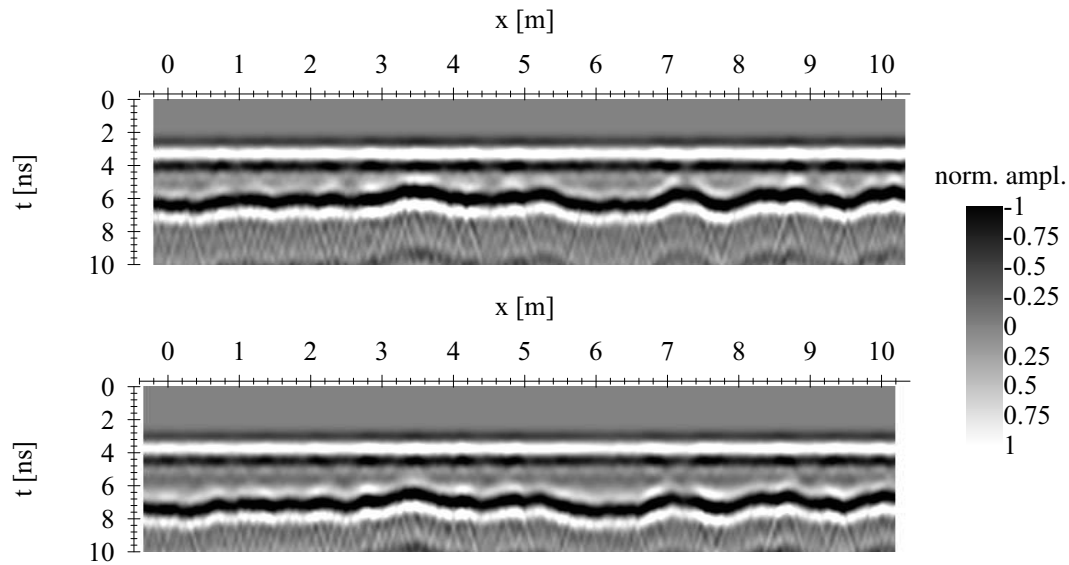


Figure 5.10: Simulated radar measurement on heterogeneous soil (model Fig. 5.9), 400 MHz: first receiver (top) and second receiver (bottom). The first arrival at 2 ns (upper radargram) and 3 ns (lower radargram) is the direct air wave and the second undulating onset is the groundwave.

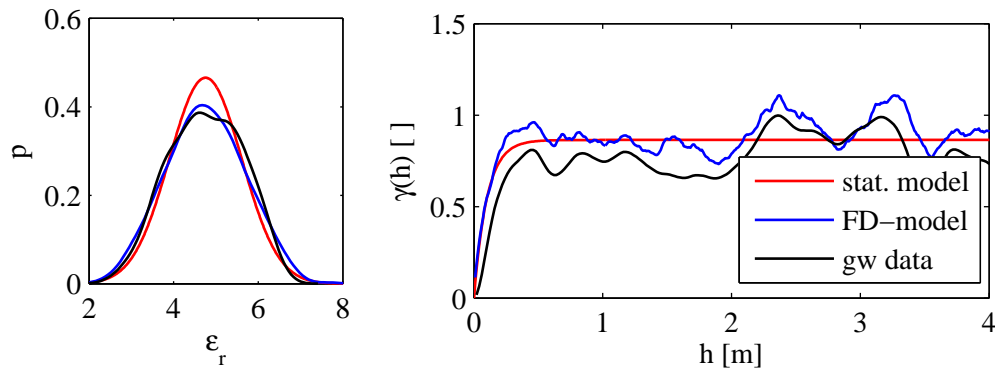


Figure 5.11: Statistical analysis of simulated groundwater measurement on heterogeneous soil: input parameters for the geostatistical simulation (red), simulated model (blue) and permittivity determined from the simulated gw-measurement (black). Left side: probability density function, right side: variogram in x -direction.

5.2.2 Influence on Constant Offset Measurements; Landmine Detection

GPR is seen to be a useful extension to metal detectors in landmine clearance (Bruschini et al., 1998; MacDonald et al., 2003). The use of metal detectors basing on electromagnetic induction methods in either time or frequency domain is sometimes constricted due to the influence of the ground, especially when minimum metal mines have to be detected (Löhken, 2007; Billings et al., 2003; ITEP, 2002). Soils featuring high magnetic susceptibilities influence the signal of metal detectors. If high susceptibilities are combined with high frequency dependence of the susceptibility, e.g. caused by superparamagnetic minerals, metal detectors may become inappropriate. A high amount of metallic clutter, e.g. fragments of grenades, will also cause high false alarm rates which is one of the main problems yielding inefficient performance in landmine clearance.

When a metal detector merely detects metallic objects, GPR maps differences in permittivity and conductivity. Due to the short wavelength it can supply an image of items in the soil and therefore is capable to provide additional information to metal detectors. In the following, the influence of soil heterogeneity on landmine detection with high frequency GPR measurements is analysed using FD calculations. Typical antipersonal mines are cylindrical objects with approximately 0.1 m diameter and 0.04 m height. They are usually placed close to the surface up to 0.2 m depth. The dielectric properties of minimum metal mines correspond to the permittivity of plastic and explosives which is $\epsilon_r^{mine} \approx 3$ with negligible loss tangent (Bruschini et al., 1998).

In the used models, three mines are placed at 0.1 m depth. A constant offset measurement was simulated using a centre frequency of 1.5 GHz and a transmitter-receiver offset of 0.1 m. Several models were calculated featuring soils with different statistical parameters of the heterogeneous electric properties. Table 5.1 lists the physical properties of the models which are plotted in Fig. 5.12 and 5.13.

In model a–c the permittivity is constant and the conductivity is variable. Model a corresponds to a sandy soil as analysed in chapter 3¹. The conductivity in the frequency range of GPR is set to the DC conductivity as in sandy soils ionic conduction is dominant and therefore frequency dependence

¹Note, the conductivity pretends to be homogeneous in model a due to the used colour scale which, for better comparability, covers the range of all models but, as a matter of fact, varies as determined in Tab. 5.1.

Table 5.1: Electromagnetic properties of the mines and the soils used for the simulation of the 1.5 GHz CO radargrams. The mean, the standard deviation (std), the coefficient of variation (cv) and the range a of the exponential variogram function are listed which were used to generate the heterogeneous models.

model	ε_r []			μ_r []	$\lg(\sigma/(S/m))$		
	mean \pm std	cv	a [m]		mean \pm std	cv	a [m]
a	5	-	-	1	-3 ± 0.15	0.05	0.3
b	5	-	-	1	-2 ± 0.5	0.25	0.3
c	5	-	-	1	-1.5 ± 0.5	0.33	0.3
d	4 ± 0.8	0.2	0.3	1	0	-	-
e	5 ± 1	0.2	0.3	1	0	-	-
f	9 ± 1.8	0.2	0.3	1	0	-	-
mine	3	-	-	1	0	-	-

of conductivity is small. Model b and c feature higher conductivities which are known to have a negative effect on GPR performance. High conductivities are typical for salty soils or soils with high clay content. Besides the absolute values, the relative variability was also augmented to obtain higher effects.

Model d–f feature a variable permittivity and constant conductivity. The permittivity distribution of model e corresponds to the statistical parameters determined in chapter 4. Model d corresponds to soil which is quite dry and model f represents moist soil. The permittivity of the three models features the same relative variability, i.e. the same coefficient of variation ².

In Fig. 5.14 the simulated CO-radargrams are depicted. Besides a gain function to counterbalance geometrical spreading, no further processing was applied to the data. If soil permittivity is homogeneous and conductivity is low, the three mines can clearly be recognised by their diffraction hyperbolas (Fig. 5.14 a). This holds true as long as there is a contrast in permittivity between the mines and the soil. Hence, small conductivity variations at small mean conductivities, as typical for sandy soils, do not have a notable effect

²Whether the coefficient of variation of soil moisture and thus permittivity increases or decreases with changing absolute values cannot be generalised. It depends on the soil type, the vegetation and several further parameters. E.g. it depends on the actual water content and the resulting hydraulic potential and at which point of the hysteresis of the water tension function one will start, i.e. if soil is dry and wetted or moist and dried.

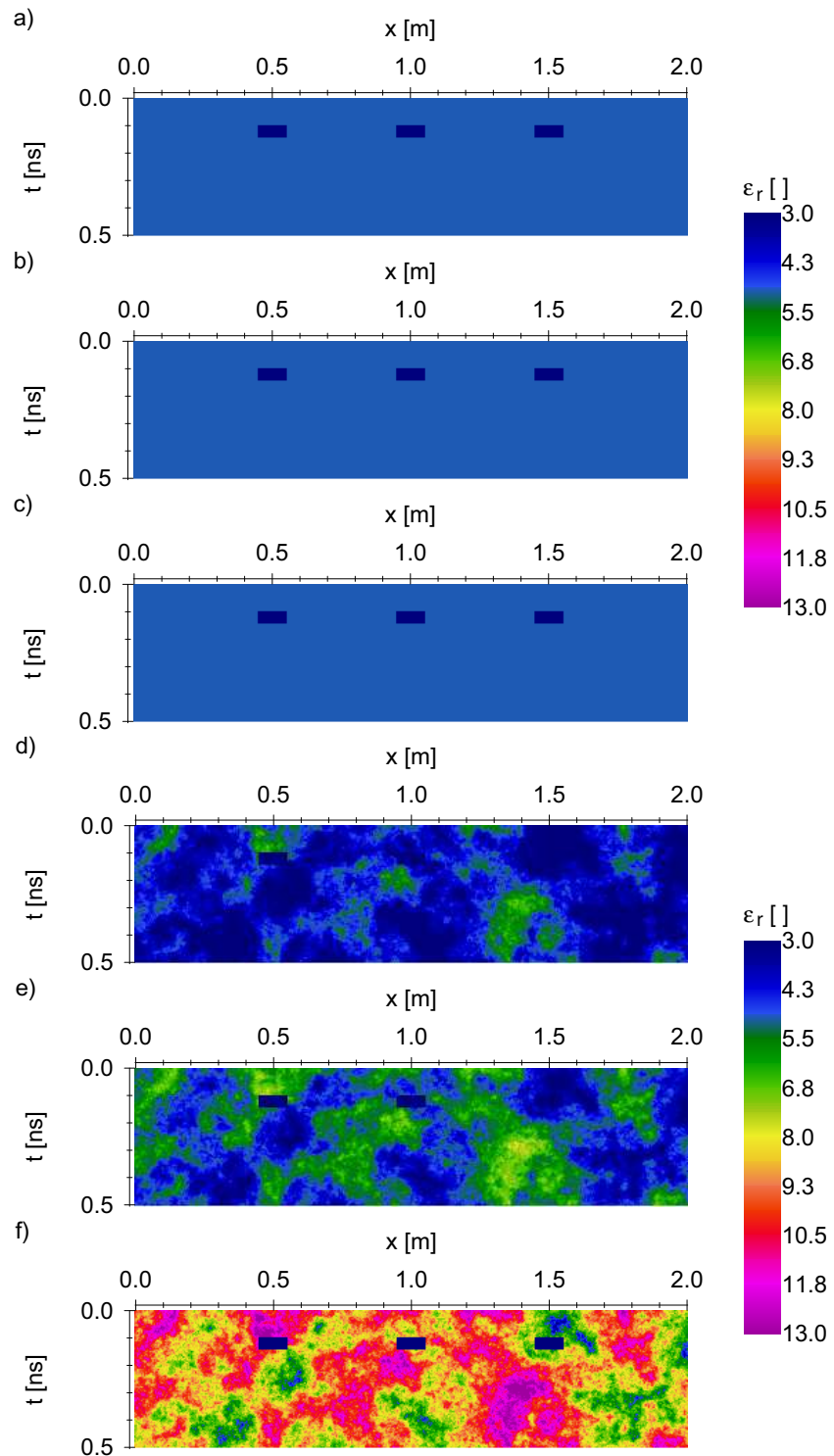


Figure 5.12: Permittivity distribution of the models used to simulate GPR measurements on heterogeneous soils (model parameters see Tab. 5.1). Three mines are placed at 0.1 m depth at $x = 0.5$, 1.0 and 1.5 m.

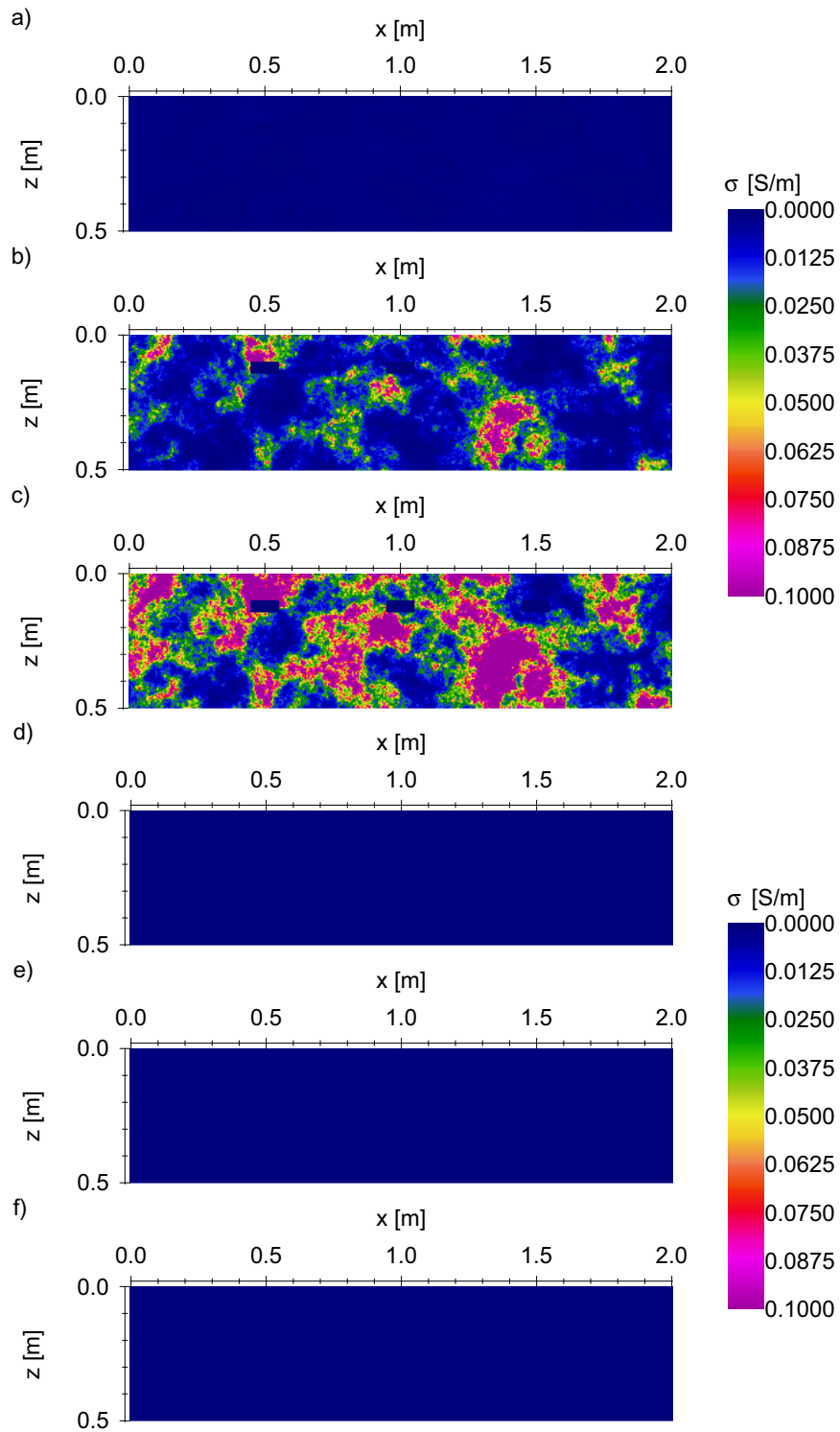


Figure 5.13: Conductivity distribution of the models used to simulate GPR measurements on heterogeneous soils (model parameters see Tab. 5.1). Three mines are placed in 0.1 m depth at $x = 0.5$, 1.0 and 1.5 m.

on GPR performance. If conductivity is heterogeneous and relatively high, the signal of the three mines are damped differently. The mines can still be detected at mid-range conductivities (Fig. 5.14 b). Mine detection will be difficult in the soil of model c as the signal of the left mine is completely damped because it is placed in a high conductive region with $\sigma > 0.1$ S/m.

If soil permittivity is heterogeneous, the form and absolute traveltime of the hyperbolas change due to velocity variations. Another effect of heterogeneity are numberless reflections which interfere with the signals from the mines. The reflections caused by permittivity variations of the models are stronger than the reflections caused even by considerable conductivity variations. If the contrast of the mines to the soil is high as is the case for moist soil, the mine signal is still clearly visible (Fig. 5.14 f). For decreasing water content, the contrast is getting smaller and mines are difficult to detect (Fig. 5.14 e) or cannot be detected any more (Fig. 5.14 d).

The analysis of the simulations show that, with exception of quite conductive soils ($\sigma > 0.05$ S/m), permittivity fluctuations cause stronger problems in mine detection than conductivity variations. If soil is quite dry and the contrast of the target to the soil is small, heterogeneity in soil moisture and resulting permittivity can cause severe problems to mine detection with GPR.

5.2.3 Influence on Moveout Measurements

Moveout (MO) measurements are frequently carried out to separate different wave types and to determine the velocity of the groundwave as introduced in section 4.4. Usually, a straight line is adapted to the groundwave and the slope corresponds to the inverse of the wave velocity in the soil. One effect which can often be observed is a curved groundwave. This can either be caused by wave dispersion due to frequency dependent electromagnetic parameters (Mayer, 2006) or by soil heterogeneity. Besides variations in velocity distribution, a heterogeneous soil also causes reflected and critically refracted waves which may interfere with the groundwave. In order to demonstrate the influence of small-scale permittivity and conductivity variations on moveout measurements and to get an assessment of the effects which might be expected under realistic conditions, a finite difference calculation was carried out simulating a moveout measurement with 1 GHz antennas. The same models were used as for the simulation of landmine detection (Tab. 5.1, Fig. 5.12 and 5.13) but without landmines embedded in the soil. The source emitting a centre frequency of

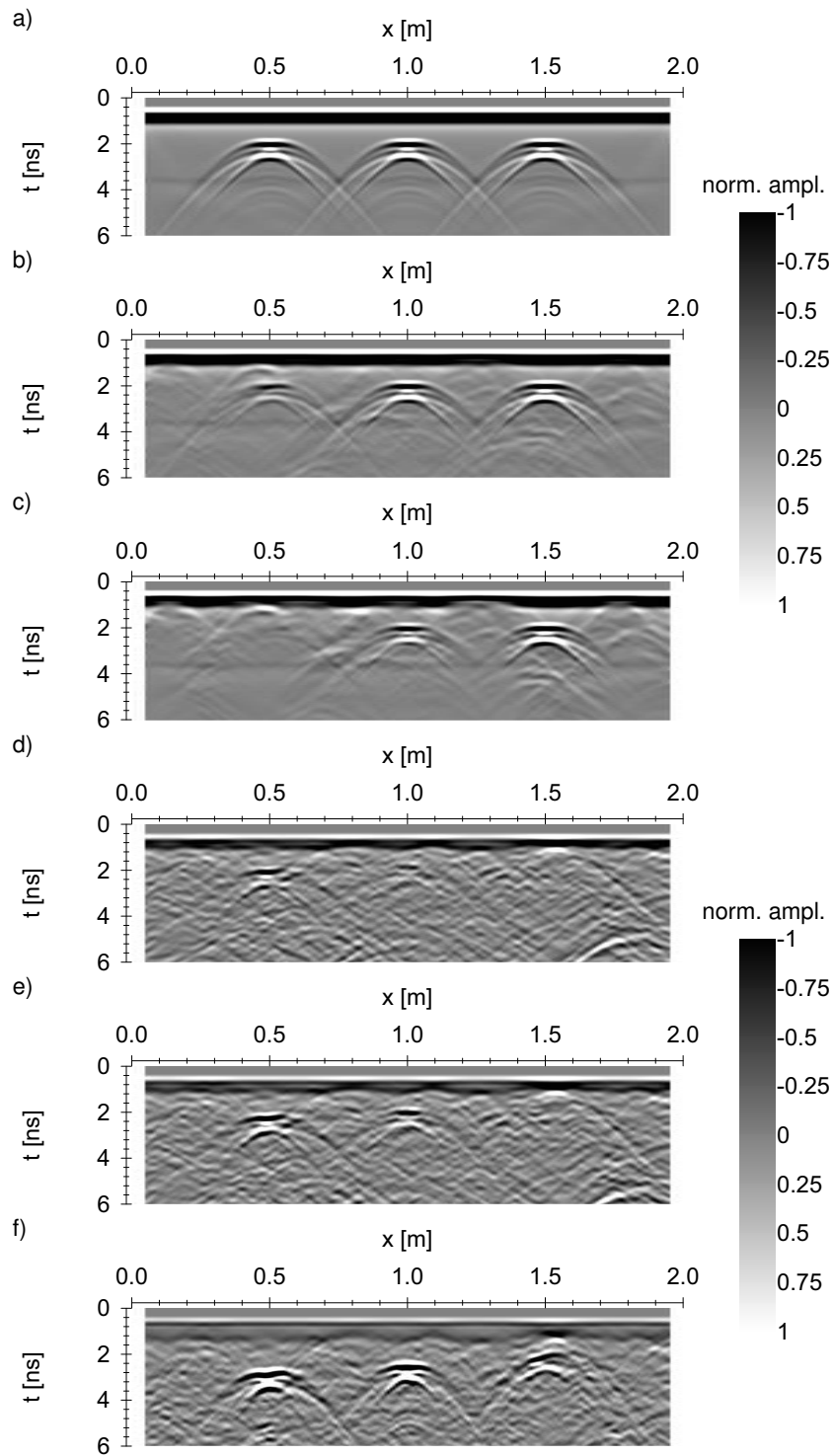


Figure 5.14: Simulated 1.5 GHz CO radar measurements on soils with buried landmines (Fig. 5.12 and Fig. 5.13). The transmitter and receiver were placed 0.01 m above ground and the offset was 0.1 m. a–c: variable conductivity, d–f: variable permittivity.

1 GHz was placed at $x = 1$ m. The receivers were placed every 0.01 m spread about the hole width of the model simulating a moveout measurement to both sides of the transmitter.

Fig. 5.2.3 shows the results of the FD calculation. The air wave and the groundwave are labelled in Fig. 5.2.3 a. Since the soil only features slight conductivity variations on a low absolute level and permittivity is constant, the groundwave describes a straight line. If conductivity and its variability is getting higher, the groundwave is damped but, as long it can be recognised, still describes a straight line (Fig. 5.2.3 b and c).

In contrast, when permittivity is heterogeneous, the groundwave shows distinct curvature and it is not possible any more to fit a straight line (Fig. 5.2.3 d–f). At large offsets, waves which are reflected at heterogeneities can interfere with the groundwave and may cause problems in groundwave determination.

In analogy to the landmine problem discussed above, variations in permittivity, as may be expected under real field conditions, cause stronger effects on GPR performance as conductivity fluctuations. At the locations where the GPR measurements of chapter 4 were carried out, the heterogeneous permittivity distribution will cause severe problems when carrying out standard groundwave measurements. Determining the correct velocity from MO measurements will be a difficult task. But this starting velocity is needed to map soil permittivity in the CO mode, when the standard groundwave measurement technique is applied (Fig. 4.21).

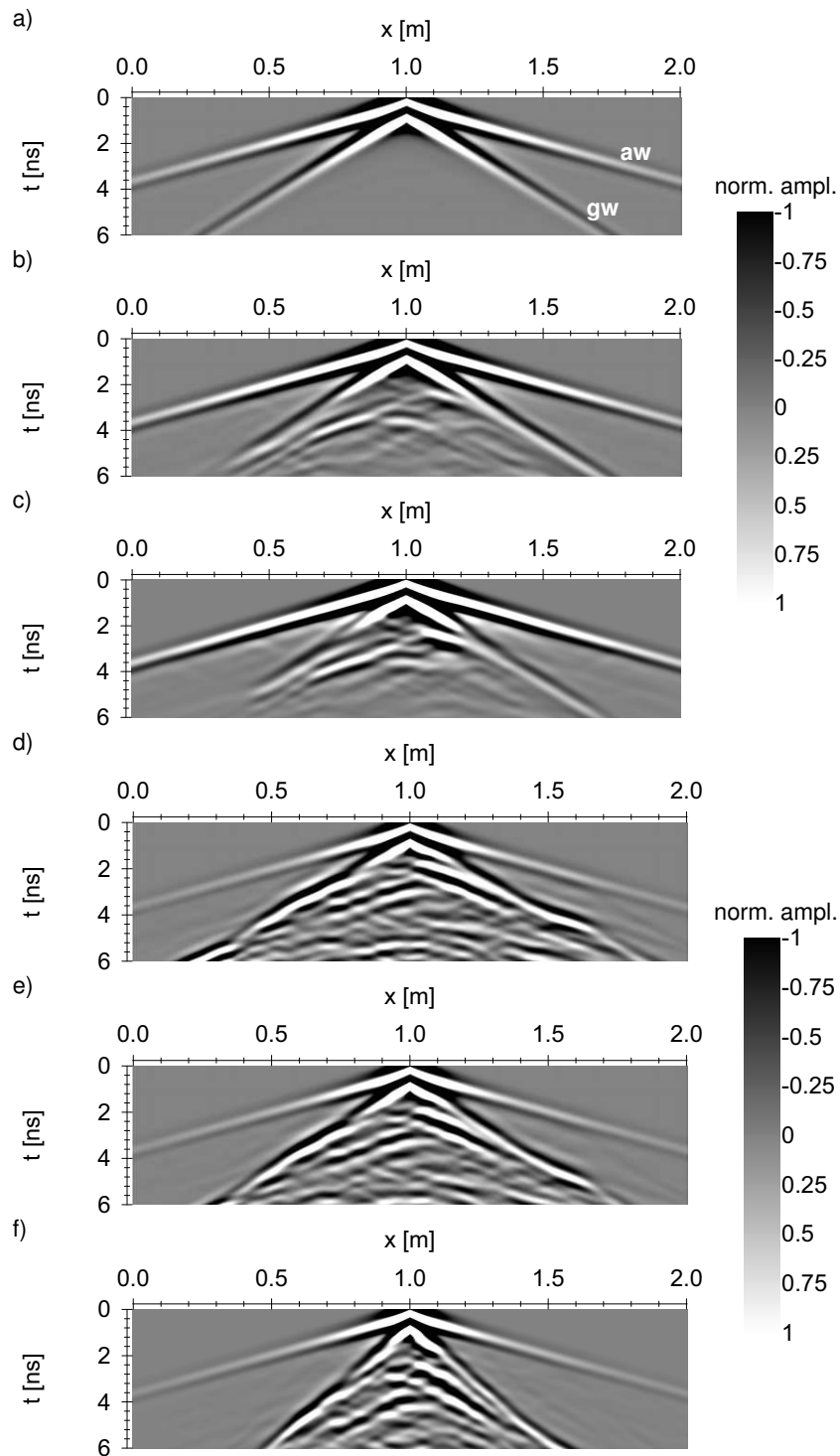


Figure 5.15: Simulated 1.0 GHz MO radar measurements on heterogeneous soils (Fig. 5.12 and Fig. 5.13 without landmines, model parameters see Tab. 5.1). The source was placed at $x = 1$ m and 0.01 m above ground. a–c: variable conductivity, d–f: variable permittivity. aw = airwave, gw = groundwave.

6 Summary and Conclusions

The aim of this work was to quantify the small-scale variability of electric conductivity and permittivity of soils and to determine the effects on resistivity and GPR measurements. The applied modus operandi

- investigate spatial distribution of the physical soil properties in situ with high-resolution geophysics
- analysis of the data and determination of statistical parameters
- geostatistical simulation of random media
- FD calculation of geophysical measurements

showed to be a powerful tool to determine the influence of geologic noise on geophysical measurements and to assess the uncertainties of the results which might be expected under real field conditions.

For the purpose of quantifying the small-scale variability, resistivity mapping techniques and GPR had to be methodically improved to ensure high spatial resolution. The high-resolution field measurements were analysed to derive the statistical parameters which describe the pattern of the spatial variability. These parameters provide the basis to generate synthetic heterogeneous media comparable to the in situ conditions. The synthetic media were used for FD calculations to simulate resistivity and GPR measurements on heterogeneous soils. The resulting synthetic data give an account of the variability and uncertainty which might be expected when carrying out measurements under realistic conditions.

The way the measuring points are allocated on an area influences the statistics which will be derived. Several **sampling layouts** were tested on synthetic heterogeneous media featuring correlation lengths between 0.2 and 2 m. The analysis shows that measurements on crossing profiles and randomly distributed measuring points are superior to layouts at which the sampled points are concentrated on one or a few sub-areas. Thus, several crossing profiles tightly sampled in line direction proved to be most-suited if the statistical parameters of regionalised physical properties are to be determined by geophysical

measurements. This layout shows the best results concerning the reproduction of density function and variogram of the spatial distribution. It is also less sensitive to spatial dislocation, i.e. the result does not strongly depend on the location of the measuring layout inside the area which is to be analysed.

Electric conductivity of soils was determined with DC geoelectrical measurements. A high resolution dipole-dipole setup showed to be suited to determine small-scale variations. Small electrode separations of 0.1 m had to be used and thus electrode geometry could not be disregarded. When using standard electrodes and standard geometric factors assuming point electrodes as are commonly used in geoelectrics, deviations in apparent conductivity up to 50% occur. Therefore, small electrodes were used and an analytical expression has been derived which describes the potential distribution in the vicinity of elongated electrodes and thus providing correct geometric factors. These geometric factors were experimentally verified by carrying out small-scale DC measurements on a homogeneous media, in a water basin. When using the correct geometric factors, the deduced apparent conductivities correspond very well with the real conductivity of the water.

High resolution DC measurements were carried out on a sandy soil used as grassland. Conductivity showed high variability with correlation lengths of some few decimetres and was almost log-normally distributed.

The correlation between soil **permittivity** and soil water content were discussed and some basic models describing the dependence of the two parameters were presented. Soil permittivity was deduced with ground-penetrating radar. The main principles of electromagnetic wave propagation were described starting with Maxwell's equations and, unlike commonly used simplifications, including all three electromagnetic parameters. This allows for assessing the inaccuracy of practical applications if these simplifications are used, e.g. if relative magnetic permeability of the soil is set to $\mu_r = 1$. Two methods were developed to determine permittivity based on two completely different physical contexts providing different depth of investigation: the reflection of waves at the air-soil interface and wave propagation of the groundwave in the soil.

It was shown that the coefficient of reflection of natural soils mainly depends on permittivity and only to a minor degree on permeability and conductivity. A 1 GHz air-launched horn antenna was operated at a distance of 0.5 m to the soil to measure the coefficient of reflection and to deduce the permittivity of the first few centimetres of the soil. Horizontal resolution was experimentally determined to be approximately $0.3 \text{ m} \times 0.25 \text{ m}$ which is a higher resolution as

the Fresnel formulas suggest and might be explained by the radiation pattern of the horn antenna. The accuracy of this method is approximately 10% when applied on a plane soil without vegetation.

Propagation velocity of electromagnetic waves depends on the three EM parameters whereas it was shown that magnetic permeability and electric conductivity have only a minor effect. Common groundwave techniques permit only a relatively low lateral resolution between 0.5 m and some few metres and are time consuming. A new technique was developed using two receiving antennas measuring traveltime differences of the groundwave which enables a fast measuring progress. With this technique permittivity distribution of the top decimetre of the soil can be mapped. When analysing FD simulations and using the same setup and frequencies as in field, the new technique provides a lateral resolution of approximately 1 decimetre. Under ideal measuring conditions, the measuring accuracy of soil permittivity is 3–8% depending on the permittivity itself.

Comparing both methods, permittivity determination by the coefficient of reflection is a very fast method and data processing is quite easy. Thus, it is suited for surveying permittivity of the first centimetres of soil on large areas. Vegetation reduces the determined permittivity and the variability. Groundwave technique is somewhat more complex concerning data acquisition and interpretation but provides a higher resolution and accuracy. It can be used to determine small-scale variabilities of approximately the first decimetre of soil. For proper groundwave identification, the vegetation has to be removed or at least trimmed if high-frequency antennas are used for high-resolution measurements.

Topsoil permittivity was determined at two locations on a sandy soil which was used as grassland. Even though both methods base on different physical effects and provide different penetration depths, they identify the same principal structures and yield comparable statistical results. One location exhibited an isotropic permittivity distribution with a correlation length of 0.35 m and a density function similar to a log-normal distribution. The other location showed normal distributed permittivities and an anisotropic spatial pattern caused by the former cultivation of the area. The minimal correlation length is 0.25 m and tends to be perpendicular to the former ploughing direction whereas the correlation length is 5 times larger parallel to this direction. A surprising result is that even though the location has been used as grassland for several years, the influence of former cultivation still influences soil moisture pattern. This might be caused by soil compaction, an uneven plough

horizon or by the influence of former cultivation on actual vegetation and thus on evapotranspiration and moisture.

The **influence of soil heterogeneity** on resistivity and GPR measurements has been analysed by means of FD calculations with random models featuring comparable variability as the soil in situ. It was shown that the used high-resolution dipole-dipole setup with electrode separations of 0.1 m can be used to determine small-scale conductivity variations. The variogram is well reproduced for correlation lengths between 0.2 and 2 m by both, 2D and 3D DC measurements. The true variance and thus variability is underestimated by the measurements if the correlation length is small but the mean and shape of the density function are well reproduced. Possibly, an inversion without smoothness constraints or with adaptive smoothness would provide better results.

The influence of soil variability on resistivity measurements was exemplarily demonstrated on the basis of Schlumberger soundings. Several different realisations of models with heterogeneous soil according to the soil analysed in situ were used for FD forward calculations. The synthetic data showed variations in the sounding curves yielding uncertainties in the inverted models. Topsoil ($z = 0\text{--}0.3$ m) causes uncertainties in the deduced models according to 6% data error whereas subsoil ($z = 0.3\text{--}1$ m) only causes uncertainties comparable to approximately 2% error. This is an effect of decreasing sensitivity with increasing depth. It was shown that often soil heterogeneity and not the measuring inaccuracy of the device is the factor which limits the accuracy of electric resistivity soundings.

FD calculations on heterogeneous media proved the 2-receiver groundwave technique being capable to properly determine the statistical parameters of permittivity distribution. The density function and the variogram are well reproduced even if correlation length is short.

GPR measurements are affected by both, electric conductivity and permittivity. The influence of variations of these two parameters on CO and MO measurements were analysed. High frequency CO measurements (1.5 GHz) for the detection of landmines were simulated with FD calculations. The mines were placed in different heterogeneous media exhibiting correlation lengths of 0.3 m. Conductivity and permittivity were varied independently to study the effects on the detectability of the mines. Conductivity of common sandy soils showed no influence on GPR performance and mine detection is negatively affected only if conductivity is higher than 0.05 S/m. Permittivity variations of common soils showed to have a stronger effect on GPR than conductivity

variations. Especially if the soil is quite dry and the dielectric contrast between mines and soil is small, variability as is typical for sandy soils can cause severe problems. The mine signal is masked by several reflection hyperbolas caused by soil heterogeneities and mines cannot be detected any more with GPR. If soil is moist, mines can be detected more easily even if heterogeneity is pronounced. However, the accuracy of depth determination of the mines will suffer from velocity variations.

The same soil models were used to simulate MO measurements. Here again, permittivity showed to have a stronger effect on the results than conductivity. A variable permittivity causes a curved groundwave as can frequently be observed in field data making velocity determination with standard groundwave technique a difficult task. If heterogeneity is strong, the groundwave might be superposed by reflected and critically refracted waves which can cause severe problems to a proper groundwave identification. When carrying out CMP measurements as are frequently used for velocity versus depth determination, similar effects are to be expected and might evoke inaccuracies.

Outlook

In this thesis, conductivity and permittivity have been determined on sandy soils which are used as grassland. Measurements should be expanded to other soil types and cultivations to obtain typical parameters of spatial pattern of the electric parameters. Such a database would be helpful to assess uncertainties of geophysical measurements on diverse locations.

Soil moisture and accordingly electrical properties do not only feature high spatial variability but are also highly variable with time. As the developed techniques are non-destructive, they can repeatedly be applied at the same place. Albeit soil moisture determination with geophysical methods has some limitations concerning accuracy and resolution, the ability of repeated measurements on the same undisturbed soil is a crucial advantage over classical soil scientific methods as e.g. gravimetric soil moisture determination. Repeated measurements will provide important information on how a spatial moisture pattern changes with time, e.g. due to seasonal variations within a hydrologic year, with a unique precipitation event or with cultivation and plant growth. This information will help to understand the formation of hydrophobic and hydrophilic domains, water infiltration and pollution or the interaction of precipitation, soil, vegetation and evapotranspiration. Especially the small-scale heterogeneity of soil moisture is mostly not known and is an important input parameter for weather and climate simulations.

There is a lack of non-destructive methods to determine high-resolution soil-permittivity variations with depth. First FD calculations have shown that the depth of influence of the proposed 2-receiver groundwave technique depends on the distance between the transmitter and the two receivers. Keeping the distance between both receivers constant and varying the distance between the transmitter and the receivers seems to be a promising technique enabling a vertical permittivity sounding. Combining several of these soundings in combination with an inversion could provide a 2D or 3D permittivity distribution of the ground. However, extensive FD calculations comprising the antennas and measurements under controlled conditions will be needed to understand the complex dependence of the depth of influence from antenna frequency, separation and permittivity distribution of the ground.

Geostatistical simulation techniques proved to be a suitable tool to generate realistic heterogeneous soil models for FD calculations. Geostatistical analysis has the potential to be applied to optimise inversion algorithms which are e.g. used for the determination of underground resistivity. The choice of inversion parameters has a great influence on the inversion result. In case of a Gauss-Newton algorithm these are the discretisation and regularisation. Different choice of assumed data errors as input for the inversion are equivalent to different regularisation parameters. The higher the errors/regularisation the smoother the inversion result. Thus realistic error estimation is essential for data interpretation by means of inversion. Geostatistics can on the one hand provide information on realistic measuring errors due to geologic noise. On the other hand, geostatistical analysis of the inverted models might be compared with the statistics of the underground which is expected or a priori known and used to ascertain optimal inversion parameters.

So far, geostatistical simulation is not a standard technique, e.g. when models are created for FD calculations. However, it proved to be a powerful tool to integrate random, which characterises natural processes and states, to computer simulations. Geostatistics provides an essential tool to generate realistic synthetic data, e.g. for feasibility studies, optimising experimental design or assessing realistic errors. The methods described may boost geophysical techniques and thus considerably contribute to a global understanding of the interaction of lithosphere and atmosphere.

Appendix A

Results of Different Sampling Layouts on Simulated Data

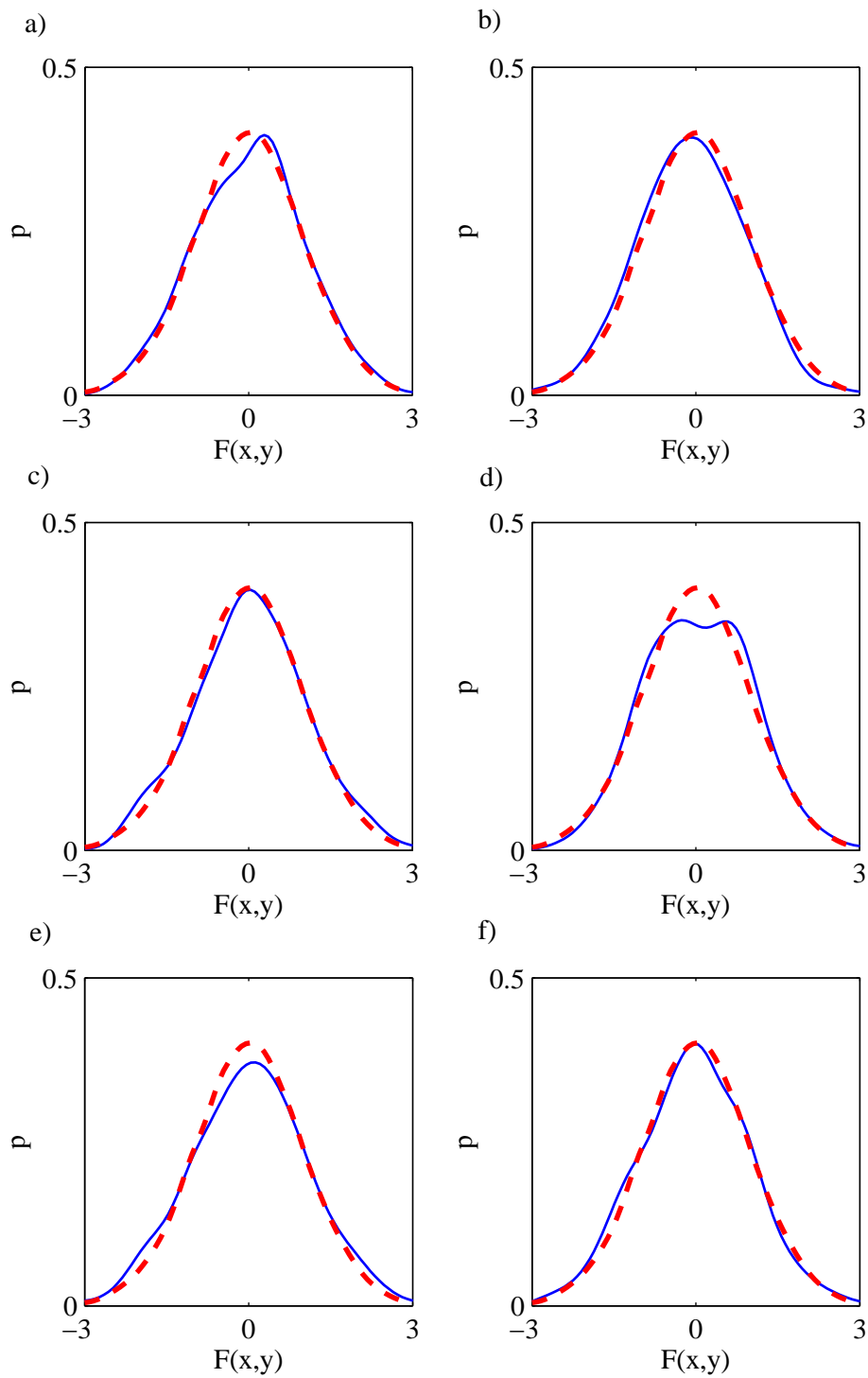


Figure A.1: Experimental distribution functions of the extracted data (blue solid line) and distribution function of the exhaustive dataset (red dashed line). The random variable was simulated using a standard normal distribution and an exponential semivariogram with $a = 0.2$ m.

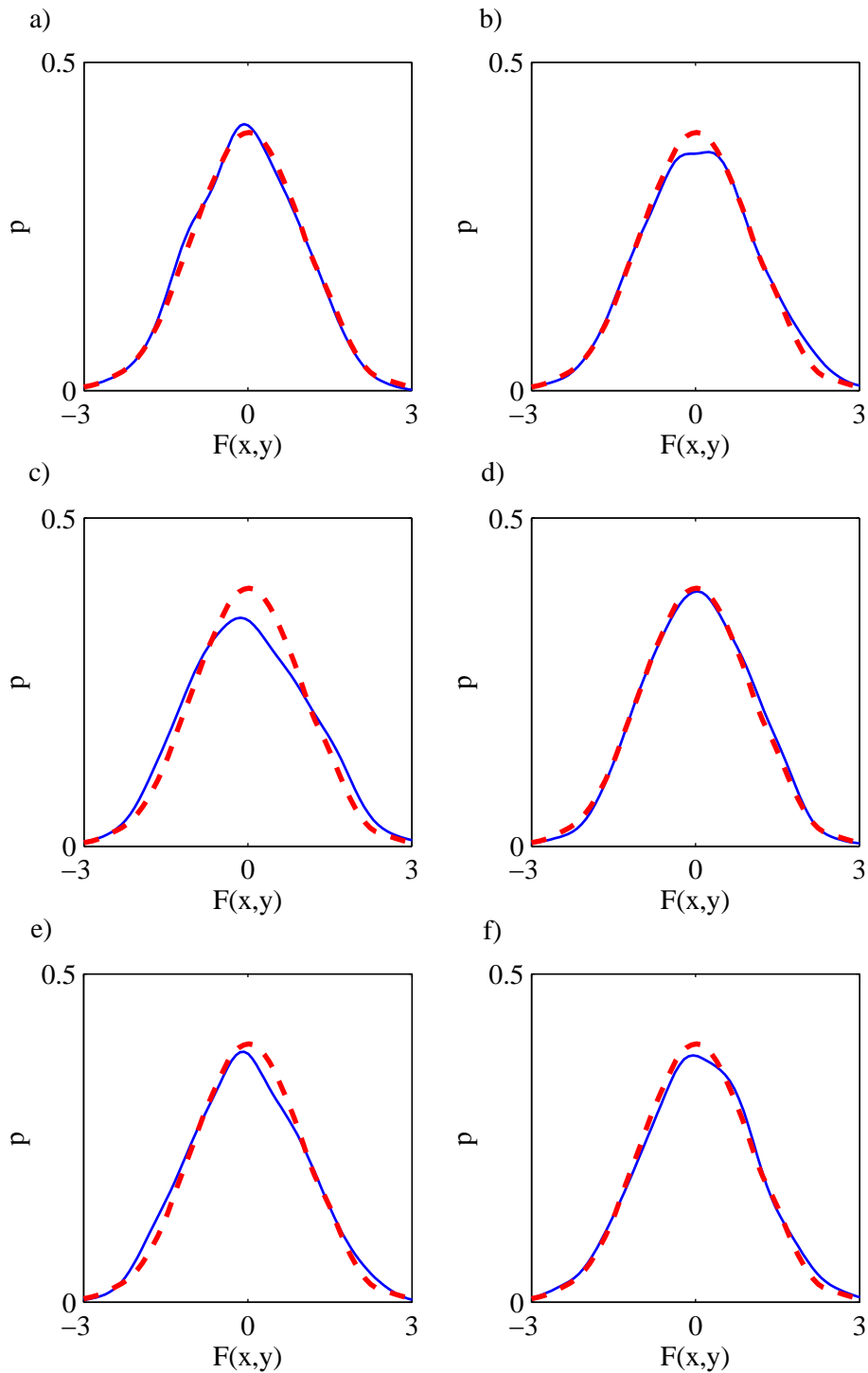


Figure A.2: Experimental distribution functions of the extracted data (blue solid line) and distribution function of the exhaustive dataset (red dashed line). The random variable was simulated using a standard normal distribution and an exponential semivariogram with $a = 0.5$ m.

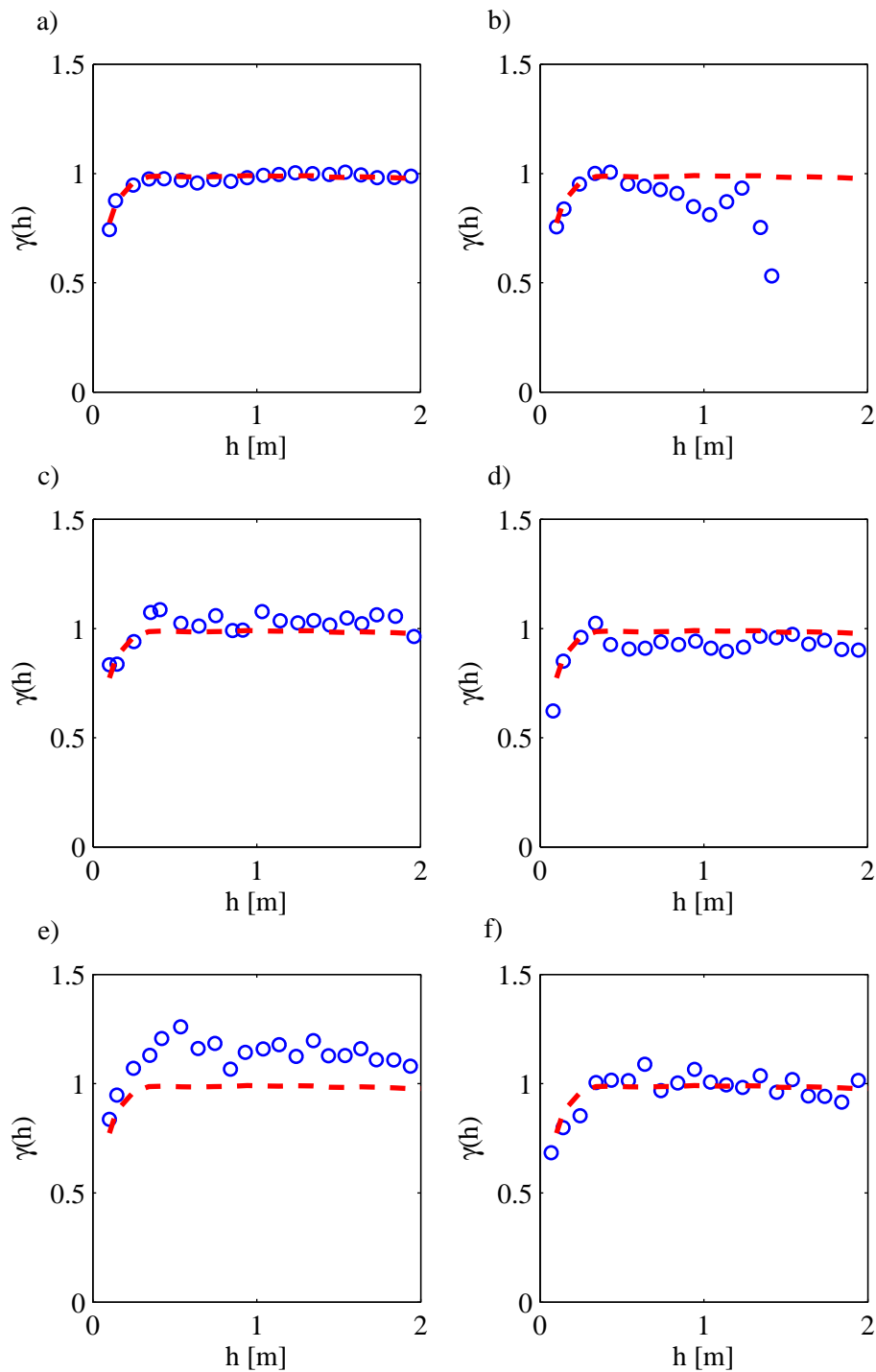


Figure A.3: Experimental variograms of the data extracted with the setups of Fig. 2.7 (blue circles) and variograms of the exhaustive dataset sampled with a 0.1 m grid (red dashed line). The random variable was simulated using a standard normal distribution and an exponential semivariogram with $a = 0.2$ m.

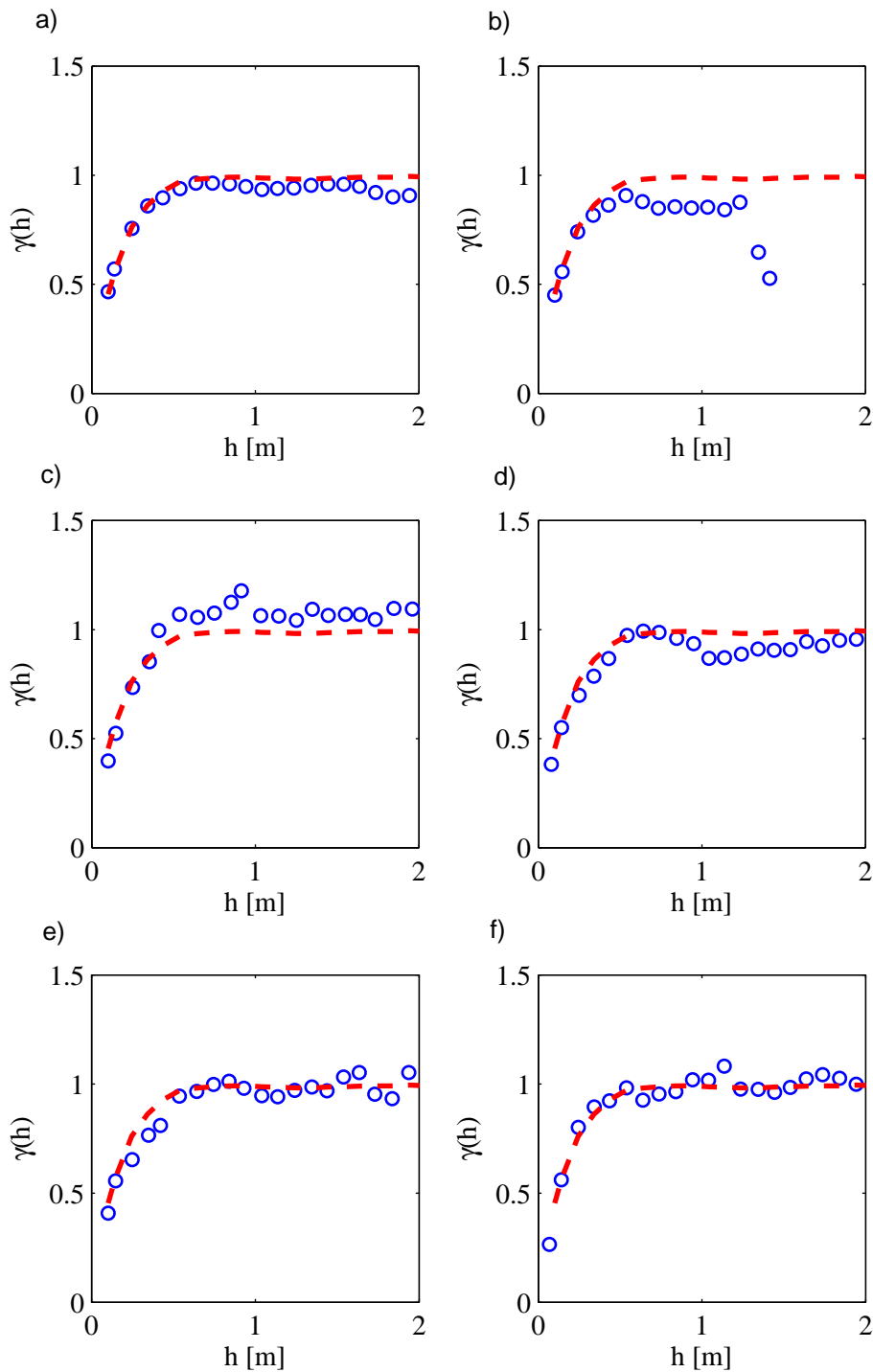


Figure A.4: Experimental variograms of the data extracted with the setups of Fig. 2.7 (blue circles) and variograms of the exhaustive dataset sampled with a 0.1 m grid (red dashed line). The random variable was simulated using a standard normal distribution and an exponential semivariogram with $a = 0.5$ m.

Appendix B

Pedological Description of the Measuring Locations

B.1 Location 1

location: Hannover Buchholz, Germany
soil type: Cambic Podzol
land use: grassland for at least 10 years, formerly ploughed acre
groundwater table: > 1 m

Estimated specifications (Preetz, pers. comm.)

topsoil:
depth: 0–0.28 m
texture: sand, slightly loamy
humus content: 4%
soil colour: dark brownish grey
lime content: 0%
stone content: 1–2% gravel
parent material: fluvatile pleistocene sand

subsoil:
depth: 0.28–0.40 m
texture: sand
humus content: 0.5%
soil colour: light greyish brown
lime content: 0%
stone content: 1–2% gravel
parent material: fluvatile pleistocene sand

underground: fluvatile pleistocene sand



Figure B.1: Picture of soil profile at location 1. Soil horizons due to German soil classification (Ad-hoc-AG Boden, 2005): 0–28 cm: rAp, 28–40 cm: rAp+ Ae+Bs, 40–50+ cm: Cv.

B.2 Location 2

location: Fuhrberg, 30 km north of Hannover, Germany
soil type: Cambic Podzol
land use: grassland for 2 years, formerly ploughed acre
groundwater table: > 1 m

Estimated specifications (Preetz, pers. comm.)

topsoil:

depth: 0–0.35 m
texture: sand, silty loamy
humus content: 4%
soil colour: dark grey
lime content: 0%
stone content: 1–2% gravel
parent material: fluvialite pleistocene sand

subsoil:

depth: 0.35–0.55 m
texture: sand
humus content: 0.5%
soil colour: yellowish brown
lime content: 0%
stone content: 1–2% gravel
parent material: fluvialite pleistocene sand

underground: fluvialite pleistocene sand

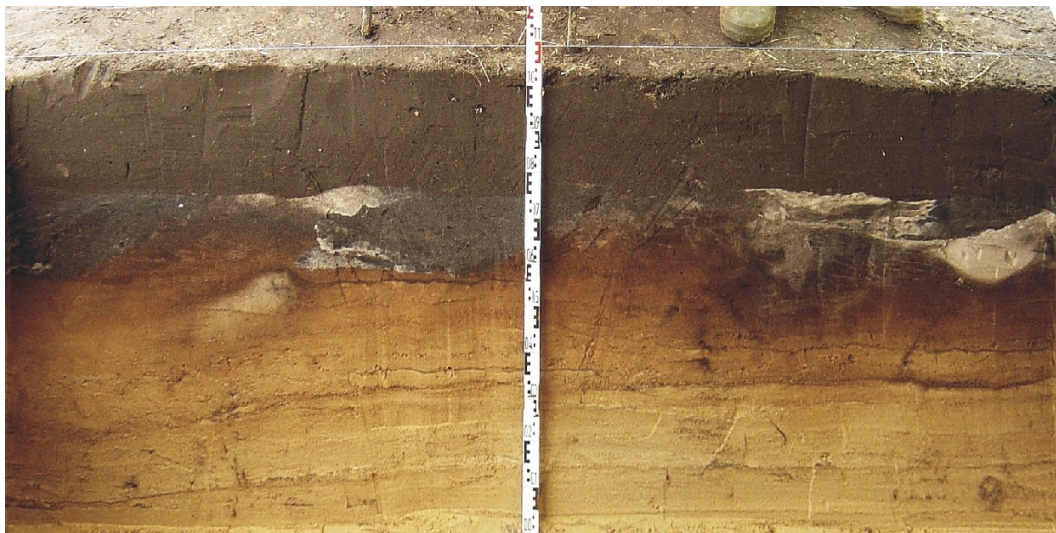


Figure B.2: Picture of soil profile at location 2 (S. Altfelder, pers. comm). Soil horizons due to German soil classification (Ad-hoc-AG Boden, 2005): 0–25 cm: Ap, 25–35 cm: Ap+Ae+Bhs, 35–55 cm: Bsv 55–100+ cm: Cv.

Table B.1: Results of laboratory measurements on soil samples, location 2 (Niedersächsisches Landesamt für Bodenforschung, NLFb)

	depth	sand	silt	clay	CaCO ₃	C _{org}	humus	Fe ₂ O ₃
	cm	% of humus-free soil			% of total soil			
topsoil (A)	0–27	87.0	5.2	7.8	0	2.4	4.2	0.63
subsoil (B)	27–50	93.4	4.6	2.0	0	0.1	0.2	0.11

B.3 Location 3

location: Hannover Buchholz, Germany
soil type: Arenosol
land use: grassland since approximately 25 years, reclaimed land
groundwater table: > 1 m

Estimated specifications (Preetz, pers. comm.)

topsoil:

depth: 0–0.36 m
texture: sand, slightly loamy
humus content: 5%
soil colour: dark grey
lime content: 0%
stone content: 1–2% gravel
parent material: anthropogenic deposition, humus rich sand

buried soil:

depth: 0.36–0.65 m
texture: sand, slightly silty
humus content: 2%
soil colour: light grey
lime content: 0%
stone content: 1–2% gravel
parent material: fluvatile pleistocene sand

subsoil:

depth: 0.65–0.8 m
texture: sand, slightly silty
humus content: 0%
soil colour: yellowish brown
lime content: 0%
stone content: 1–2% gravel
parent material: fluvatile pleistocene sand

underground: fluvatile pleistocene sand



Figure B.3: Picture of soil profile at location 3. Soil horizons due to German soil classification (Ad-hoc-AG Boden, 2005): 0–10 cm: jAh, 10–32 cm: jAh2, 32–36 cm: f(j)Ah, 36–65 cm: Bv.

Used Symbols and Abbreviations

Abbreviations

aw ...	airwave
CD ...	coefficient of deviation
CDF ...	cumulative density function
CMP ...	common mid point
CO ...	constant offset
DC ...	direct current
exp ...	exponential function
EM ...	electromagnetic
FD ...	finite difference
GPR ...	ground-penetrating radar
GSSI ...	Geophysical Survey Systems, Inc.
gw ...	groundwave
MO ...	moveout
PDF ...	probability density function
RMS ...	root mean square
RRMS ...	relative root mean square
SIP ...	spectral induced polarisation
TDR ...	time-domain reflectometry
WARR ...	wide angle reflection and refraction
2D ...	2 dimensional
3D ...	3 dimensional

Physical and mathematical constants

c_0 ...	speed of light = $2.9979 \cdot 10^8$ m/s
i ...	imaginary unit = $\sqrt{-1}$
ϵ_0 ...	dielectric permittivity of free space = $8.8510 \cdot 10^{-12}$ As/Vm
μ_0 ...	magnetic permeability of free space = $4\pi \cdot 10^{-7}$ Vs/Am

Symbols

$a \dots$	range [m]
$a \dots$	dipole length [m]
$a \dots$	formation factor
$\vec{A} \dots$	vector field
$\vec{B} \dots$	magnetic flux density [T]
$C \dots$	sill
$C_0 \dots$	nugget effect
$\text{Cov} \dots$	covariance
$d \dots$	diameter [m]
$d_i \dots$	data points
$\vec{D} \dots$	electric flux density [C/m ²]
$E \dots$	expectation
$\vec{E} \dots$	electric field strength [V/m]
$E_0 \dots$	emitted electric field strength [V/m]
$E_n \dots$	field strength contribution of the n-th Fresnel zone [V/m]
$f \dots$	function
$F \dots$	regionalised data
$G \dots$	Gaussian data
$h \dots$	lag distance [m]
$h \dots$	height [m]
$\vec{h} \dots$	lag distance vector [m]
$\vec{H} \dots$	magnetic field strength [A/m]
$I \dots$	current [A]
$\vec{j} \dots$	free current density [A/m ²]
$\vec{k} \dots$	wavenumber vector [1/m]
$k_B \dots$	Boltzmann's constant = $1.38 \cdot 10^{-23}$ J/K
$K \dots$	configuration factor [m]
$l \dots$	length [m]
$m \dots$	mean
$m \dots$	cementation factor
$M \dots$	model
$n \dots$	dipole separation []
$n \dots$	saturation exponent
$N \dots$	natural number
$p \dots$	probability density
$p \dots$	electric dipole moment [Cm]
$\vec{P} \dots$	polarisation density [C/m ²]
$r \dots$	radius [m]

$R \dots$	receiver
$\vec{r} \dots$	position vector [m]
$s_n \dots$	travel path of the n-th Fresnel zone [m]
$t \dots$	time [s]
$T \dots$	transmitter
$T \dots$	periodic time [s]
$T \dots$	temperature [K]
$U \dots$	voltage [V]
$v \dots$	velocity [m/s]
$V \dots$	volumetric fraction [m ³ /m ³]
$\text{Var} \dots$	variance
$\vec{x} \dots$	position vector [m]
$Z \dots$	random function
$\alpha \dots$	angle [°]
$\alpha \dots$	attenuation constant [1/m]
$\beta \dots$	phase constant [1/m]
$\Phi \dots$	normal score transformation
$\Phi \dots$	potential field
$\Phi \dots$	effective porosity [m ³ /m ³]
$\gamma \dots$	semivariance
$\delta \dots$	Dirac's delta function, $\delta(x) = \infty$ for $x = 0$; $\delta(x) = 0$ for $x \neq 0$
$\varepsilon_r \dots$	relative dielectric permittivity []
$\varepsilon_{eff} \dots$	effective dielectric permittivity []
$\Theta_V \dots$	volumetric soil water content [m ³ /m ³]
$\lambda \dots$	wavelength [m]
$\lambda \dots$	anisotropy factor []
$\mu_r \dots$	relative magnetic permeability []
$\nu \dots$	frequency [1/s]
$\xi \dots$	variable
$\rho \dots$	resistivity [Ωm]
$\rho_a \dots$	apparent resistivity [Ωm]
$\varrho_{el} \dots$	electric charge density [C/m ³]
$\varrho_N \dots$	molecule density [1/m ³]
$\rho \dots$	coefficient of reflection []
$\sigma \dots$	electrical conductivity [S/m]
$\sigma_a \dots$	apparent conductivity [S/m]
$\sigma_q \dots$	interface conductivity [S/m]
$\sigma_w \dots$	conductivity of pore fluid [S/m]
$\sigma \dots$	RMS deviation
$\tau \dots$	coefficient of transmission []

$\tau \dots$	relaxation time [s]
$\omega \dots$	angular frequency = $2\pi \nu$ [1/s]
$\vec{\nabla} \dots$	Nabla operator = $(\partial/\partial x, \partial/\partial y, \partial/\partial z)$
$\Delta \dots$	Laplace operator = $(\partial^2/\partial x^2 + \partial^2/\partial y^2 + \partial^2/\partial z^2)$
$* \dots$	convolution operator $a(t) * b(t) = \int_{-\infty}^{\infty} a(\tau)b(t - \tau) d\tau = \int_{-\infty}^{\infty} a(t - \tau)b(\tau) d\tau$
$\forall \dots$	for all

Indices and accents

' ...	real part
" ...	imaginary part
$t \dots$	tangential component
$n \dots$	normal component
$a, b \dots$	medium a or b
$a, m, w, bw \dots$	air, soil matrix, water, bound water
$i, r, t \dots$	incident, reflected, and transmitted wave
$x, y, z \dots$	x , y , and z component of a vector

List of Figures

1.1	Picture of a sandy topsoil	3
1.2	Guideline of the thesis	5
2.1	Schema of normal score transformation	11
2.2	Exemplary experimental semivariogram	12
2.3	Basic semivariogram models	13
2.4	Illustration of ergodic fluctuations of geostatistical simulations .	16
2.5	Simulated data distribution on a 10 m × 10 m area	18
2.6	Deduced geostatistical parameters of simulated data	20
2.7	Different setups used for data sampling	21
2.8	Experimental PDF of extracted simulated data ($a = 2$ m) . . .	22
2.9	Summarisation of statistical parameters of extracted PDFs . . .	24
2.10	Experimental variograms of extracted simulated data ($a = 2$ m)	25
2.11	Illustration of the position of the analysed areas in the field . . .	26
2.12	Repeatability of the experimental PDF	27
2.13	Repeatability of the experimental variogram	28
3.1	Schematic illustration of a 4-electrode DC measurement	35
3.2	Geometric factor for elliptical and point electrodes	37
3.3	Water experiment to determine influence of electrode geometry .	38
3.4	Point vs. elliptical electrodes, deduced conductivities	38
3.5	Location of the profiles for DC measurements	40
3.6	Inverted DC geoelectric profiles at location 1	42
3.7	Probability density function of the conductivity at location 1 . .	44
3.8	Variograms of conductivity distribution at location 1	45
4.1	Schematic illustration of soil compounds	47
4.2	Frequency dependent permittivity of water	50
4.3	Schematic diagram of TDR principle	54
4.4	Reflection and transmission of EM waves	60
4.5	Fresnel zones of a reflecting interface	65
4.6	Different wave types at the interface air–soil	68
4.7	Coefficient of reflection depending on μ , ε and σ	71
4.8	Experimental setup, horn antenna	73

4.9	Radar traces of a reflection at metal, soil and soil + vegetation .	74
4.10	Experimental determination of the footprint of the horn antenna	75
4.11	ε determined in reflection mode along a 10 m profile	77
4.12	Amplitude drift of the GSSI GPR system	78
4.13	Measuring grid and ε -distribution at location 2	79
4.14	PDF of ε with and without vegetation (location 2)	80
4.15	Directional variogram of the 2D ε -distribution (location 2) . . .	81
4.16	Gridded 2D ε distribution by coefficient of reflection (location 2)	82
4.17	PDF of ε at location 3	83
4.18	Variogram of ε -distribution at location 3	84
4.19	Gridded 2D ε distribution by coefficient of reflection (location 3)	85
4.20	Phase velocity depending on μ , ε and σ	86
4.21	Schematic traveltime diagram of groundwave measurement . . .	88
4.22	Setup for groundwave measurement	90
4.23	FD simulation of CO groundwave measurement	92
4.24	Groundwave analysis of synthetic radargram with 1 anomaly . .	93
4.25	Groundwave analysis of synthetic radargram with 2 anomalies .	94
4.26	Groundwave analysis of sand box measurement	95
4.27	Groundwave field measurement compared to TDR	96
4.28	Time drift of the GPR system	97
4.29	Measuring grid and ε -distribution at location 2	99
4.30	PDF of the groundwave data at location 2	99
4.31	Variogram of the groundwave data at location 2	100
4.32	Gridded 2D ε -distribution by groundwave (location 2)	101
4.33	PDF of the groundwave data at location 3	102
4.34	Variogram of the groundwave data at location 3	103
4.35	Gridded 2D ε -distribution by groundwave (location 3)	103
5.1	3D FD model used to simulate 3D and 2D measurements	107
5.2	2D and 3D measurements on a medium with 2 m range	109
5.3	2D and 3D measurements on a medium with 0.5 m range	110
5.4	2D and 3D measurements on a medium with 0.2 m range	111
5.5	Statistical analysis of 2D and 3D inversion for $a = 0.2 - 2$ m . .	112
5.6	Resistivity models for Schlumberger sounding simulation	113
5.7	FD simulation of soundings on heterogeneous topsoil	114
5.8	FD simulation of soundings on heterogeneous subsoil	116
5.9	Model of heterogeneous soil for FD-groundwave simulation . . .	118
5.10	Simulated radargrams of gw measurement on heterogeneous soil	119
5.11	Statistical analysis of simulated gw measurements	119
5.12	Permittivity distribution of the landmine models	122

5.13	Conductivity distribution of the landmine models	123
5.14	Simulated 1.5 GHz CO radargrams on soils with landmines . . .	125
5.15	Simulated 1.0 GHz MO radargrams on heterogeneous soils . . .	127
A.1	Experimental PDF of extracted simulated data, $a = 0.2$ m . . .	136
A.2	Experimental PDF of extracted simulated data, $a = 0.5$ m . . .	137
A.3	Experimental variograms of extracted simulated data, $a = 0.2$ m	138
A.4	Experimental variograms of extracted simulated data, $a = 0.5$ m	139
B.1	Picture of soil profile at location 1	142
B.2	Picture of soil profile at location 2	144
B.3	Picture of soil profile at location 3	146

List of Tables

3.1	Adaption of the inverted model to the data, point electrodes vs. elliptical electrodes	41
5.1	Electromagnetic properties of the models used for the simulation of landmine detection with GPR	121
B.1	Results of laboratory measurements on soil samples, location 2 .	144

Used Software

- GSLIB (Deutsch and Journel, 1998): geostatistical simulation
- variowin (Pannatier, 1996): variogram calculation, analysis and model adaption
- Surfer8: variogram calculation, kriging
- DC2dInvRes, DC3dInvRes: resistivity FD simulation and inversion (<http://www.resistivity.net>)
- Reflex (Sandmeier, 2006): GPR data analysis and FD simulation
- Matlab7: statistical analysis, scripts and plots
- dot: generation of flowchart diagram (<http://www.graphviz.org>)
- L^AT_EX 2_ε: text setting and layout

Bibliography

- Ad-hoc-AG Boden (2005). *Bodenkundliche Kartieranleitung*. Hannover, Germany, 5th edition.
- Archie, G. E. (1942). The electrical resistivity log as an aid in determining some reservoir characteristics. *Transactions of the American Institute of Mining, Metallurgical and Petroleum Engineers*, 146:54–62.
- Becht, A., Appel, E., and Dietrich, P. (2006). Analysis of multi-offset gpr data: a case study in a coarse-grained gravel aquifer. *Near Surface Geophysics*, 4:227–240.
- Billings, S. D., Pasion, L. R., Oldenburg, D. W., and Foley, J. (2003). The influence of magnetic viscosity on electromagnetic sensors. *EUDEM – SCOT2, Int. Conf. on Requirements and Technologies for the Detection, Removal and Neutralization of Landmines and UXO, Brussels*.
- Birchak, J. R., Gardner, C. G., Hipp, J. E., and Victor, J. M. (1974). High dielectric constant microwave probes for sensing soil moisture. *Proceedings of the IEEE*, 62:93–98.
- Brekhovskikh, L. M. (1980). *Waves in Layered Media*. Academic Press, inc.
- Bronstein, I. N. and Semendjajew, K. A. (1991). *Taschenbuch der Mathematik*. Teubner, 25. edition.
- Bruschini, C., Gros, B., Guerne, F., Pièce, P.-Y., and Carmona, O. (1998). Ground penetrating radar and imaging metal detector for antipersonal mine detection. *Journal of Applied Geophysics*, 40:59–71.
- Chanzy, A., Tarussov, A., Judge, A., and Bonn, F. (1996). Soil water content determination using a digital ground-penetrating radar. *Soil Science Society of America Journal*, 60:1318–1326.
- Chilès, J.-P. and Delfinier, P. (1999). *Geostatistics: modelling spacial uncertainty*. Wiley series in probability and statistics. John Wiley and Sons.

- Daily, W., Ramirez, A., LaBrecque, D., and Nitao, J. (1992). Electrical resistivity tomography of vadose water movement. *Water Resources Research*, 28(5):1429–1442.
- Dam, R. L. v., Borchers, B., and Hendrickx, J. M. H. (2005). Methods for prediction of soil dielectric properties: a review. Technical report, SPIE–The International Society for Optical Engineering.
- Dam, R. L. v., Borchers, B., Hendrickx, J. M. H., and Harmon, R. S. (2003). Effects of soil water content and texture on radar and infrared landmine sensors: implications for sensor fusion. *Proc. of the Internat. Conf. on Requirements and Technologies for the Detection, Removal, and Neutralization of Landmines and UXO*, 1:107–114.
- Davis, J. L. and Annan, A. P. (1989). Ground-penetrating radar for high-resolution mapping of soil and rock stratigraphy. *Geophysical Prospecting*, 37(37):531–551.
- Debye, P. (1929). *Polar Molecules*. Dover, New York.
- Dekker, L. W., Ritsema, C. J., Wendroth, O., Jarvis, N., Oostindie, K., Pohl, W., Larsson, M., and Gaudet, J.-P. (1999). Moisture distributions and wetting of soils at experimental fields in the Netherlands, France, Sweden and Germany. *Journal of Hydrology*, 215:4–22.
- DeLoor, G. P. (1964). Dielectric properties of heterogeneous mixtures. *Applied Scientific Research*, B11:310–320.
- Demtröder (1995). *Experimentalphysik 2: Elektrizität und Optik*. Springer, Berlin, 1st edition.
- Deutsch, C. V. and Journel, A. G. (1998). *GSLIB: Geostatistical Software Library and User's Guide*. Oxford University Press, 2nd edition.
- Dirksen, C. and Dasberg, S. (1993). Improved calibration of time domain reflectometry soil water content measurements. *Soil Science Society American Journal*, 57:660–667.
- Dobson, M. C., Ulaby, F. T., Hallikainen, M. T., and El-Rayes, M. A. (1985). Microwave dielectric behaviour of wet soil – part ii: Dielectric mixing models. *IEEE Transactions on Geoscience and Remote Sensing*, 23:35–46.

- Du, S. (1996). *Determination of Water Content in the Subsurface with the Ground Wave of Ground Penetrating Radar*. Dissertation, Universität München.
- FAO (2006). Food and Agriculture Organization of the United Nations: World reference base for soil resources - a framework for international classification, correlation and communication.- World soil resources reports 103, Rome.
- Feddes, R. A., Koopmans, R. W. R., and van Dam, J. C. V. (1999). *Agrohydrology*. Wageningen University, Department of Wate Resources.
- Fisher, E., McMechan, G. A., and Annan, A. P. (1992). Acquisition and processing of wide-aperture ground-penetrating radar data. *Geophysics*, 57(3):495–504.
- Fließbach, T. (2005). *Lehrbuch zur Theoretischen Physik II, Elektrodynamik*. Elsevier, München, 4th edition.
- Friedel, S. (2000). *Über die Abbildungseigenschaften der geoelektrischen Impedanztomographie unter Berücksichtigung von endlicher Anzahl und endlicher Genauigkeit der Meßdaten*. Dissertation, Universität Leipzig.
- Friedel, S. (2003). Resolution, stability and efficiency of resistivity tomography estimated from a generalized inverse approach. *Geophysical Journal International*, 153:305–316.
- Galagedara, L. W., Parkin, G. W., Redman, J. D., Bertoldi, P. v., and Endres, A. L. (2005). Field studies of the gpr ground wave method for estimating soil water content during irrigation and drainage. *Journal of Hydrology*, 301:182–197.
- Garambois, S., Sénéchal, P., and Perroud, H. (2002). On the use of combined geophysical methods to assess water content and water conductivity of near-surface formations. *Journal of Hydrology*, 259:32–48.
- Gerhartz, W. (1996). *Ullmann's Encyclopedia of Industrial Chemistry*, volume A, 28. VCH Verlagsgesellschaft, Weinheim.
- Goovaerts, P. (1997). *Geostatistics for Natural Resources Evaluation*. Oxford University Press.
- Greaves, R. J., Lesmes, D. P., Lee, J. M., and Toksötz, M. N. (1996). Velocity variations and water content estimated from multi-offset ground-penetrating radar. *Geophysics*, 61:683–695.

- Grote, K., Hubbard, S., Harvey, J., and Rubin, Y. (2005). Evaluation of infiltration in layered pavements using surface gpr reflection techniques. *Journal of Applied Geophysics*, 57:129–153.
- Grote, K., Hubbard, S., and Rubin, Y. (2003). Field-scale estimation of volumetric water content using ground-penetrating radar ground wave techniques. *Water Resources Research*, 39(11):1321–1333.
- Günther, T. (2004). *Inversion Methods and Resolution Analysis for the 2D/3D Reconstruction of Resistivity Structures from DC Measurements*. Dissertation, Technische Universität Bergakademie Freiberg.
- Hanafy, S. and el Hagrey, S. A. (2006). Ground-penetrating radar tomography for soil-moisture heterogeneity. *Geophysics*, 71:K9–K18.
- Hendrickx, J. M. H., Borchers, B., and Woolslayer, J. (2001). Spatial variability of dielectric properties in field soils. In *Detection and remediation technologies for mines and minelike targets VI, SPIE proceedings vol. 4394*, pages 398–408.
- Herbst, M., Diekkrüger, B., and Vanderborght, J. (2006). Numerical experiments on the sensitivity of runoff generation to the spatial variation of soil hydraulic properties. *Journal of Hydrology*, 326:43–58.
- Holliger, K., Lampe, B., Meier, U., and Lambert, M. (2004). Realistic modelling of surface ground-penetrating radar antenna systems: where do we stand? *Near Surface Geophysics*, 2:11–19.
- Hubbard, S., Grote, K., and Rubin, Y. (2002). Mapping the volumetric soil water content of a california vineyard using high-frequency gpr ground wave data. *The Leading Edge*, 21(6):552–559.
- Hübner, C. (1999). *Entwicklung hochfrequenter Meßverfahren zur Boden- und Schneefeuchtebestimmung*. Dissertation, Universität Karlsruhe (TH).
- Huisman, J. A., Hubbard, S. S., Redman, J. D., and Annan, A. P. (2003a). Measuring soil water content with ground penetrating radar: a review. *Vadose Zone Journal*, 2:476–491.
- Huisman, J. A., Snepvangers, J. J. J. C., Bouten, W., and Heuvelink, G. B. M. (2002). Mapping spacial variation in surface soil water content: comparison of ground-penetrating radar and time domain reflectometry. *Journal of Hydrology*, 269:194–207.

- Huisman, J. A., Snepvangers, J. J. J. C., Bouten, W., and Heuvelink, G. B. M. (2003b). Monitoring temporal development of spacial soil water content variation: comparison of ground penetrating radar and time domain reflectometry. *Vadose Zone Journal*, 2:519–529.
- Huisman, J. A., Sperl, C., Bouten, W., and Verstaten, J. M. (2001). Soil water content measurements at different scales: accuracy of time domain reflectometry and ground-penetrating radar. *Journal of Hydrology*, 245:48–58.
- ITEP, editor (2002). *International test and evaluation program for humanitarian demining: Soil electromagnetic characteristics and metal detector performance*, Via E. Fermi, I-21020 Ispra (VA). Joint Research Centre, Ispra.
- Jackson, J. D. (1999). *Classical Electrodynamics*. John Wiley & Sons, 3rd edition.
- Journal, A. G. and Huijbregts, C. J. (1978). *Mining Geostatistics*. Academic Press.
- Kaatze, U. (1989). Complex permittivity of water as a function of frequency and temperature. *Journal of Chemical Engineering Data*, 34:372–374.
- Keller, G. V. and Frischknecht, F. C. (1970). *Electrical Methods in Geophysical Prospecting*. International Series of Monographs in Electromagnetic Waves Volume 10. Pergamon Press, 1st edition.
- King, R. W. P., Owens, M., and Wu, T. T. (1992). *Lateral Electromagnetic Waves*. Springer Verlag, New York.
- Knight, R., Tercier, P., and Irving, J. (2004). The effect of vertical measurement resolution on the correlation structure of a ground penetrating radar reflection image. *Geophysical Research Letters*, 31:L21607.
- Knight, R. J. and Endres, A. L. (2006). *An Introduction to Rock Physics Principles for Near-Surface Geophysics*, chapter 3, pages 31–70. Investigations in Geophysics, No. 13. Society of Exploration Geophysicists.
- Knödel, K., Krummel, H., and Lange, G. (1997). *Handbuch zur Erkundung des Untergrundes von Deponien und Altlasten; Bd. 3: Geophysik*. Springer.
- Krige, D. G. (1951). A statistical approach to some basic mine valuation problems on the Witwatersrand. *Journal of the Chemical, Metallurgical and Mining Society of South Africa*, 52:119–139.

- Lampe, B. and Holliger, K. (2003). Effects of fractal fluctuations in topographic relief, permittivity and conductivity on ground-penetrating radar antenna radiation. *Geophysics*, 68(6):1934–1944.
- Lehmann, W. (1995). *Anwendung geostatistischer Verfahren auf die Bodenfeuchte in ländlichen Einzugsgebieten*. Dissertation, Institut für Hydrologie und Wasserwirtschaft, Universität Karlsruhe (TH).
- Löhken, J. O. (2007). *Analytische Berechnung, Finite Elemente Simulation und Inversion von Metalldetektorsignalen im Zeit- und Frequenzbereich. Untersuchungen zur Reduzierbarkeit der Fehlalarmrate bei der Landminensuche*. Dissertation, in preparation, Universität zu Köln.
- Loke, M. H. and Barker, R. D. (1996). Rapid least-squares inversion of apparent resistivity pseudosections by a quasi-newton method. *Geophysical Prospecting*, 44:131–152.
- MacDonald, J., Lockwood, J. R., McFee, J., Altshuler, T., Broach, T., Carin, L., Harmon, R., Rappaport, C., Scott, W., and Weaver, R. (2003). *Alternatives for landmine detection*. RAND corporation.
- Makinde, W., Favretto-Cristini, N., and de Bazelaire, E. (2005). Numerical modelling of interface scattering of seismic wavefield from a random rough interface in an acoustic medium: comparison between 2d and 3d cases. *Geophysical Prospecting*, 53:373–397.
- Marquardt, D. W. (1963). An algorithm for least-squares estimation of non-linear parameters. *Journal of the Society for Industrial and Applied Mathematics*, 11:431–441.
- Matheron, G. (1965). *Les variables régionalisées et leur estimation. Une application de la théorie des fonctions aléatoires aux Sciences de la Nature*. Masson, Paris.
- Matheron, G. (1971). *The Theory of Regionalised Variables and its Applications*. Fasc. 5, Cahier du Centre de Morphologie Mathématique de Fontainebleau. Ecoles des Mines de Paris.
- Mayer, V. (2006). *Modellierung elektromagnetischer Wellenausbreitung unter Berücksichtigung von im Labor gemessenen Materialeigenschaften*. Dissertation, Universität Karlsruhe (TH).

- Miao, Y., Robinson, C. A., Stewart, B. A., and Evett, S. E. (2000). Comparison of soil spatial variability in crop and rangeland. In *5th Int. Conf. on Precision Agriculture and Other Resource Management*, Bloomington, MN, USA.
- Militzer, H. and Weber, F. (1985). *Angewandte Geophysik*, volume 2. Springer.
- Miller, T. W., Borchers, B., Hendrickx, J. M. H., Hong, S.-H., Dekker, L. W., and Ritsema, C. J. (2002). Effects of soil physical properties on GPR for landmine detection. In *Fifth Int. Symp. on Technology an the Mine Problem, Monterey, CA*.
- Montenegro Ferrigno, H. (1995). *Parameterbestimmung und Modellierung in heterogenen Böden*. Dissertation, Institut für Hydromechanik der Universität Karlsruhe (TH).
- Moysey, S. and Knight, R. (2004). Modeling the field-scale relationship between dielectric constant and water content in heterogeneous systems. *Water Resources Research*, 40(3).
- Müller, M., Mohnke, O., Schmalholz, J., and Yaramanci, U. (2003). Moisture assessment with small-scale geophysics — the interurban project. *Near Surface Geophysics*, 1:173–181.
- Olea, R. A. (1999). *Geostatistics for Engineers and Earth Scientists*. Kluwer Academic Publishers.
- Olhoeft, G. R. (1998). Electrical, magnetic, and geometric properties that determine ground penetrating radar performance. In *Seventh International Conference on Ground Penetrating Radar*, pages 177–182, University of Kansas, Lawrence, KS, USA.
- Or, D. and Wraith, J. M. (1999). Temperature effects on soil bulk dielectric permittivity measured by time domain reflectometry: a physical model. *Water Resources Research*, 35(2):371–383.
- Overmeeren, R. A., Sariowan, S. V., and Gehrels, J. C. (1997). Ground penetrating radar for determining volumetric soil water content; results of comparative measurements at two test sites. *Journal of Hydrology*, 197:316–338.
- Pannatier, Y. (1996). *Variowin: Software for Spatial Data Analysis in 2D*. Springer, New York.
- Papoulis, A. (1962). *The Fourier Integral and Its Applications*. McGraw-Hill Electronic Sciences Series. McGraw-Hill Book Company.

- Rea, J. and Knight, R. (1998). Geostatistical analysis of ground-penetrating radar data: A means of describing spatial variation in the subsurface. *Water Resources Research*, 34(3):329–339.
- Ritsema, C. J. and Dekker, L. W. (1994). How water moves in a water repellent soil. 2. dynamics of fingered flow. *Water Resources and Research Letters*, 30:2519–2531.
- Roth, K., Schulin, R., Flühler, H., and Attinger, W. (1990). Calibration of time domain reflectometry for water content measurement using a composite dielectric approach. *Water Resources Research*, 26(10):2267–2273.
- Rothammel, K. and Krischke, A. (2001). *Antennenbuch*. DARC Verlag, 12th edition.
- Sandmeier, K. J. (2006). *Reflex-Win Version 4.2, Windows 9x/NT/2000/XP-program for the processing of seismic, acoustic or electromagnetic reflection, refraction and transmission data*. Sandmeier software.
- Schafmeister-Spierling, M.-T. (1990). *Geostatistische Simulationstechniken als Grundlage der Modellierung von Grundwasserströmung und Stofftransport in heterogenen Aquifersystemen*. Dissertation, Freie Universität Berlin.
- Schmalholz, J. (2007). *Georadar for small-scale high-resolution dielectric property and water content determination of soils*. Dissertation, Technische Universität Berlin.
- Schmalholz, J., Stoffregen, H., Kemna, A., and Yaramanci, U. (2004). Imaging of water content distributions inside a lysimeter using gpr tomography. *Vadose Zone Journal*, 3:1106–1115.
- Schmalz, B., Lennartz, B., and Wachsmuth, D. (2002). Analyses of soil water content variations and gpr attribute distributions. *Journal of Hydrology*, 267:217–226.
- Schön, J. (1996). *Physical Properties of Rocks; Fundamentals and Principles of Petrophysics*. Pergamon.
- Serbin, G. and Or, D. (2003). Near-surface soil water content measurements using horn antenna radar: methodology and overview. *Vadose Zone Journal*, 2:500–510.

- Shen, L. C., Savre, W. C., Price, J. M., and Athavale, K. (1985). Dielectric properties of reservoir rocks at ultra-high frequencies. *Geophysics*, 50(4):692–704.
- Sihvola, A. H. and Kong, J. A. (1988). Effective permittivity of dielectric mixtures. *IEEE Transactions on Geoscience and Remote Sensing*, 26:420–429.
- Sommerfeld, A. (1967). *Vorlesungen über Theoretische Physik, Band III: Elektrodynamik*. Akademische Verlagsgesellschaft Geest & Portig, Leipzig, 4th edition.
- Sperl, C. (1999). *Erfassung der raum-zeitlichen Variation des Bodenwassergehalts in einem Agrarökosystem mit dem Ground-Penetrating Radar*. Dissertation, Technische Universität München.
- Stacheder, M. (1996). *Die Time Domain Reflectometry in der Geotechnik*. Dissertation, Universität Karlsruhe (TH), Schriftenreihe Angewandte Geologie Karlsruhe, 40.
- Stummer, P., Maurer, H., and Green, A. G. (2004). Experimental design: Electrical resistivity data sets that provide optimum subsurface information. *Geophysics*, 69(1):120–139.
- Täumer, K., Stoffregen, H., and Wessolek, G. (2006). Seasonal dynamics of preferential flow in a water repellent soil. *Vadose Zone Journal*, 5(1):405–411.
- Topp, G. C., Davis, J. L., and Annan, A. P. (1980). Electromagnetic determination of soil water content: measurements in coaxial transmission lines. *Water Resources Research*, 16(3):574–582.
- Topp, G. C., Davis, J. L., and Annan, A. P. (1982). Electromagnetic determination of soil water content using TDR: II. evaluation of installation and configuration of parallel transmission lines. *Soil Science Society of America Journal*, 46:678–684.
- Tronicke, J. and Holliger, K. (2005). Quantitative integration of hydrogeophysical data: Conditional geostatistical simulation for characterizing heterogeneous alluvial aquifers. *Geophysics*, 70(3):H1–H10.
- Turesson, A. (2006). Water content and porosity estimated from ground-penetrating radar and resistivity. *Journal of Applied Geophysics*, 58:99–111.

- Ulaby, F. T., Dubois, P., and Zyl, J. (1996). Radar mapping of surface moisture. *Journal of Hydrology*, 184(1–2):57–84.
- Ulaby, F. U., Moore, R. K., and Adrian, K. F. (1986). *Microwave Remote Sensing: Active and Passive*, volume 3: From Theory to Applications. Artech House.
- Vanderborght, J., Kasteel, R., and Vereecken, H. (2006). Stochastic continuum transport equations for field-scale solute transport. *Vadose Zone Journal*, 5:184–203.
- Ward, H. S. and Hohmann, G. W. (1988). *Electromagnetic Theory for Geophysical Applications*, volume 1, chapter 4, pages 131–311. Society of Exploration Geophysicists, Tulsa, Oklahoma.
- Wendroth, O., Pohl, W., Koszinski, S., Rogasik, H., Ritsema, C. J., and Nielsen, D. R. (1999). Spatio-temporal patterns and covariance structures of soil water status in two northeast-german field sites. *Journal of Hydrology*, 215:38–58.
- Wessel, B. (2006). *Automatische Extraktion von Straßen aus SAR-Bilddaten*. Dissertation, Technische Universität München.
- Western, A. W. and Blöschl, G. (1999). On the spatial scaling of soil moisture. *Journal of Hydrology*, 217:203–224.
- Western, A. W., Blöschl, G., and Grayson, R. B. (1998). Geostatistical characterisation of soil moisture patterns in the Tarrawarra catchment. *Journal of Hydrology*, 205:20–37.
- Wollny, K. G. (1999). *Die Natur der Bodenwelle des Georadar und ihr Einsatz zur Feuchtebestimmung*. Dissertation, Ludwig-Maximilians-Universität München.
- Wood, E. F. (1997). Effects of soil water aggregation on surface evaporative fluxes. *Journal of Hydrology*, 190:397–412.
- Wtorek, J., Wyszynska, J., and Zduniak, A. (2003). EUDEM2 Technology Survey: Determination of Spatial Variability of Soil Conductivity. EU Humanitarian Demining – State of the Art on HD Technologies, Products, Services and Practices in Europe, Gdańsk University of Technology.

Acknowledgements

This work was written for the project "Metal detectors for Humanitarian Demining: Development potentials for data analysis and measurement techniques" funded by the German Federal Ministry of Education and Research (BMBF) under contract number 01 RX 0310 during my employment at the Leibniz Institute for Applied Geosciences in Hannover, Germany.

I am grateful to the supervisors of this thesis. I would like to thank Prof. A. Junge for the trust he put in me, the support and confidence he gave me in following the right path. My thanks also go to Prof. H. Wilhelm who thoroughly read the manuscript with the required distance and who added clarifying comments. I was very pleased that he agreed to be my supervisor after all the years since I left Karlsruhe University.

My gratitude goes to Thomas Wonik for managing the BMBF project and shielding me from most of the bureaucratic work. Without this additional time I wouldn't have been able to concentrate on the scientific topic and it would have been even more difficult to write this thesis.

No fieldwork – no data, no data – no thesis. Therefore, I am indebted to all the persons supporting the measurements or constructing some special devices: Bernd Ehret, Dieter Epping, Thomas Grelle, Robert Meyer, Wolfgang Südekum, Holger Preetz and Sven Uchtmann. Sven did not only share the room with me but also his personal computer capacity for the longsome FD calculations and revised parts of the manuscript. Special thanks go to my project colleague Holger who taught me some aspects of soil sciences and provided the pedologic descriptions.

No software – no calculations, no calculations – no thesis. Thanks to Thomas Günther for providing his software (DC2DInvRes and DC3dInvRes), the support I got and for revising parts of the manuscript. Jupp Sandmeier implemented many additional tools to his programme REFLEX whenever I needed them for my work, e.g. the import function for the FD models. Lothar Gorling assisted me in installing the Fortran libraries of GSLIB on my computer.

I am grateful to Slavica Babinka, Thies Beilecke, Ralf Gelfort, Michael Grinat, Wolfram Rühaak, Hanna-Maria Rumpel, Jörn Schünemann, Stefan Wessling and Regine Ziekur for all their little tips, their support and encouragement. Hanna and Thies added the finishing touches to the introductory and closing words. Thanks to all the colleagues at the institute who are not mentioned here but who have contributed to this thesis by creating an enjoyable working atmosphere.

My thanks go to Ulla Noell and Oliver Mohnke for the discussion on resistivity and some helpful hints.

A great help was the continuing contact with my former student fellows Helgard Anschütz and Jürgen Schmalholz. Working on a related topic, Jürgen was an important counterpart to debate all the ideas and numberless GPR problems. Thanks for all the chats not only on scientific subjects. Helgard seemed to take refuge to Antarctica most of the time but once in a while we could pity one another for our hard life as doctoral candidates. Thanks to both of them for critically reading parts of the manuscript.

I am grateful to my *marvellous* sister Marike for the linguistic revision of the manuscript and for her patience with teaching me all the types of conditional clauses. Finally my thanks go to my friends and my family for their encouragement. Special thanks to those who did NOT ask me every day when I would finish.

Curriculum Vitae

Personal

Name	Jan Stephan Igel
Date of Birth	09.05.1974
Place of Birth	Wangen im Allgäu, Germany
Nationality	German and French

Professional Record

since 01/2004	Research assistant at Leibniz Institute for Applied Geosciences (GGA Institute), Hannover, Germany: Soil influence on landmine detection. Contribution to BMBF project on humanitarian demining "HuMin/MD".
11/2001–12/2003	Research assistant at GGA Institute: Geophysical Investigations in salt deposits. Contribution to BMBF project "Salinargeophysik II".
12/2000–02/2001	Undergraduate research assistant at the Alfred-Wegener-Institute for Polar and Marine Research, Bremerhaven, Germany: GPR measurements on the Antarctic ice shield.
02/1998–06/1998	Undergraduate research assistant at the Geophysical Institute of University of Göttingen, Germany: Seismological measurements within the "Eifel-plume" project.
1996–2001	Undergraduate research assistant at the Geophysical Institute of Karlsruhe University: Mentoring field and lab courses in magnetics, geoelectrics and GPR.

Education

- 03/2001 Diploma (M.Sc.) in Geophysics at Karlsruhe University. Diploma thesis: "Entwicklung und Vergleich verschiedener Methoden zur Bestimmung der Bodenfeuchte mit dem Georadar" (Developing and comparing techniques to determine soil moisture with ground-penetrating radar).
- 10/1994–03/2001 Studies of Geophysics at Karlsruhe University. Major subjects: experimental physics, geophysics, rock mechanics and hydrogeology.
- 1984–1993 Grammar school "Rupert-Ness-Gymnasium" Wangen, Germany. Abitur (a-level) in 1993.

Declaration

I hereby declare that the present work was made by myself and no other than the cited sources were used.

Ich erkläre hiermit, die vorliegende Arbeit selbstständig und nur mit den angegebenen Hilfsmitteln angefertigt zu haben.

Jan Igel

Hannover, April 2007

